



ISSN 1343-2230

CNS-REP-88
February, 2012

Annual Report 2010

Center for Nuclear Study,
Graduate School of Science, the University of Tokyo

Editors
Taku Gunji

Center for Nuclear Study

CNS Reports are available from:
Wako-Branch at RIKEN
Center for Nuclear Study,
Graduate School of Science, the University of Tokyo
2-1 Hirosawa, Wako
351-0198, Japan
Tel: +81-48-464-4191
Fax: +81-48-464-4554

Annual Report 2010

Center for Nuclear Study,
Graduate School of Science, the University of Tokyo

Preface

This is the annual report of the Center for Nuclear Study (CNS), Graduate School of Science, the University of Tokyo, for the fiscal year 2010 (April 2010 through March 2011). During this period, a lot of research activities in various fields of nuclear physics have been carried out and a wide variety of fruitful results have been obtained at CNS. This report summarizes research such activities. I hereby mention some highlights of the report.

The NUSPEQ (NUclear SPectroscopy for Extreme Quantum system) group studies exotic structures in high-isospin and/or high-spin states in nuclei. The CNS GRAPE (Gamma-Ray detector Array with Position and Energy sensitivity) is a major apparatus for high-resolution in-beam gamma-ray spectroscopy. Missing mass spectroscopy using the SHARAQ is going to start as another approach on exotic nuclei. In 2010, the following progress has been made. New high-spin states in $^{49-51}\text{Ti}$ populated by fusion reactions of an RI beam have been found, which gives information on the $N=28$ shell gap and the single particle energies in the fp-shell. High-spin states in $A\sim 40$, mass region were studied via $^{18}\text{O}+^{26}\text{Mg}$ fusion evaporation reactions. A superdeformed rotational band ($\beta_2 \sim 0.5$) was observed up to 12^+ state in ^{40}Ar . This finding indicates the presences of the $N=22$ and $Z=18$ superdeformed shell structure in this region. High-spin states of ^{107}In were studied via the $^{58}\text{Ni}(^{32}\text{Cr}, 3p)$ reaction. A rotational cascade consisting of ten gamma-ray transitions was observed. The band exhibits the features typical for smooth terminating bands in $A \sim 100$ mass region.

Upgrade of the readout system of the CNS GRAPE has started, where digital pulse data taken by sampling ADCs are analyzed by FPGAs on boards. Proposal for studying tetra neutron system using the double-charge exchange reaction $^4\text{He}(^8\text{He } ^8\text{Be})4n$ at 200 A MeV was submitted to the NP-PAC and approved, which will be performed in near future.

Major program of the nuclear astrophysics group is to study nuclear reactions and structures under explosive conditions in the universe, and clarify the mechanism of stellar evolution and explosive phenomena such as supernovae. High-intensity RI beams of light nuclei from the CNS low-energy RI beam separator CRIB provide a good opportunity to study stellar nuclear reactions under explosive conditions both by the direct method as well as by indirect methods. The research programs include investigations of α induced stellar reactions on ^7Be , ^{18}Ne , and ^{30}S . The $^{12}\text{N}(p,\gamma)$ stellar reaction was also investigated indirectly using a ^{12}N beam with the ANC method. Developments were also made for new RI beams, and an active target with GEM (GEM-MSTPC) has been developed and used successfully for direct measurements of (α,p) stellar reactions using ^{18}Ne and ^{30}S beams. This demonstrated that the GEM-MSTPC detector can measure efficiently stellar reactions with low-cross sections. Further technological development for the Wien-filter of CRIB was made in the past year.

Main goal of the quark physics group is to understand the properties of hot and dense nuclear matter created by colliding heavy nuclei at relativistic energies. The group has been involved in the PHENIX experiment at Relativistic Heavy Ion Collider (RHIC) at Brookhaven National Laboratory, and in the ALICE experiment at Large Hadron Collider (LHC) at CERN. A big news in this year was that LHC succeeded making Pb+Pb collisions in November of 2010. As for PHENIX, the group has been concentrating on the physics analysis involving leptons and photons, which include direct photon production at low transverse momentum using the virtual-gamma method, neutral pion production with high transverse momentum as a function of azimuthal angle from the reaction plane in Au+Au collisions, and J/ψ production in ultra-peripheral Au+Au collisions. The group has also been involved in the construction and commissioning of Si VTX detector subsystem. As for ALICE, the group has been involved in the commissioning of the Transition Radiation Detector (TRD), and calibration and performance study of Time Projection Chamber (TPC). Efforts to analyze p+p and Pb+Pb data have been initiated. The group has also been playing a leading role in the development of forward calorimeter for future upgrade. R&D of gas electron multiplier (GEM) and related techniques has been continuing. Development of resistive GEM with resistive anodes has been progressing in

collaboration with the Tamagawa group of RIKEN.

The SHARAQ promoted momentum and angular dispersion matching (DM) technique for RI beams. We successfully achieved DM beam transport by using RI beams of ^{10}C and ^{12}N in BigRIPS, High-resolution beamline and SHARAQ spectrometer, following the achievement of DM transport with a primary ^{14}N beam in 2009. By using the DM beam transport, we performed two experiments to search the isovector spin monopole (IVSM) mode and the isovector spin-non-flip monopole (IVM) mode in nuclei: In the experiment for IVSM, we obtained an excitation function in $^{90}\text{Zr}(^{12}\text{N},^{12}\text{C})$ reaction, which is exothermic and is possible to excite the target nucleus by IVSM mode with recoil-less; The experiment for IVM aims at searching IVM mode of nuclear excitation. We observed the spectra in $^{90}\text{Zr}(^{10}\text{C},^{10}\text{B}(E_x = 1740 \text{ keV}))$ channel, which is likely to be an effective probe for IVM excitation because of its feature of $\Delta T=1$ and $\Delta S=0$. The analyses of these experimental data are now in progress. SHARAQ group developed two tracking detectors installed in the beam line especially in the point of high-rate operation. As a tracking detector for small beam spot and high intensity, we developed a stack of plastic scintillators (Plastic tracker). Hit positions are determined by light output from each plastic bar, its position resolution is 1 mm, corresponding to the plastic scintillator width. Secondly, the low-pressure MWDC for beam tracking developed by study of its operation parameters. After optimization, the capability of beam tracking advanced up to 2×10^6 particles/sec and the detector stably operated by RI beam of 10^6 cps during 2 weeks.

One of the Major tasks of the accelerator group is the AVF upgrade project which includes development of ion sources, upgrading the AVF cyclotron of RIKEN and the beam line to CRIB. Development of ECR heavy ion sources is to provide a new HI beams, higher and stable beams of metallic ions, and to improve the control system. Two CNS ECR sources now provide all the beams for the AVF cyclotron and support not only CRIB experiments but also a large number of RIBF experiments. A charge-breeding ECR source is also under development. Three major works were advanced for upgrading the AVF cyclotron. The first is a design study of the central region of the cyclotron with harmonic number of 1. The second is installation of a new central module to increase the beam energy up to K78. The third is installation of a new beam deflector monitor to improve the transmission efficiency. Injection beam monitoring and control are being studied. New ion-source beam diagnosis and monitoring system (ISDM) was designed. This new beam monitor will become a powerful tool for all the RIBF facility.

The nuclear theory group has been promoting the RIKEN-CNS joint research project on large-scale nuclear-structure calculations since 2001 under mutual agreement with RIKEN, and maintaining its parallel computer system. In the fiscal year 2010, we have developed a new Monte Carlo shell model (MCSM) code under this computer system in order to run the code on up-to-date massively parallel supercomputers such as "K computer". This year has also seen methodological advancement in the MCSM by introducing a novel extrapolation method which enables us to obtain the energy in very good accuracy. Another important activity is the evaluation of the Gamow-Teller strengths and electron capture rates in Ni isotopes, which plays an important role for understanding the initial conditions for the nucleosynthesis in supernova explosions. We also mention that the monopole strength of the ^{12}C was studied in terms of α cluster model.

The 9th CNS International Summer School (CISS10) has been organized in August 2010 with many invited lecturers including four foreign distinguished physicists.

Finally, I thank Ms. M. Hirano and other administrative staff members for their heartfelt contributions throughout the year.

Takaharu Otsuka
Director of CNS



Table of Contents

1a. Experimental Nuclear Physics: Low and Intermediate Energies

Excitation functions of ${}^7\text{Be}+\alpha$ elastic and inelastic scattering cross section	1
<i>H. Yamaguchi, T. Hashimoto, S. Hayakawa, D.N. Binh, D. Kahl, S. Kubono, T. Kawabata, T. Teranishi, Y. Wakabayashi, N. Iwasa, Y. Miura, Y.K. Kwon, L.H. Khiem, and N.N. Duy</i>	
Present status of the direct measurement of the ${}^{18}\text{Ne}(\alpha, p){}^{21}\text{Na}$ reaction cross sections using the GEM - MSTPC	3
<i>T. Hashimoto, S. Kubono, H. Yamaguchi, S. Hayakawa, D. Kahl, S. Ota, S. Michimasa, H. Tokieda, K. Yamaguchi, I. Arai, T. Komatsubara, H. Ishiyama, Y.X. Watanabe, H. Miyatake, Y. Hirayama, N. Imai, S. C. Jeong, Y. Mizoi, S. K. Das, T. Fukuda, H. Makii, Y. Wakabayashi, N. Iwasa, T. Yamada, A. A. Chen, J. J. He</i>	
High-Spin Level Structure in ${}^{35}\text{S}$	5
<i>E. Ideguchi, S. Go, H. Miya, K. Kisamori, M. Takaki, S. Ota, S. Michimasa, S. Shimoura, T. Koike, T. Yamamoto, K. Shirotori, Y. Ito, J. Takatsu, T. Suzuki, T. Morikawa, M. Oshima, M. Koizumi, Y. Toh, A. Kimura, H. Harada, K. Furutaka, S. Nakamura, F. Kitatani, Y. Hatsukawa, T. Shizuma, M. Sugawara, Y.X. Watanabe, and Y. Hirayama</i>	
Spectroscopic study of ${}^9\text{He}$ via the double charge exchange (${}^{18}\text{O}, {}^{18}\text{Ne}$) reaction	7
<i>H. Matsubara, M. Takaki, T. Uesaka, S. Shimoura, N. Aoi, M. Dozono, T. Fujii, K. Hatanaka, T. Hashimoto, T. Kawabata, S. Kawase, K. Kisamori, Y. Kikuchi, Y. Kubota, C.S Lee, H.C. Lee, Y. Maeda, S. Michimasa, K. Miki, H. Miya, S. Noji, S. Ota, S. Sakaguchi, Y. Sasamoto, T. Suzuki, L.T Tang, K. Takahisa, H. Tokieda, A. Tamii, K. Yako, Y. Yasuda, N. Yokota, R. Yokoyama, and J. Zenihiro</i>	
Measurement of the ${}^{90}\text{Zr}({}^{12}\text{N}, {}^{12}\text{C}){}^{90}\text{Nb}$ reaction at 200 MeV/nucleon	9
<i>S. Noji, H. Sakai, N. Aoi, H. Baba, G. P. A. Berg, R. Chen, P. Doornenbal, M. Dozono, N. Fukuda, N. Inabe, D. Kameda, T. Kawabata, S. Kawase, Y. Kikuchi, K. Kisamori, T. Kubo, Y. Maeda, H. Matsubara, S. Michimasa, K. Miki, H. Miya, H. Miyasako, S. Sakaguchi, Y. Sasamoto, S. Shimoura, M. Takaki, H. Takeda, S. Takeuchi, H. Tokieda, T. Ohnishi, S. Ota, T. Uesaka, H. Wang, K. Yako, Y. Yanagisawa, N. Yokota, K. Yoshida</i>	
The super-allowed Fermi type charge exchange reaction for studies of isovector non-spin-flip monopole resonance ..	11
<i>Y. Sasamoto, T. Uesaka, S. Shimoura, S. Michimasa, S. Ota, K. Miki, S. Noji, K. Yako, H. Tokieda, H. Miya, S. Kawase, Y. Kikuchi, K. Kisamori, M. Takaki, M. Dozono, H. Mathubara, H. Sakai, T. Kubo, Y. Yanagisawa, H. Takeda, K. Yoshida, T. Ohnishi, N. Fukuda, D. Kameda, N. Inabe, N. Aoi, S. Takeuchi, T. Ichihara, H. Baba, S. Sakaguchi, P. Doornenbal, H. Wang, R. Chen, Y. Shimizu, T. Kawahara, T. Kawabata, N. Yokota, Y. Maeda, H. Miyasako, G. P. A. Berg</i>	
Proton spin-orbit splitting in ${}^{18}\text{O}$ studied by the $(\vec{p}, 2p)$ reaction at 200 MeV	13
<i>S. Kawase, T. Uesaka, S. Ota, H. Tokieda, Y. Kikuchi, K. Kisamori, M. Takaki, H. Matsubara, M. Dozono, T. Kawahara, T. Kawabata, Y. Nozawa, N. Yokota, T. Noro, T. Wakasa, M. Okamoto, Y. Maeda, T. Saito, H. Miyasako, A. Tamii, and T. Suzuki</i>	
Development of heavy-ion detection at GRAND RAIDEN spectrometer for the (${}^{18}\text{O}, {}^{18}\text{Ne}$) reaction	15
<i>M. Takaki, H. Matsubara, T. Uesaka, S. Shimoura, N. Aoi, M. Dozono, T. Fujii, K. Hatanaka, T. Hashimoto, T. Kawabata, S. Kawase, K. Kisamori, Y. Kikuchi, Y. Kubota, C.S. Lee, H.C. Lee, Y. Maeda, S. Michimasa, K. Miki, H. Miya, S. Noji, S. Ota, S. Sakaguchi, Y. Sasamoto, T. Suzuki, L.T. Tang, K. Takahisa, H. Tokieda, A. Tamii, K. Yako, Y. Yasuda, N. Yokota, R. Yokoyama, and J. Zenihiro</i>	
1b. Experimental Nuclear Physics: PHENIX Experiment at BNL-RHIC and ALICE Experiment at CERN-LHC	
First Results of Pb+Pb Collisions at $\sqrt{s_{NN}}=2.76$ TeV from LHC-ALICE	17
<i>T. Gunji, H. Hamagaki, S. Sano, Y. Hori, for the ALICE Collaboration</i>	
Measurement of multi-strange particles in $\sqrt{s} = 7$ TeV $p + p$ collisions at LHC-ALICE	19

<i>S. Sano, H. Hamagaki, T. Gunji, for the ALICE collaboration</i>	
Study of nuclear effects on low p_T direct photon production in $\sqrt{s_{NN}} = 200$ GeV $d+Au$ collisions at RHIC	21
<i>Y.L. Yamaguchi, H. Hamagaki, Y. Akiba^a, and T. Gunji, for the PHENIX collaboration</i>	
Neutral Pion Production with Respect to the Azimuthal Angle in Au+Au Collisions at $\sqrt{s_{NN}} = 200$ GeV	23
<i>Y. Aramaki, T. Sakaguchi, G. David, H. Hamagaki, for the PHENIX Collaboration</i>	
Operation and Performance of the Silicon Pixel Detector for the PHENIX Vertex Tracker	25
<i>R. Akimoto, Y. Akiba, H. Asano, T. Gunji, T. Hachiya, H. Hamagaki, M. Kurosawa, H. Sako, S. Sato, A. Take-tani (for the PHENIX Collaboration)</i>	
Study of TPC $E \times B$ distortion at LHC-ALICE experiment	27
<i>Y. Hori, S. Rossegger, J. Thomas, M. Ivanov, C. Ivan, T. Gunji, H. Hamagaki</i>	
Simulation study of the Forward Calorimeter for LHC-ALICE	29
<i>T. Tsuji, H. Hamagaki, T. Gunji, Y. Hori</i>	
ASIC development for ALICE FOCAL readout	31
<i>S. Hayashi, H. Hamagaki, T. Gunji, Y. Hori, M. Tanaka, M. Kurokawa, Y. Katayose, and H. Ikeda</i>	
Measurement of J/ψ photoproduction in ultra-peripheral Au+Au collisions at $\sqrt{s_{NN}}=200$ GeV using the PHENIX detector	33
<i>A Takahara, H Hamagaki, T Gunji, Zaida Conesa del Valle, Yasuyuki Akiba, Mickey Chiu, Joakim Nystrand, Sebastian White, Kyrre Skjerdal, Ermiyas T. Atomssa</i>	
2. Accelerator and Instrumentation	
SHARAQ Project — Progress in FY2010 —	35
<i>S. Michimasa, T. Uesaka, S. Ota, Y. Sasamoto, K. Miki, S. Noji, H. Matsubara, H. Miya, H. Tokieda, S. Kasase, Y. Kikuchi, S. Sasano, H. Kurei, T. Kawabata, K. Yakou, N. Yamazaki, A. Yoshino, S. Shimoura, H. Sakai, T. Kubo, Y. Yanagisawa, H. Baba, G.P. Berg, P. Roussel-Chomaz, D. Bazin, for the SHARAQ collaboration</i>	
Development of CVD Diamond Detector	37
<i>S. Michimasa, M. Takaki, M. Dozono, S. Go, E. Ideguchi, K. Kisamori, H. Matsubara, H. Miya, S. Ota, H. Sakai, S. Shimoura, A. Stolz, Tsz Leung Tang, H. Tokieda, T. Uesaka, R.G.T. Zegers</i>	
Focus tuning method of the high-resolution beam line for the SHARAQ spectrometer	39
<i>Y. Sasamoto, T. Uesaka, T. Kubo, H. Takeda, and G.P.A. Berg</i>	
Performance test of low-pressure multi-wire drift chambers for SHARAQ beamline with high-intensity proton beam at the Pelletron Accelerator at RIKEN	41
<i>S. Noji, S. Ota, S. Kawase, Y. Kikuchi, K. Kisamori, M. Takaki, S. Michimasa, K. Miki, H. Miya</i>	
Performance of Low-Pressure Multi-Wire Drift Chamber for High-Intensity Heavy Ion beam	43
<i>H. Miya, S. Ota, H. Matsubara, S. Noji, Y. Kikuchi, K. Kisamori, M. Takaki, S. Michimasa, K. Miki, T. Uesaka, S. Shimoura</i>	
Development of two-alpha detection system in SHARAQ spectrometer for measurement of (^8He , ^8Be) reaction	45
<i>K. Kisamori, S. Shimoura, S. Michimasa, S. Ota, S. Noji, A. Tokieda, H. Baba</i>	
CNS Active Target Development and Test Experiment at HIMAC	47
<i>S. Ota, S. Michimasa, T. Gunji, H. Yamaguchi, H. Tokieda, T. Hashimoto, R. Akimoro, D. Kahl, M. Dozono, S. Hayakawa, S. Kawase, Y. Kikuchi, Y. Maeda, H. Matsubara, H. Otsu, S. Kubono, H. Hamagaki, T. Uesaka</i>	
Performance of Gas Electron Multiplier with Deuterium Gas	49

H. Tokieda, S. Ota, T. Hashimoto, S. Michimasa, M. Dozono, H. Matubara, Y. Kikuchi, T. Gunji, H. Yamaguchi, D. M. Kahl, R. Akimoto, H. Hamagaki, S. Kubono, and T. Uesaka

Development of position extraction for segmented Ge detectors by using pulse shape analysis	51
<i>S. Go, S. Shimoura, E. Ideguchi, S. Ota, H. Miya, H. Baba</i>	
Development of a Readout System for the GEM-based X-ray Imaging Detector	53
<i>A. Nukariya, H. Hamagaki, Y. Tanaka, T. Fusayasu, and T. Kawaguchi</i>	
Production of stable metallic ion beams of Hyper ECR ion source	55
<i>Y. Ohshiro, S. Yamaka, S. Watanabe, H. Muto and S. Kubono</i>	

3. Theoretical Nuclear Physics

Large scale nuclear shell-model calculations in CNS	57
<i>N. Shimizu, T. Otsuka, Y. Utsuno and T. Abe</i>	
Gamow-Teller Strengths in Ni Isotopes and Electron Capture Reactions	59
<i>T. Suzuki, M. Honma, and T. Otsuka</i>	
Symplectic structure and monopole strength in ^{12}C	61
<i>T. Yoshida, N. Itagaki and K. Katō</i>	

4. Other Activities

The 9th CNS-EFES Summer School(CNS-EFES10)	63
<i>S. Ota, S. Michimasa, N. Aoi, S. Fujii, H. Hamagaki, S. Kubono, T. Nakatsukasa, T. Otsuka, H. Sakai, S. Shimoura, T. Suzuki</i>	
Laboratory Exercise for Undergraduate Students	65
<i>S. Ota, S. Michimasa, H. Yamaguchi, A. Takaki, M. Takaki, K. Ozawa, S. Shimoura</i>	

Appendices

Symposium, Workshop, Seminar, PAC and External Review	67
CNS Reports	68
Publication List	69
Talks and Presentations	75
Personnel	81

Experimental Nuclear Physics: Low and Intermediate Energies

Excitation functions of ${}^7\text{Be}+\alpha$ elastic and inelastic scattering cross sections

H. Yamaguchi, T. Hashimoto^a, S. Hayakawa, D.N. Binh^g, D. Kahl, S. Kubono, T. Kawabata^b, T. Teranishi^c, Y. Wakabayashi^d, N. Iwasa^e, Y. Miura^e, Y.K. Kwon^f, L.H. Khien^g, and N.N. Duy^g

Center for Nuclear Study, Graduate School of Science, University of Tokyo

^a*RCNP, Osaka University*

^b*Department of Physics, Kyoto University*

^c*Department of Physics, Kyushu University*

^d*Advanced Science Research Center, JAEA*

^e*Department of Physics, Tohoku University*

^f*Department of Physics, Chung-Ang University*

^g*Institute of Physics and Electronics, Vietnam Academy of Science and Technology*

A measurement of ${}^7\text{Be}+\alpha$ elastic scattering was performed at CRIB [1, 2] in 2010, as reported previously [3]. This study was motivated in relation to the astrophysical ${}^7\text{Be}(\alpha, \gamma){}^{11}\text{C}$ reaction and the α -cluster structure in ${}^{11}\text{C}$. The measurement was performed using the thick target method in inverse kinematics [4], and the setup was essentially equivalent to the one in the measurement of the ${}^7\text{Li}+\alpha$ resonant elastic scattering [5]. A ${}^7\text{Be}$ beam of 2×10^5 per second was stopped in a target chamber filled with helium gas. The energy of recoiled α particle E_α was measured by silicon detectors, and converted to the center-of-mass energy E_{cm} , using the kinematical formula for the elastic scattering,

$$E_{\text{cm}} = E_\alpha \frac{m_4 + m_7}{4m_7 \cos^2 \theta_{\text{lab}}}, \quad (1)$$

where m_4 and m_7 are the masses of α and ${}^7\text{Be}$ particles, respectively, and θ_{lab} is the scattering angle in the laboratory frame. The energy loss of the recoiled α particle in the gas target was also considered in the calculation. The energy of the beam at any position in the gas target was obtained with a good precision (5% resolution or better), based on direct energy measurements at various target pressures, which was compared with an energy loss calculation using the SRIM [6] code. The differential cross section was calculated for each small energy division using the solid angle of the detector and the effective target thickness, both of which depend on the reaction position.

Measurements were also performed using an argon target having almost equivalent stopping power against the ${}^7\text{Be}$ beam. Differential cross sections were calculated assuming elastic scattering kinematics for both targets, as shown in Figure 1. We expected almost no α -particle events for argon-target runs as in the case of ${}^7\text{Li}+\alpha$ experiment, because of the high Coulomb barrier. However, we observed innegligible numbers of events as shown in Figure 1. They are considered as beam-like α particles produced at the production target as contaminants in the ${}^7\text{Be}$ beam, and reached to the silicon detectors at the end of the beamline. The sharp peak at 3.7 MeV corresponds to α particles which had the magnetic rigidity analyzed at the dipole magnets (D1 and D2) in CRIB. The lower-energy component is possibly α particles which had the same origin, but were scattered in a vacuum chamber. These beam-like particles should be

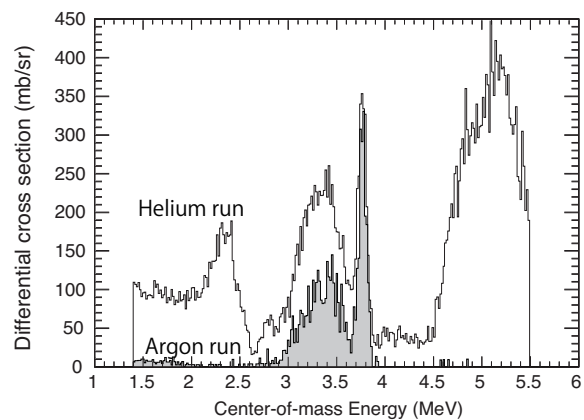


Figure 1. Energy spectra of differential cross section calculated using the kinematics of ${}^7\text{Be}+\alpha$ elastic scattering. The upper one is obtained with a helium gas target, and the lower one is with an argon gas target, showing the contribution of the background events.

mostly rejected by the Wien filter and by an event discrimination based on the timing information, but still remained in the obtained spectra. The heights of the sharp peak for both target runs are in a good agreement, but the lower energy component was significantly higher in the helium-target spectrum. This suggests the peak around 3-3.5 MeV observed in the helium-target spectrum is partly due to the beam-like α background, but the rest is by real scattering events. Thus, the background contribution was evaluated by the argon-target run data and subtracted from the helium-target spectrum. The resulting spectrum is mostly by the ${}^7\text{Be}+\alpha$ elastic scattering events, however, it still contains contribution from inelastic events.

Inelastic scattering events producing ${}^7\text{Be}^*$ at the first excited state were identified by measuring 429-keV γ rays with NaI detectors. We selected triple-coincidence events in which a ${}^7\text{Be}$ beam particle detected at the beam detector (MCP), an α or any other particle at the silicon detectors and a γ -ray at the NaI array. The γ -ray energy spectrum for those events is shown in Figure 2. The peak at 429 keV was clearly identified, and small peaks around 511 keV and 728 keV, which should be from positron annihilations

and excited ^{10}B produced via the $^7\text{Be}(\alpha, p)^{10}\text{B}^*$ reaction, were also observed. Selecting events in which an α particle

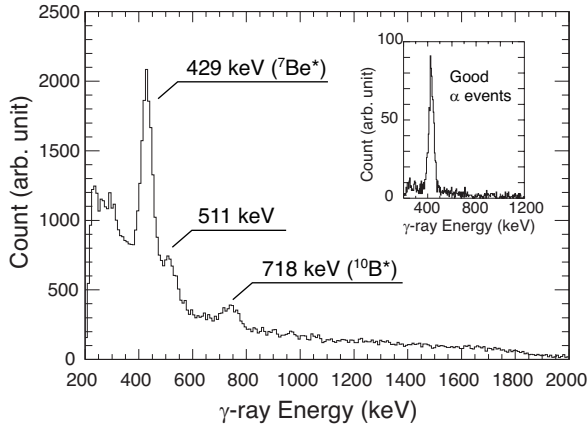


Figure 2. Energy spectrum of γ rays for ^7Be - α - γ triple-coincidence events. The insert shows the same spectrum for events with an α particle identified, after a beam position selection.

was identified and a ^7Be beam particle was measured at the MCP within a $20 \times 20 \text{ mm}^2$ square, an energy spectrum of γ -rays with a good signal-to-noise ratio was obtained, as shown in the insert of Figure 2. The photo-peak efficiency of the NaI array, measured at various position in the gas target, was used for calculating absolute cross section. Based on the γ -ray information, an excitation function of the inelastic scattering was obtained. Finally, the inelastic contribution was subtracted from the total differential cross section, and an excitation function of elastic scattering was obtained.

The excitation functions of the elastic and inelastic scatterings are shown in Figure 3. No previous measurements

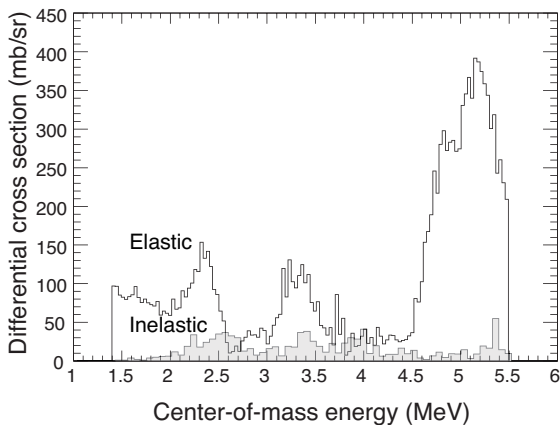


Figure 3. Excitation functions of $^7\text{Be}+\alpha$ elastic and inelastic scattering cross sections.

to be directly compared with these excitation functions are known. In the present excitation function of the elastic scattering, a structure having several peaks, which should correspond to the resonance structure in ^{11}C , was observed. We

expect that the parameters of these resonances could be determined by performing an R-matrix analysis. The overall uncertainty in E_{cm} was estimated as 70–130 keV, depending on the energy. The uncertainty mainly originated from the energy straggling of the ^7Li beam and α particles (30–80 keV), the energy resolution of the ΔE -E detector (20–55 keV), and angular uncertainty due to the finite size of the detector (20–100 keV). The present excitation function is for θ_{cm} 160–180°, and the average θ_{cm} is 170°.

The statistics of inelastic events was not sufficient to discuss the detailed structure, but the differential cross section was about 30 mb/sr at maximum, one order of magnitude smaller than that of the elastic scattering.

In summary, we successfully obtained excitation functions of $^7\text{Be}+\alpha$ elastic scattering and inelastic scattering to the first excited state of ^7Be . We will perform an R-matrix analysis to determine resonance parameters, which are not known precisely from previous measurements. The α widths would provide valuable information for the α -cluster structure in the high excited states of ^{11}C , and astrophysical $^7\text{Be}(\alpha, \gamma)$ reaction rate in high-temperature phenomena.

References

- [1] S. Kubono *et al.*, *Eur. Phys. J. A* **13** (2002) 217.
- [2] Y. Yanagisawa *et al.*, *Nucl. Instrum. Methods Phys. Res., Sect. A* **539** (2005) 74.
- [3] H. Yamaguchi *et al.*, *CNS Annual Report 2009* (2011).
- [4] K. Artemov *et al.*, *Sov. J. Nucl. Phys* **52** (1990) 408.
- [5] H. Yamaguchi *et al.*, *Phys. Rev. C* **83** (2011) 034306.
- [6] J. Ziegler, J. Biersack, and M. Ziegler, *SRIM The Stopping and Range of Ions in Matter* (Lulu Press, Morrisville, USA, 2008).

Present status of the direct measurement of the $^{18}\text{Ne}(\alpha, p)^{21}\text{Na}$ reaction cross sections using the GEM - MSTPC

T. Hashimoto, S. Kubono, H. Yamaguchi, S. Hayakawa, D. Kahl, S. Ota, S. Michimasa, H. Tokieda, K. Yamaguchi^a, I. Arai^a, T. Komatsubara^a, H. Ishiyama^b, Y.X. Watanabe^b, H. Miyatake^b, Y. Hirayama^b, N. Imai^b, S. C. Jeong^b, Y. Mizoi^c, S. K. Das^c, T. Fukuda^c, H. Makii^d, Y. Wakabayashi^d, N. Iwasa^e, T. Yamada^e, A. A. Chen^e, J. J. He^g,

Center for Nuclear Study, Graduate School of Science, University of Tokyo

^a*Graduate School of Pure and Applied Sciences, University of Tsukuba*

^b*Institute of Particle and Nuclear Studies (IPNS), High Energy Accelerator Research Organization (KEK)*

^c*Research Center for Physics and Mathematics, Faculty of Engineering, Osaka Electro-Communication University*

^d*Advanced Science Research Center, Japan Atomic Energy Agency (JAEA)*

^e*Department of Physics, Tohoku University*

^f*Department of Physics and Astronomy, McMaster University*

^g*Institute of Madam Physics*

1. Introduction

The $^{18}\text{Ne}(\alpha, p)^{21}\text{Na}$ reaction is considered as one of the main possible breakout routes from the hot - CNO cycle to the rp - process. This reaction is considered to be dominant at around $T = 0.6 - 4.0$ GK which corresponds to the Gamow energy of 0.5 - 3.4 MeV.

Although several experimental efforts on the $^{18}\text{Ne}(\alpha, p)^{21}\text{Na}$ reaction have been made in this energy region [1], the information is very limited yet. In order to determine the reaction rate, the cross sections in the energy region are needed. However no direct measurement of the reaction cross section for that process have been successfully performed yet in this energy region.

We planned to directly measure the excitation function of the $^{18}\text{Ne}(\alpha, p)^{21}\text{Na}$ reaction in the low energy region using a sophisticated active target type detector system, Multiple Sampling and Tracking Proportional Chamber with Gas Electron Multiplier (GEM-MSTPC). Figure 1 shows the experimental setup, which consists of a beam monitor, the GEM - MSTPC, and a Si detector array.

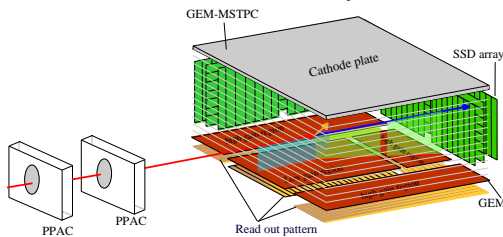


Figure 1. Experimental setup for the $^{18}\text{Ne}(\alpha, p)^{21}\text{Na}$ reaction.

The beam monitor consists of two PPACs. It provides the time-of-flight information and trajectory for each incident secondary beam. Absolute beam energy and injected angle are obtained from these information of these values on event by event.

The Si detector array is set just outside the gas sensitive area of the GEM -MSTPC in order to measure the energies and directions of protons. The telescope consists of 18 Si detectors. Each Si detector is 90×90 mm² in size and 450 μm in thickness with 9 readout strips. The solid angle

and the angular range are 15% of 4π and 0 - 115 degrees, respectively.

The main component GEM - MSTPC has a structure based on the MSTPC [4, 5], It can measure the three dimensional trajectories and the energy loss of all relevant charged particles of reaction, which makes it possible to identify the true reaction events. In order to relax the limitation in beam injection rate, we adopted a Gas Electron Multiplier (GEM) [6] in substitution for a multi-wire proportional counter used in the MSTPC.

The GEM - MSTPC consists of a drift space region and GEMs and readout pads. The drift space region has an active volume of 295 mm long, 278 mm wide and 100 mm high. The active region consists of a low - gain regions for measurement of beam and/or recoil particles, and three high - gain regions for measurement of emitted protons. Each region consists of one or more GEM foils and a position sensitive read - out pads. Gas mixture of 90% ^4He and 10% CO_2 at 0.21 atmosphere is used .

The feasibility of the experiment, the result of ^{18}Ne beam production and high beam injection rate capability of the GEM - MSTPC except for the drift velocity were discussed in Ref. [2, 3]. In this report, the beam injection rate dependence of the electron drift velocity of the GEM - MSTPC and the preliminary results of the $^{18}\text{Ne}(\alpha, p)^{21}\text{Na}$ reaction measurement are described.

2. Beam injection rate dependence of the electron drift velocity

We adopted the 200 μm - thick GEM foil, since our requirements on gas gain, gain stability, position resolution and energy resolution, were satisfied with this foil up to 420 kpps of heavy ion injection rate [3].

The remaining problem is position distortion of the electron drift direction. Ion feed back ratio can be made less than 2% using 200 μm - thick GEM under the same field condition of Ref [7]. In order to judge whether this ratio is acceptable or not, we have performed a test experiment at the pelletron accelerator facility of RIKEN. The injected beam was ^4He with energy of 4.5 MeV. The position dis-

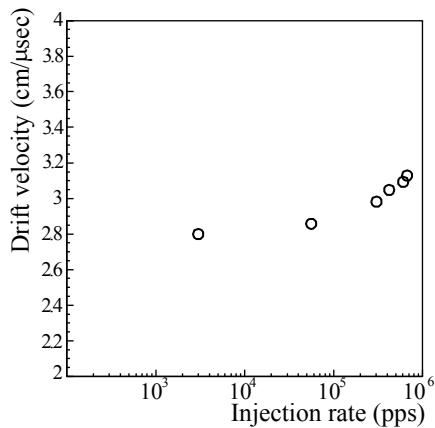


Figure 2. The results of the test experiment of the high beam injection rate dependence of the electron drift velocity. The horizontal axis indicates the beam injection rate, and the vertical axis is the electron drift velocity.

tortion was tested by varying the beam intensity from 200 pps to 700 kpps. The event trigger was made by a silicon solid detector which was set just downstream side of the GEM - MSTPC.

The experimental result is shown in fig 2. The horizontal axis indicates the beam injection rate, and the vertical axis is the electron drift velocity. This result indicates that the electron drift velocity depends on weakly on the beam injection rate. Since the field distortion due to ionized by injected beam is about 1.1% at 10^6 pps heavy ion beam injection according to our calculation, the main source is ion feed back from the GEM foils. From the present result, the position distortion in the drift direction is estimated to be 3.6 mm for the 400 kpps beam injection. The value is a little over our original requirement of 2 mm. However this is not a serious problem. Since this phenomena is occurred at around beam ray, this position distortion can be corrected by beam monitor information. We judged that the GEM - MSTPC can be used to our experiment with the satisfied performance.

3. Direct measurement of the $^{18}\text{Ne}(\alpha, p)^{21}\text{Na}$ reaction

We have performed a new direct exclusive measurement of the $^{18}\text{Ne}(\alpha, p)^{21}\text{Na}$ reaction at the CNS Radioactive Ion Beam Separator (CRIB) facility [8]. ^{18}Ne beam was produced via the $^3\text{He}(^{16}\text{O}, ^{18}\text{Ne})n$ reaction. The ^{16}O beam, with energy of 6.8 MeV/u and the averaged intensity of 560 particle nA, was irradiated on a cryogenic gas target [9] of ^3He . The typical energy, intensity and purity of ^{18}Ne beam were 3.7 MeV/u, 326 kpps and 81.6%, respectively. Obtained intensity and beam purity were as expected from the test production [3].

A typical ΔE - E plot for ^{18}Ne injected events is shown in fig. 3, in which protons are clearly separated from α particles which stop inside the first layer of Si telescope. We first concentrate proton detected events.

Figure 4 shows a typical reaction event. This event is found in the proton detected events at ΔE - E telescope and an energy - loss pattern is different from beam through events. Because there is very high possibility.

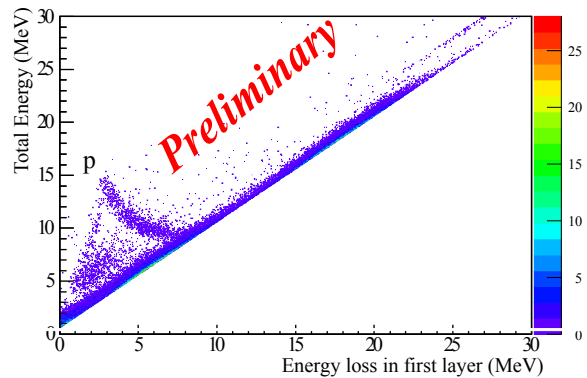


Figure 3. Typical ΔE - E plot. Detected protons and α - particles are indicated as “ α ” and p, respectively.

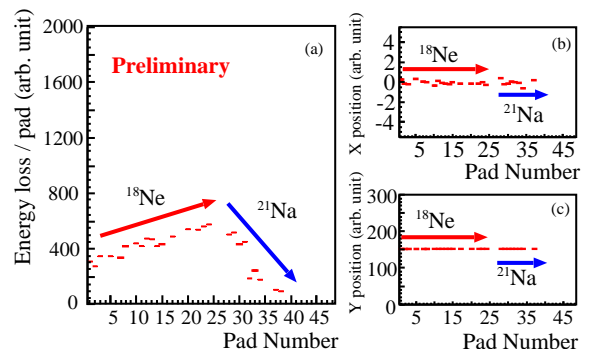


Figure 4. Typical event pattern of $^{18}\text{Ne}(\alpha, p)^{21}\text{Na}$ reaction. Left figure (a) shows energy loss per pad versus the number of pads. Right figures show the horizontal (b) and vertical (c) projections of the three dimensional particle trajectories. The vertical axes of these figures indicate the horizontal and vertical positions, respectively.

4. Summary

We have developed the GEM - MSTPC which is a sophisticated active target type detector for measurements of (α , p) reaction of astrophysical interest. It is demonstrated that the GEM - MSTPC have satisfied performances for the experiments.

Direct measurement of the $^{18}\text{Ne}(\alpha, p)^{21}\text{Na}$ reaction have been performed at CRIB. Analysis is still in progress to get an excitation function of $^{18}\text{Ne}(\alpha, p)^{21}\text{Na}$ reaction.

References

- [1] J. J. He *et al.*, Eur. Phys. J. A **36** (2008) 1, and references therein.
- [2] T. Hashimoto *et al.*, CNS Annual Rep. 2008 17.
- [3] T. Hashimoto *et al.*, CNS Annual Rep. 2009 9.
- [4] Y. Mizoi *et al.*, Nucl. Instrum. Meth. A **431** (1999) 112.
- [5] T. Hashimoto *et al.*, Nucl. Instrum. Meth. A **556** (2006) 339.
- [6] F. Sauli Nucl. Instrum. Meth. A **386** (1997) 531.
- [7] K. Yamaguchi *et al.*, Nucl. Instrum Meth A, **623** (2010) 135.
- [8] S. Kubono, *et al.*, Nucl. Phys. A **558** (1995) 305.
- [9] H. Yamaguchi, *et al.*, Nucl. Instrum. Meth A **589** (2008) 150.

High-Spin Level Structure in ^{35}S

E. Ideguchi, S. Go, H. Miya, K. Kisamori, M. Takaki, S. Ota, S. Michimasa, S. Shimoura, T. Koike^a, T. Yamamoto^a, K. Shirotori^a, Y. Ito^b, J. Takatsu^b, T. Suzuki^c, T. Morikawa^d, M. Oshima^e, M. Koizumi^e, Y. Toh^e, A. Kimura^e, H. Harada^e, K. Furutaka^e, S. Nakamura^e, F. Kitatani^e, Y. Hatsukawa^e, T. Shizuma^e, M. Sugawara^f, Y.X. Watanabe^g, and Y. Hirayama^g

Center for Nuclear Study, Graduate School of Science, University of Tokyo

^a*Department of Physics, Kyushu University*

^b*Department of Physics, Tohoku University*

^c*Department of Physics, Osaka University*

^d*RCNP, Osaka University*

^e*Japan Atomic Energy Agency*

^f*Chiba Institute of Technology*

^g*Institute of Particle and Nuclear Studies, High Energy Accelerator Research Organization (KEK)*

Recent experimental studies elucidated superdeformed (SD) structures in the excited levels of $A \sim 40$ nuclei whose ground state is spherical [1–4]. The systematical presence of SD structure in this mass region is qualitatively understood by the superdeformed shell structures related to the $N, Z=18, 20, 22$ SD magic numbers. Another SD magic number of $N=Z=16$ is predicted and the associated SD structure has been expected in ^{32}S for a long time [5], but it has not yet been observed and remains as a great challenge. Cranked Skyrme-Hartree-Fock calculations predict the SD structure in a range of sulfur isotopes [6]. ^{36}S and adjacent isotope ^{35}S are candidates of SD nuclei. However, spectroscopic studies of sulfur isotopes are not well explored and only low-lying levels near the ground state are studied.

In order to clarify high-spin levels and to investigate collective structure in ^{35}S , we have performed an in-beam γ -ray spectroscopy experiment. ^{35}S is a nucleus with $Z=16$ and $N=19$, and the spin-parity of the ground state is $3/2^+$ due to the neutron hole in $d_{3/2}$ orbital. At 1.991 MeV, there is a $7/2^-$ isomeric state associated with a promotion of one neutron from the sd shell to the $f_{7/2}$ orbital. In the previous study [7], we found several γ transitions in coincidence with the 1991 keV transition. Based on the γ - γ coincidence analysis, excited levels up to 7.18 MeV were found. Spin assignment of the excited levels were performed based on the DCO (Directional Correlation from Oriented nuclei) analysis [8], but due to the limited counting statistics, spin-parity of the levels could not firmly identified. In order to identify the multipolarities of each γ transitions and to assign the spins and parities of the excited levels, linear polarization measurements of γ rays have been performed.

The experiment was performed at the Cyclotron and Radioisotope Center (CYRIC), Tohoku University. High-spin states in ^{35}S were studied using a $^{26}\text{Mg}(^{18}\text{O}, 2\alpha 1n)^{35}\text{S}$ fusion-evaporation reaction at a beam energy of 70 MeV. A ^{26}Mg target of 0.47 mg/cm^2 with $13.2 \text{ mg/cm}^2 \text{ Pb}$ backing was used. Prompt γ rays were detected by Hyperball-2 array composed of 6 coaxial Ge detectors and 6 Clover Ge detectors in this experiment. Clover Ge detectors were placed at 90° and coaxial detectors were placed at $\sim 134^\circ$ relative to the beam direction. Each Ge detectors was shielded with

BGO counters for Compton background suppression. Evaporated charged particles in the reaction were detected by the Si-Ball charged particle filter [9] which consist of 30 Si detectors mounted on the truncated icosahedron shaped frame. Ten pentagonal and twenty hexagonal shaped Si ΔE detectors of $170 \mu\text{m}$ thickness were used. In front of each Si detector, thin Al absorber foil is mounted in order to prevent ^{18}O beam directly hitting the detector after scattering at the target.

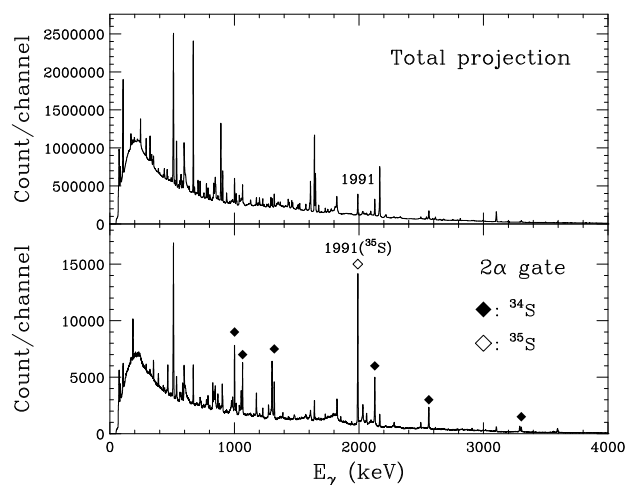


Figure 1. Total γ - γ coincidence spectrum (upper panel) and a γ -ray spectrum obtained by gating the events with two alpha particles detected in the experiment.

With a trigger condition of more than two Compton suppressed Ge detectors firing, a total number of 3.8×10^8 events were collected. Figure 1 shows a total projection (upper panel) of γ - γ coincidence data and a spectrum gating on two α particle detected (lower panel). As seen in the figure, γ -ray peaks associated with ^{34}S and ^{35}S were clearly identified by the charged-particle gates.

In this experiment, Clover Ge detectors were used as polarimeters for measuring linear polarization of γ rays to determine the electric or magnetic character of transitions. Linear polarization of γ rays is estimated by measuring an experimental asymmetry,

$$A(E_\gamma) = \frac{N_\perp - N_\parallel}{N_\perp + N_\parallel}.$$

Here, N_\perp and N_\parallel denotes the number of counts of Compton scattered events perpendicular and parallel to the beam direction, respectively. This ratio is proportional to the degree of polarization P and it depends on the photon energy;

$$A(E_\gamma) = Q(E_\gamma)P(E_\gamma),$$

where the factor Q corresponds to the polarization sensitivity of the polarimeter. Since Q is always positive, it is sufficient to use $A(E_\gamma)$ to identify whether transition is electric or magnetic in character. Stretched electric transitions give rise to a positive and magnetic transitions to a negative value of $P(E_\gamma)$.

This method is demonstrated in a γ -ray spectrum obtained by subtracting the spectrum of N_\perp from that of N_\parallel as shown in Fig. 2. Previously known γ -ray peaks of magnetic transitions appear in positive side while electric transitions in negative side.

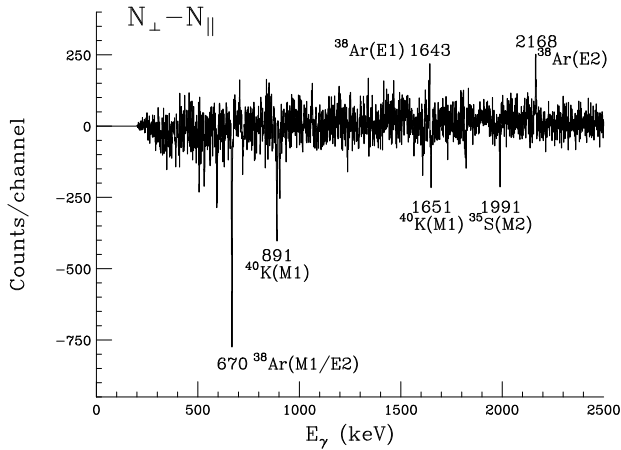


Figure 2. Experimental asymmetry γ -ray peaks of ^{35}S detected in the Clover Ge detectors (see text).

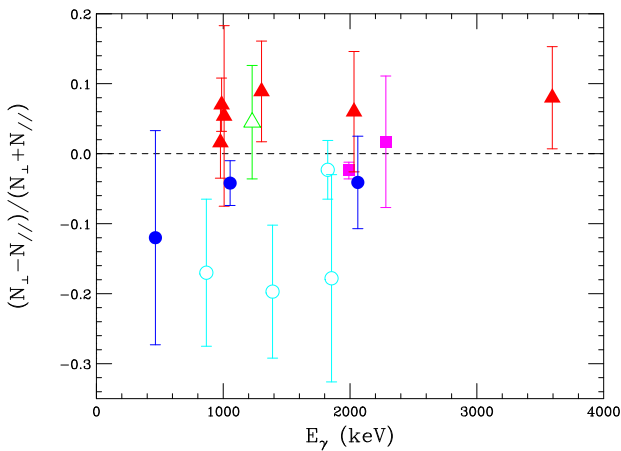


Figure 3. Experimental asymmetry of each γ -ray peaks in ^{35}S detected in the Clover Ge detectors (see text).

Deduced asymmetries of newly observed γ -ray transitions in ^{35}S are plotted in Fig. 3. In the plot, filled trian-

gles, an open triangle, and filled squares appearing in the positive side are assigned as E2, E1, and E3/M2 transitions, respectively. Data points in negative side with filled circles and open circles are assigned as pure M1 and M1/E2 mixed transitions, respectively. Based on this result with the results of DCO analysis, we are going to identify the multiplicities of each γ -ray transitions in ^{35}S . Data analysis is in progress.

References

- [1] E. Ideguchi *et al.*, Phys. Lett. B **686**, 18-22 (2010).
- [2] C.E. Svensson *et al.*, Phys. Rev. Lett. **85**, 2693-2696 (2000).
- [3] E. Ideguchi *et al.*, Phys. Rev. Lett. **87**, 222501/1-4 (2001).
- [4] C.D. OfLeary *et al.*, Phys. Rev. C **61**, 064314/1-7 (2000).
- [5] I. Ragnarsson, S.G. Nilsson, R.K. Sheline, Phys. Rep. **45**, 1 (1978).
- [6] T. Inakura *et al.*, Nucl. Phys. A **728**, 52-64 (2003).
- [7] E. Ideguchi *et al.*, CNS Ann. Rep. **2009**, 23 (2010).
- [8] K.S. Krane, R.M. Steffen and R.M. Wheeler, Nucl. Data Tables, **11**, 351-406 (1973).
- [9] T. Kuroyanagi *et al.*, Nucl. Instrum. Methods Phys. Res. A **316**, 289-296 (1992).

Spectroscopic study of ${}^9\text{He}$ via the double charge exchange (${}^{18}\text{O}, {}^{18}\text{Ne}$) reaction

H. Matsubara^a, M. Takaki^a, T. Uesaka^b, S. Shimoura^a, N. Aoi^c, M. Dozono^b, T. Fujii^a,
 K. Hatanaka^c, T. Hashimoto^c, T. Kawabata^d, S. Kawase^a, K. Kisamori^a, Y. Kikuch^a, Y. Kubota^a,
 C.S Lee^a, H.C. Lee^b, Y. Maeda^e, S. Michimasa^a, K. Miki^c, H. Miya^a, S. Noji^a, S. Ota^a,
 S. Sakaguchi^f, Y. Sasamoto^a, T. Suzuki^c, L.T Tang^a, K. Takahisa^c, H. Tokieda^a, A. Tamii^c,
 K. Yako^g, Y. Yasuda^c, N. Yokota^d, R. Yokoyama^a, and J. Zenihiro^b

^aCenter for Nuclear Study, Graduate School of Science, University of Tokyo

^bRIKEN (The Institute of Physical and Chemical Research)

^cResearch Center for Nuclear Physics (RCNP), Osaka University

^dDepartment of Physics, Kyoto University

^eDepartment of Applied Physics, Miyazaki University

^fDepartment of Physics, Kyusyu University

^gDepartment of Physics, University of Tokyo

1. Introduction

The ${}^9\text{He}$ nucleus has the largest A/Z ratio of 4.5. Although it is unbound, the first excited state of ${}^9\text{He}$ is reported to have a remarkably narrow width at a level of 100 keV [1]. Because the ${}^{10}\text{He}$ ground state is also unbound, neutron pickup reactions, such as (p, d) and (d, t) reactions, can not be applied to investigate the level structure of ${}^9\text{He}$. Thus, small number of works have been devoted to study the energy levels, widths and spin-parities in ${}^9\text{He}$. Most of their spin-parities and widths, however, are still uncertain or scarcely known, as summarized in Table 1.

We have developed a new powerful probe to study neutron rich nuclei, which is the heavy ion double charge exchange (HIDCX) measurement via the (${}^{18}\text{O}, {}^{18}\text{Ne}$) reaction by making use of the high resolution spectrometer Grand Raiden (GR) at the Research Center for Nuclear Physics (RCNP), Osaka University. This probe has noticeable advantages *i.e.* (a) unstable nucleus can be investigated even by using stable nuclei for a target and for a beam, (b) missing mass measurement enables us to observe an excitation energy spectrum both below and above the particle threshold, (c) out-going particles of ${}^{18}\text{Ne}$ can be clearly identified through the spectrometer because the ${}^9\text{B}$ nucleus is unbound and thus an A/Q value for ${}^{18}\text{Ne}$ is unique, and (d) the HIDCX transition rate between ${}^{18}\text{O}$ and ${}^{18}\text{Ne}$ is expected to be relatively large because of overlapping for their wavefunctions in r -space, which arises from the fact that they are in the super-multiplet members. It should be noted that the advantage (d) is essential for the HIDCX measurement since a double charge exchange transition is considered to be a two-step reaction and its rate is usually small. Therefore, the (${}^{18}\text{O}, {}^{18}\text{Ne}$) reaction that has a large transition rate would provide us to investigate the nucleus ${}^9\text{He}$ from the stable nucleus ${}^9\text{Be}$.

2. Experimental setup

The experiment was performed at the WS course of the RCNP. A primary beam of ${}^{18}\text{O}$ was accelerated up to 1432 MeV (79.6 MeV/nucleon), which is the maximum at the RCNP, by the coupled cyclotrons. A typical beam in-

Table 1. Energy levels and widths in ${}^9\text{He}$.

E_x (MeV)	J^π	Γ (MeV)
0.0	$1/2^+$	
1.10	$1/2^-$	0.1
2.26		0.7
4.2		
5.0		
8.0		

tensity was 20 pA. A typical beam energy resolution was 1 MeV (FWHM) including an effect due to the detector system. The ${}^{18}\text{O}$ beam bombarded a self-supporting foil target of ${}^9\text{Be}$ with an areal density of 5.0(1) mg/cm², where the natural abundance in beryllium is 100%. The scattered particles were momentum-analyzed by the GR spectrometer. Then, they were detected by the focal plane detector system, which consists of two vertical drift chambers (VDC's) and two plastic scintillators. Thicknesses of the two scintillators were 1 and 3 mm. Coincident signals from the scintillators were used to trigger the data acquisition (DAQ) system. A momentum acceptance of the GR was limited for it to be half by setting steel plates at the focal plane, which reduced the trigger rate for the DAQ system. A typical DAQ rate was reduced to 6 kcps, and the typical live efficiency recovered to 80%. The measurable region in excitation energy for ${}^9\text{Be}$ was from -20 to 50 MeV.

The GR spectrometer was placed at 0°. We adopted an under-focus mode, which gives a better vertical scattering angle resolution, by reducing a magnetic field of the first quadrupole magnet (Q1) in the GR to -10% from the standard setting. The total scattering angle resolution of 5 mr (FWHM) was achieved by the calibration using a sieve-slit. The angle acceptance of the GR spectrometer was ± 20 and ± 45 mr for the horizontal and the vertical direction, respectively, which covers $0-8^\circ$ for scattering angles in center of mass frame.

The primary beam was stopped by the D1 Faraday cup

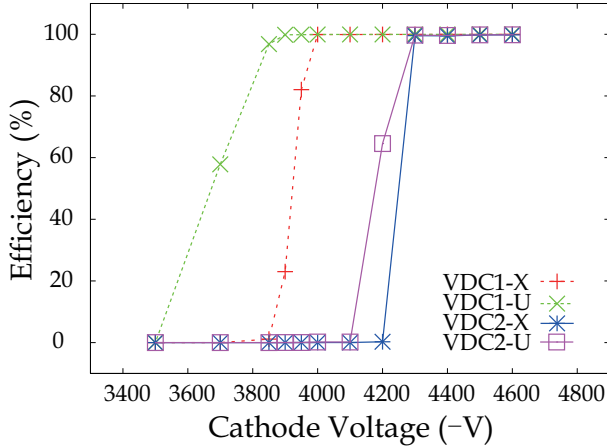


Figure 1. Voltage dependence of hit wire efficiency for the vertical drift chambers at the GR in the case of ^{18}O beam at 1432 MeV (79.6 MeV/nucleon). The gas mixture for the VDC1 is Ar : Isobutane=70 : 30, and that for the VDC2 is 50 : 50.

(D1FC) which located at the high momentum side of the exit of the first dipole (D1) magnet of the GR. It is made of carbon block of 4 cm thick in the beam direction. The total beam charge was measured by the D1FC, which was 7.7 mC. By the irradiation with an intensity of 20 pA, the temperature of the D1FC, which was monitored by using a Pt-100, rapidly increased to be over 200°C within 30 minutes.

3. Optimized parameters of the vertical drift chambers for heavy ion

Although many experiments employing light ion beam have been performed with the GR spectrometer so far, the VCD's have not been used to detect heavy ion particles that are larger than $Z \geq 4$. Thus, we optimized parameters to operate the VDC's in the case of the heavy ion ^{18}O ($Z = 8$).

The two VDC's were operated with different gas mixtures with a pressure of 1 atm: the first VDC (VDC1) with a mixture of Ar : Isobutane=70 : 30 and the second VDC (VDC2) with Ar : Isobutane=50 : 50. Since isobutane gas works as quencher in a process of electron avalanche, higher voltages can be supplied to the VDC2. Figure 1 shows the detection efficiency of VDC's as a function of high-voltage applied on the cathode plane. The voltage to the potential wires was fixed to be -300 V. The hit wire efficiency is defined as a ratio of the number of events in which more than two wires are fired to the total event number. Dotted curves correspond to responses of VDC1 (X- and U-planes), while solid lines to those of VDC2. From this result, we have determined to apply the voltages of -4500 V and -300 V to the cathode planes and the potential wires, respectively, with the gas mixture of Ar : Isobutane=50 : 50.

4. Result and discussion

The particle identification to select ^{18}Ne was realized by using the information of Time-of-Flight between RF signals and the trigger scintillators and by making use of its unique A/Q value. Detailed descriptions for the analysis may be found in Ref. [2]. The excitation energy spectrum reconstructed for ^9He via the HIDCX reaction is shown in Fig. 2,

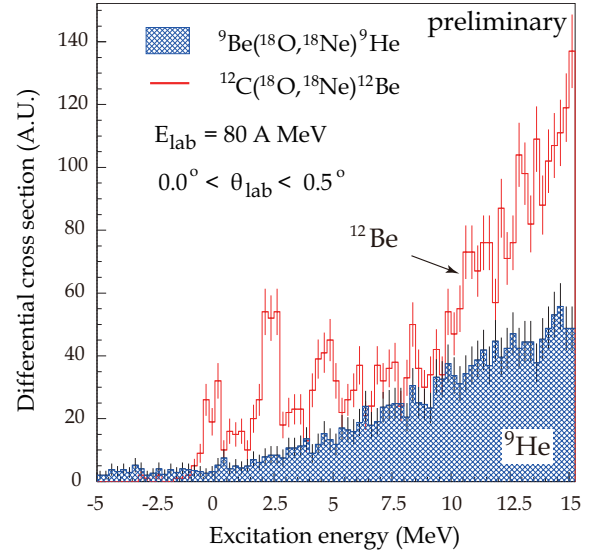


Figure 2. Typical excitation energy spectra for the $^9\text{Be}(^{18}\text{O}, ^{18}\text{Ne})^9\text{He}$ and the $^{12}\text{C}(^{18}\text{O}, ^{18}\text{Ne})^{12}\text{Be}$ [2] reactions at $\theta_{lab} = 0-0.5^\circ$.

comparing with that for ^{12}Be [2]. It is obvious that no peaks are observed in the spectrum for ^9He , while peaks owing to the HIDCX reaction are clearly observed in that for ^{12}Be . The difference shows that the transition rate from ^9Be to ^9He is much weaker than that from ^{12}C to ^{12}Be . This may be figured out as the ground state of ^9Be is well deformed due to a cluster-like structure [3]. The present result indicates that the HIDCX reaction at 80 MeV/nucleon is a good probe for the study of nuclear structure. Detailed comparison of reaction calculations with experimental data is in progress.

References

- [1] H.G. Bohlen *et al.*, Prog. Part. Nucl. Phys. **42** (1999) 17-26.
- [2] M. Takaki *et al.*, CNS Ann. Rep. 2010 (2012).
- [3] C. Scholl *et al.*, Phys. Rev. C **84** (2011) 014308.

Measurement of the $^{90}\text{Zr}(^{12}\text{N}, ^{12}\text{C})^{90}\text{Nb}$ reaction at 200 MeV/nucleon

S. Noji¹, H. Sakai^a, N. Aoi^{a,2}, H. Baba^a, G. P. A. Berg^b, R. Chen^a, P. Doornenbal^a, M. Dozono^{c,3}, N. Fukuda^a, N. Inabe^a, D. Kameda^a, T. Kawabata^d, S. Kawase^c, Y. Kikuchi^c, K. Kisamori^c, T. Kubo^a, Y. Maeda^e, H. Matsubara^c, S. Michimasa^c, K. Miki², H. Miya^c, H. Miyasako^e, S. Sakaguchi^{a,4}, Y. Sasamoto^c, S. Shimoura^c, M. Takaki^c, H. Takeda^a, S. Takeuchi^a, H. Tokieda^c, T. Ohnishi^a, S. Ota^c, T. Uesaka^{c,3}, H. Wang^a, K. Yako, Y. Yanagisawa^a, N. Yokota^d, K. Yoshida^a

^aDepartment of Physics, University of Tokyo

^aRIKEN (The Institute of Physical and Chemical Research)

^bJoint Institute for Nuclear Physics and the Department of Physics, University of Notre Dame

^cCenter for Nuclear Study, Graduate School of Science, University of Tokyo

^dDepartment of Physics, Kyoto University

^eDepartment of Applied Physics, University of Miyazaki

The existence of the isovector spin monopole resonance (IVSMR) has long been an issue to be clarified. The IVSMR [2] is a coherent $2\hbar\omega$ $1p$ - $1h$ excitation with $\Delta L = 0$ and $\Delta S = \Delta T = 1$ driven by the operator $\hat{O}_{\pm} \equiv \sum_k t_{\pm}(k) \sigma_{\mu}(k) r(k)^2$. The energy centroid and width of the IVSMR can be related to, for example, the isovector spin-incompressibility, the effective interaction in a spin-isospin channel, etc. From the model independent sum rule $\mathcal{S}_- - \mathcal{S}_+ = 3(N\langle r^4 \rangle_n - Z\langle r^4 \rangle_p)$, with $\mathcal{S}_{\pm} = \sum_{\mu} \sum_m |\langle m | \hat{O}_{\pm} | 0 \rangle|^2$, one can deduce a quantity $\delta_{np} = \sqrt[4]{\langle r^4 \rangle_n} - \sqrt[4]{\langle r^4 \rangle_p}$, which is related to the neutron skin thickness and then places a strong constraint on the neutron matter equation of state. Although important, experimental information on the IVSMR has been scarce [3, 4].

In October 2010, we performed an experiment to search for IVSMR in ^{90}Nb via the $^{90}\text{Zr}(^{12}\text{N}, ^{12}\text{C})^{90}\text{Nb}$ reaction at 200 MeV/nucleon. This reaction is referred to as *the exothermic charge-exchange reaction* because of its positive reaction Q -value ($Q_{\text{gg}} > 0$). This reaction has the following advantages for the IVSMR study: (1) This reaction can realize high excitation energy transfer with only a small momentum transfer, thanks to the large mass difference (~ 17 MeV) between the projectile and ejectile. This kinematical condition is preferable for the excitation of $\Delta L = 0$ mode. (2) This reaction is sensitive to the surface region because of strong absorption. Therefore IVSMR, whose transition density has a node at the surface, can be strongly excited. (3) This reaction has the selection rule $\Delta S = \Delta T = 1$; thus, it exclusively excites isovector spin-flip modes.

However, this reaction has two types of major background processes. One is due to the in-flight β decay of the ^{12}N projectile, whose half-life is 11.0 ms. This process produces ^{12}C nuclei, the amount of which is comparable to that of the true charge-exchange reaction products, and these are not separable with the response of the focal plane detectors. The other is due to the Fermi transition of ^{12}N

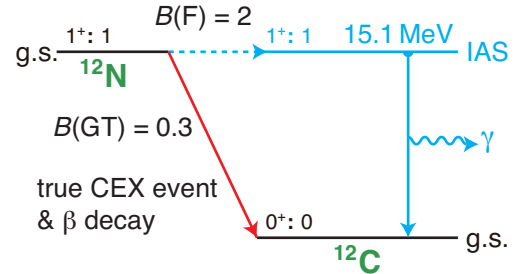


Figure 1. Energy relationship between ^{12}N and ^{12}C .

to the excited state in ^{12}C at 15.1 MeV, which is the IAS of the ground state of ^{12}N . The transition has a relatively large $B(F)$ value of 2, unlike the transition to the ground state, which has $B(GT) = 0.3$. This relationship is depicted in Fig. 1. This Fermi transition excites the IAS and the isovector non-spinflip monopole resonance in ^{90}Nb , and the $^{12}\text{C}^*(\text{IAS})$ mainly decays directly to the ground state by γ decay.

We performed the experiment at the RIBF by using the BigRIPS, the High Resolution Beam Line, and the SHARAQ Spectrometer. The experimental setup is shown in Fig. 2. The primary beam of ^{14}N , accelerated by AVF, RRC, and SRC up to 250 MeV/nucleon, bombarded the Be target at F0 with a thickness of 5 mm. The secondary ^{12}N beam was produced via projectile fragmentation and was separated in BigRIPS. The Al degrader at F1 with a thickness of 15 mm was used to increase the purity of the ^{12}N beam. The emittance of the beam was reduced with a momentum slit at F1 to $|\delta p/p| = 0.2\%$, and with an angular collimator at F2 to $|\delta\theta/\theta| = 10$ mrad and $|\delta\phi/\phi| = 25$ mrad. The beam was transported to the target in the dispersion matching mode [5]. A position-sensitive segmented scintillation detector at F3 [6] and two MWDCs at F-H10 [7] were used to measure the trajectories of the beam during the measurement. A plastic scintillator with a thickness of 1 mm was also installed at F3 for the timing reference. The reaction target used here was ^{90}Zr with a

¹Present address: Center for Nuclear Study, Graduate School of Science, University of Tokyo.

²Present address: Research Center for Nuclear Physics, Osaka University.

³Present address: RIKEN (The Institute of Physical and Chemical Research).

⁴Present address: Department of Physics, Kyushu University.

thickness of $150\text{mg}/\text{cm}^2$. The reaction product was momentum analyzed by SHARQA and detected at the focal plane by two CRDCs [8] and three plastic scintillators with thicknesses of 5, 10, 20 mm.

In this experiment, we aimed to verify the usefulness of the method by employing a setup to remove these two types of backgrounds. For the estimation of the background due to the β decay, we installed a pair of 1 mm-thick plastic scintillators at $\sim 8\text{mm}$ up- and downstream of the ^{90}Zr target in order to determine the charges of the incoming and outgoing particles and to separate the true charge-exchange events from the β decay events. For the estimation of the background due to the Fermi transition of the projectile, we installed the NaI(Tl) array DALI2 around the target chamber for the detection of γ rays with $E_\gamma = 15.1\text{MeV}$ from the de-excitation of $^{12}\text{C}^*(\text{IAS})$. In order to estimate the detection efficiency of the 15.1 MeV γ rays, we performed Monte Carlo simulations. The estimated efficiency was $38 \pm 5\%$ with the threshold level of 8 MeV.

The beam was stable throughout the experiment; the maximum intensity of the primary beam was 400 pA. The counting rate and the purity of the ^{12}N beam were 1.4 Mcps and 90%, respectively. Double-differential-cross-section data were successfully obtained along with the γ -ray data taken with the DALI2 array. Detailed analysis for the IVSMR is currently in progress.

References

- [1] Recent review on spin-isospin responses by the nucleon induced charge-exchange reaction for example: M. Ichimura, H. Sakai and T. Wakasa, Prog. Part. Nucl. Phys., **56**, 446 (2006).
- [2] I. Hamamoto and H. Sagawa, Phys. Rev. C **62**, 024319 (2000).
- [3] D. L. Prout et al., Phys. Rev. C **63**, 014603 (2000).
- [4] R. G. T. Zegers et al., Phys. Rev. Lett. **90**, 202501 (2003).
- [5] Y. Sasamoto et al., CNS Ann. Rep. 2010 (2012).
- [6] Y. Kikuchi et al., CNS Ann. Rep. 2010 (2012).
- [7] H. Miya et al., CNS Ann. Rep. 2010 (2012).
- [8] H. Tokieda et al., CNS Ann. Rep. 2009 (2010).

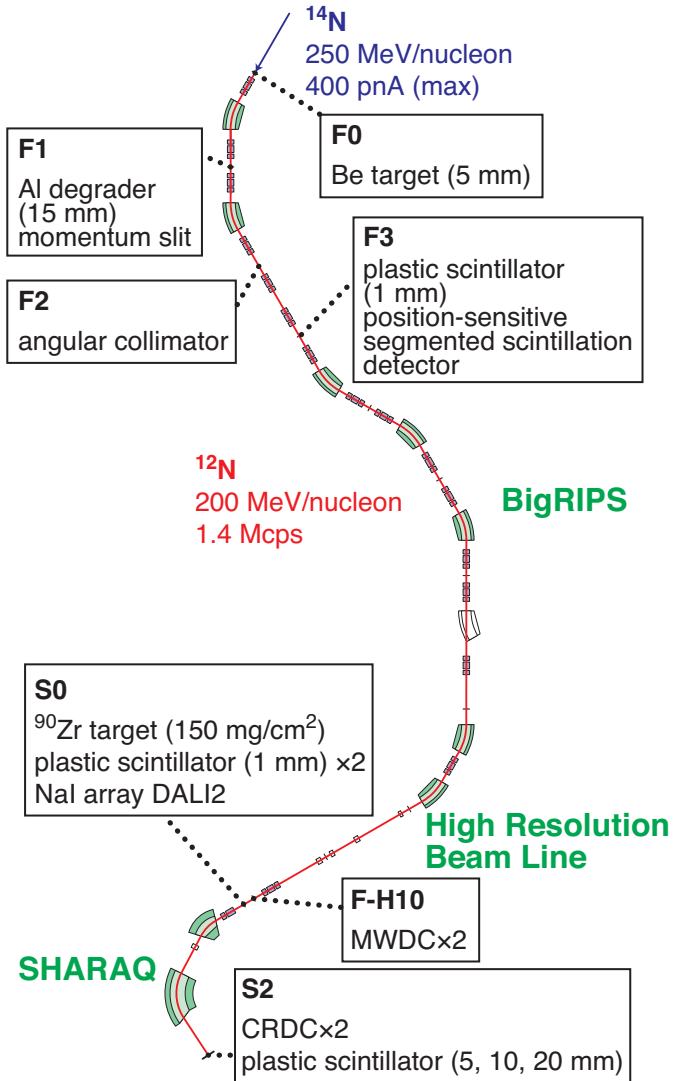


Figure 2. Setup of the present experiment performed at the RIBF by using the BigRIPS, the High Resolution Beam Line, and the SHARQA Spectrometer. Experimental devices installed are listed at the respective focal planes. See text for detail.

The super-allowed Fermi type charge exchange reaction for studies of isovector non-spin-flip monopole resonance

Y. Sasamoto, T. Uesaka, S. Shimoura, S. Michimasa, S. Ota, K. Miki^{a,b}, S. Noji^b, K. Yako^b, H. Tokieda, H. Miya, S. Kawase, Y. Kikuchi, K. Kisamori, M. Takaki, M. Dozono, H. Mathubara, H. Sakai^a, T. Kubo^a, Y. Yanagisawa^a, H. Takeda^a, K. Yoshida^a, T. Ohnishi^a, N. Fukuda^a, D. Kameda^a, N. Inabe^a, N. Aoi^a, S. Takeuchi^a, T. Ichihara^a, H. Baba^a, S. Sakaguchi^a, P. Doornenbal^a, H. Wang^a, R. Chen^a, Y. Shimizu^a, T. Kawahara^c, T. Kawabata^d, N. Yokota^d, Y. Maeda^e, H. Miyasako^e, G. P. A. Berg^f

Center for Nuclear Study, Graduate School of Science, University of Tokyo
^aRIKEN Nishina center

^bDepartment of Physics, University of Tokyo

^cDepartment of Physics, Toho University

^dDepartment of Physics, Kyoto University

^eDepartment of Physics, Miyazaki University

^fDepartment of Physics and Joint Institute for Nuclear Astrophysics, University of Notre Dame

1. Introduction

Isovector non-spin-flip monopole resonance (IVMR) is of particular interest, because it is an oscillation mode of isovector density $\rho_{IV} = \rho_n - \rho_p$ and its energy and width should be closely related to properties of asymmetric nuclear matter [1] and to isospin mixture in nuclei [2].

In spite of its importance, however, experimental data on IVMR are scarce so far. Pion charge exchange reactions (π^\pm, π^0) [3] and heavy-ion charge exchange (HICE) such as ($^{13}\text{C}, ^{13}\text{N}$) [4, 5] and ($^7\text{Li}, ^7\text{Be}$) [6] reactions have been used to study IVMR. These reactions provided inconsistent results of excitation energy, width, and/or multipolarity of the state [4].

To understand nature of IVMR, a HICE probe selective to the non-spin-flip ($\Delta T = 1, \Delta S = 0$) modes is essentially important. We propose the the super-allowed Fermi type charge exchange ($^{10}\text{C}, ^{10}\text{B}$ (IAS)) reaction which is selective to $\Delta T = 1, \Delta S = 0$ modes. This selectivity is achieved only with the RI beam induced reaction as will be explained below.

We applied ^{90}Zr to the ($^{10}\text{C}, ^{10}\text{B}$ (IAS)) reaction at ^{10}C beam energy of 200 MeV/nucleon. In this report, we introduce the characteristics of ($^{10}\text{C}, ^{10}\text{B}$ (IAS)) reaction and report the experimental result.

2. Characteristics of ($^{10}\text{C}, ^{10}\text{B}$ (IAS)) reaction

Our idea to probe the isovector non-spin-flip states is based on the use of a super-allowed Fermi transition between isobaric analog states in the projectile. This necessarily leads to an RI beam induced charge exchange reaction since light stable nuclei with $J^\pi = 0^+$ have no analog states because of their isospin $T = 0$. On the other hand, some unstable nuclei with $J^\pi = 0^+$ and $T = 1$ have isobaric analog states in neighbor nuclei. Gamma rays emitted from IAS can be used to identify the super-allowed Fermi transition experimentally. Among such RI beam induced charge exchange reactions, ($^{10}\text{C}, ^{10}\text{B}$ (IAS)) is considered to be the best one because the feedings from the highly ex-

cited GT states are expected to be negligibly small. This is not the case in other reactions such as ($^{14}\text{O}, ^{14}\text{N}$ (IAS)), ($^{18}\text{Ne}, ^{18}\text{F}$ (IAS)). This reaction has many advantages as a probe to IVMR as described in Ref. [7], over other HICE reactions used so far.

The analog state of the ^{10}C ground state locates at $E_x=1.74$ MeV in ^{10}B as shown in Fig. 1. The transition from the ^{10}C ground state to the 1.74-MeV state in ^{10}B can be experimentally identified by observing the emitted γ -ray of 1022 keV. Thus, coincident detection of ^{10}B and 1022-keV γ -rays in the final state will be a clear signature of $0^+ \rightarrow 0^+$ transition in the projectile, and consequently, of the non-spin-flip excitation in the target.

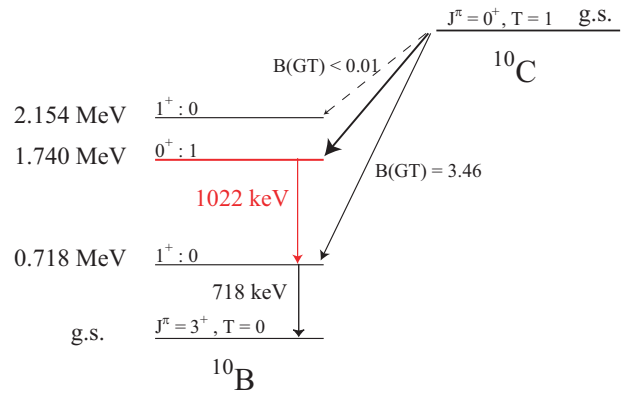


Figure 1. Levels in ^{10}B . The analog state of the ^{10}C ground state is found at $E_x=1.74$ MeV in ^{10}B .

3. Experiment and result

The experiment was performed at the RIBF facility in RIKEN using the SHARAQ spectrometer [8]. A layout of the experimental setup is shown in Fig. 2. The secondary ^{10}C beam was produced as fragments of 250 MeV/u ^{14}N using a ^9Be target with a thickness of 20 mm positioned at BigRIPS-F0 which is shown in Fig. 2 labeled of F0. A

purity of approximately 95% was achieved for ^{10}C by using an Al wedge with thickness of 810 mg/cm^2 . The intensity of the ^{10}C beam was approximately 2×10^6 pps at the secondary target. The beam trajectories were measured by the mitiwire drift chambers [9] upstream of the secondary target to determine the position and incident angle of the beam. High-resolution beamline was set to the dispersion-matched mode so as to cancel the effect of energy spread of the beam itself [10]. A secondary ^{90}Zr target with a thickness of 150 mg/cm^2 was used. The emitted 1022-keV γ -rays to define the non-spin-flip transition were detected by the NaI detector array (DALI2 [11]) located near the secondary target. Scattered ^{10}B particles were momentum analyzed by the SHARAQ spectrometer.

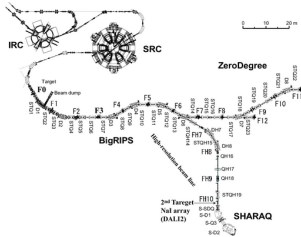


Figure 2. Layout of the experimental setup. It branches from BigRIPS after F6. F3 is the ion-optical starting point of the high-resolution beam line.

Figure 3 shows a Doppler-corrected γ -ray spectrum, obtained by DALI2 coincident with ^{10}B particles at the SHARAQ focal plane. The 1022-keV peak is clearly observed. Since this γ ray is emitted from the 0^+ state at $E_x=1.74\text{ MeV}$ in ^{10}B , the non-spin-flip transition can be deduced by gating on this peak.

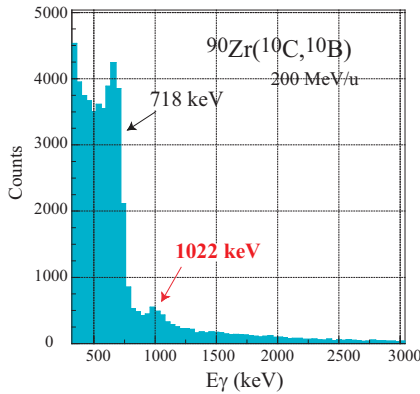


Figure 3. Doppler-corrected γ -ray spectrum of $^{90}\text{Zr}(^{10}\text{C}, ^{10}\text{B})$ obtained by DALI2.

Figure 4 shows a correlation between excitation energy and emitted γ rays of ^{90}Nb . The horizontal and vertical axes show gamma-ray energy detected in DALI2 and excitation energy in ^{90}Nb , respectively. At more than $E_x > 20\text{ MeV}$, some strengths coincident with 1022-keV gamma-ray in ^{90}Nb are observed. These strengths are possible candidates of IVMR in ^{90}Nb .

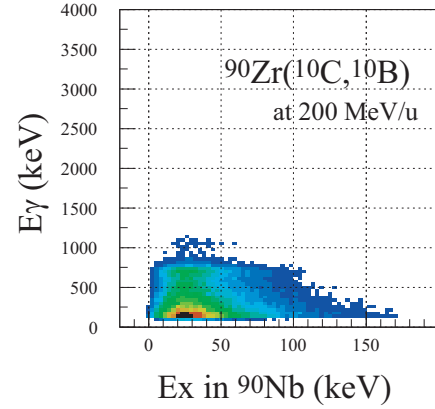


Figure 4. Correlation of Doppler-corrected γ -ray energy and excitation energy in ^{90}Nb .

4. Summary

In order to establish the HICE using the super-allowed Fermi type reaction that is selective to the non-spin-flip mode, the $^{90}\text{Zr}(^{10}\text{C}, ^{10}\text{B}(\text{IAS}))$ experiment at 200 MeV/u was performed using the SHARAQ spectrometer at RIBF. We successfully observed the 1022-keV gamma-rays emitted from $^{10}\text{B}(\text{IAS})$ which is a signature of the non-spin-flip transition. We also observed some strength around $E_x > 20\text{ MeV}$ in ^{90}Nb coincident with 1022-keV gamma-ray, where the IVMR is expected to exist. The extraction of the non-spin-flip amplitude based on the analysis of the γ -ray spectrum is now in progress.

References

- [1] G. Colo and N. Van Giai, Phys. Rev. C **53**, 2201 (1996).
- [2] A. Bohr and B. Mottelson, "Nuclear Structure".
- [3] A. Erell et al., Phys. Rev. C **34**, 1822 (1986).
- [4] I. Lhenry, Nucl. Phys. A **599**, 245c (1996).
- [5] T. Ichihara et al., Phys. Rev. Lett. **89**, 142501 (2002).
- [6] S. Nakayama et al., Phys. Rev. Lett. **83**, 690 (1999).
- [7] Y. Sasamoto et. al., CNS Ann. Rep. 2009, 27 (2010).
- [8] T. Uesaka et al.: Nucl. Instrum. Meth. in Phys. Res. B **266**, 4218 (2008).
- [9] H. Miya et al., CNS Ann. Rep. 2010 (2012).
- [10] T. Kawabata et al.: Nucl. Instrum. and Meth. in Phys. Res. B **266**, 4201 (2008).
- [11] S. Takeuchi et. al.: RIKEN Accel. Prog. Rep. **36**, 148 (2003).

Proton spin-orbit splitting in ^{18}O studied by the $(\vec{p}, 2p)$ reaction at 200 MeV

S. Kawase, T. Uesaka, S. Ota, H. Tokieda, Y. Kikuchi, K. Kisamori, M. Takaki, H. Matsubara, M. Dozono, T. Kawahara^a, T. Kawabata^b, Y. Nozawa^b, N. Yokota^b, T. Noro^c, T. Wakasa^c, M. Okamoto^c, Y. Maeda^d, T. Saito^d, H. Miyasako^d, A. Tamii^e, and T. Suzuki^e

Center for Nuclear Study, Graduate School of Science, University of Tokyo

^aDepartment of Physics, Faculty of Science, Toho University

^bDepartment of Physics, Kyoto University

^cDepartment of Physics, Kyushu University

^dDepartment of Applied Physics, Faculty of Engineering, University of Miyazaki

^eResearch Center for Nuclear Physics, Osaka University

Strong spin-orbit coupling, which was introduced independently by Mayer and Jensen to explain magic numbers in nuclei, is essential in nuclear physics. It is so strong that it can shuffle the level sequences with different principal quantum numbers, or in different major shells. The spin-orbit splitting is a direct measure of the strength of the spin-orbit coupling. We have been studying the proton 1p spin-orbit splitting in ^{18}O nuclei via the $(\vec{p}, 2p)$ reaction. This is the first step to the systematic study of the spin-orbit splitting in the chain of oxygen isotopes, where it is aimed to reveal how the spin-orbit splitting changes as a function of neutron number in nuclei far from the β -stability line.

The experiment was carried out at the Ring Cyclotron Facilities of the Research Center for Nuclear Physics (RCNP), Osaka University. A spin-polarized proton beam with the kinetic energy of 200 MeV was injected into a thin (~ 20 mg/cm²) and windowless H_2^{18}O ice target [1]. To evaluate the ^{16}O contamination in the target, an H_2^{16}O ice target was also used. To shorten the traversing length of the outgoing protons with lower energy, which were scattered to the direction to the LAS, the ice target was tilted to the Large Acceptance Spectrometer (LAS) by 30 degrees from the beam direction as shown in Fig. 2. Spin polarization of the proton beam was monitored continuously by a pair of beam line polarimeters and it was approximately 60% over the experiment. Momentum vectors of two scattered protons were determined by using the two-arm spectrometer system, which is shown in Fig. 1, consisting of the Grand Raiden Spectrometer [2] and the Large Acceptance Spectrometer [3]. The design specifications of GR and LAS are summarized in Table 1. The angles of the spectrometers were set to maximize the efficiency of spin-parity (J^π) identification. Proton separation energy and excitation energy in residual ^{17}N was deduced from the momenta of the protons and their resolution is 350 keV (FWHM), obtained as the recoil momentum of the residual ^{17}N . Typical spectra of differential cross section and vector analyzing power A_y are shown in the upper and the middle panel of Fig. 3, respectively. The peak at the separation energy of 16 MeV corresponds to the ground state of ^{17}N . In addition to some known states in ^{17}N , an excited state of ^{17}N at 11.13 MeV (correspond to the Separation energy of 27.13 MeV) was observed for the first time in this experiment.

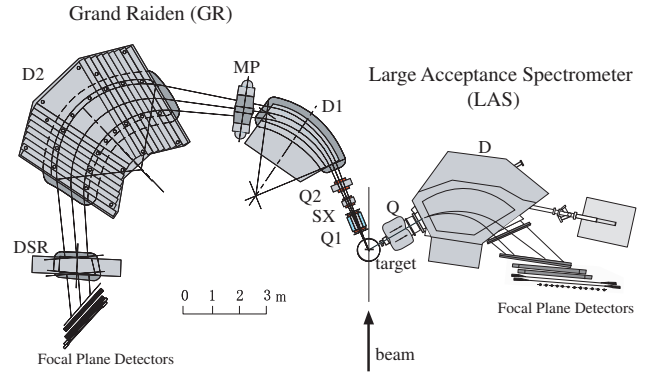


Figure 1. Schematic view of the two-arm spectrometer system at the RCNP

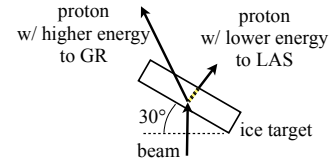


Figure 2. The target was tilted to shorten the traversing length of the protons with lower energy

We compared the experimental results with the calculation based on the distorted wave impulse approximation (DWIA) by using the computer code THREEDEE [4]. In this calculation, Dirac optical model potentials given by Cooper *et al.* [5] and the NN scattering amplitude given by Arndt *et al.* [6] were used. The calculation reproduced well the Fermi momentum dependence of the differential cross section and analyzing power for known states. Differential cross section and analyzing power for the 11.13 MeV state is shown in Figs. 4 and 5. From this comparison, we determined the J^π of a state at 10.14 MeV and at 11.13 MeV to be $3/2^-$. The 1p proton spin-orbit splitting was determined as the difference between the single-particle energies of $1p_{3/2}$ and $1p_{1/2}$ states. Since the single-particle $1p_{3/2}$ state fragment into several $3/2^-$ states, the $1p_{3/2}$ single-particle energy was obtained by taking the S-factor-weighted-mean of the excitation energies of the fragmented states with $J^\pi = 3/2^-$. Here, S-factor was defined as $S \equiv \left(\frac{d^2\sigma}{d\Omega dE} \right)_{\text{exp.}} / \left(\frac{d^2\sigma}{d\Omega dE} \right)_{\text{DWIA}}$ and its assignment for several single-particle states is shown in the lower panel of Fig. 3. As a result, the proton 1p spin-orbit splitting in ^{18}O

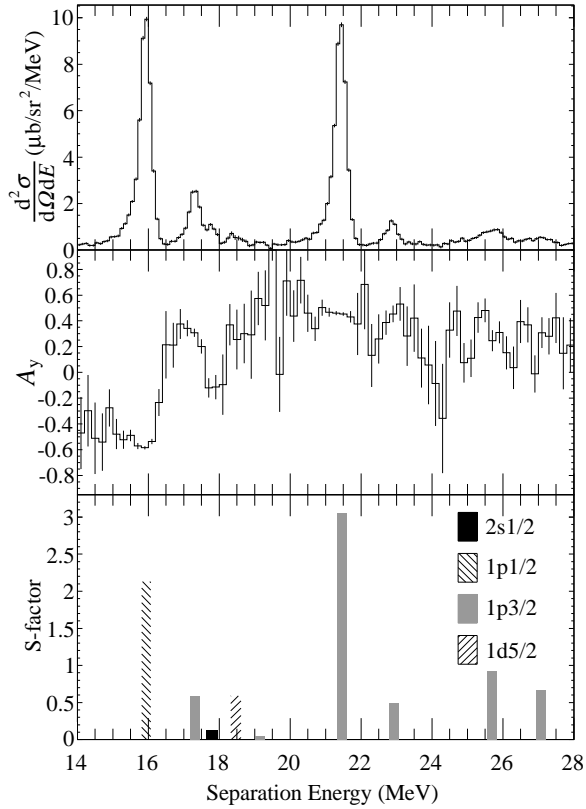


Figure 3. Typical spectra of differential cross section $\frac{d^2\sigma}{d\Omega dE}$ (upper panel), vector analyzing power A_y (middle panel), and S-factor assignments for several single particle states (lower panel). The abscissa shows the proton separation energy.

was obtained as 6.51 MeV. This value is lower than that of ^{16}O , which is approximately 7 MeV. Further analysis including detailed evaluation of background and error is in progress.

References

- [1] T. Kawabata *et al.*, Nucl. Instrum. Meth. A **459** (2001) 171.
- [2] M. Fujiwara *et al.*, Nucl. Instrum. Meth. A **422** (1999) 484.
- [3] N. Matsuoka *et al.*, RCNP Annual Report 1990, page 235.
- [4] N. S. Chant and P. G. Roos, Phys. Rev. C **15** (1977) 57.
- [5] E. D. Cooper, S. Hama, B. C. Clark, and R. L. Mercer., Phys. Rev. C **47** (1993) 297.
- [6] R. A. Arndt, J. S. Hyslop, and L. D. Roper, Phys. Rev. D **35** (1987) 128.

Table 1. Design specification of the two-arm spectrometer system at the RCNP facility

	GR	LAS
Configuration	QSQDMD(+D)	QD
Radius of the central orbit	3 m	1.75 m
Total bending angle	162°	70°
Tilting angle of focal plane	45°	57°
Maximum magnet rigidity	5.4 Tm	3.2 Tm
Hor. magnification (x x)	-0.417	-0.4
Ver. magnification (y y)	5.98	-7.3
Momentum range	5%	30%
Momentum resolution	37,076	4,980
Acceptance of hor. angle	±20 mr	±60 mr
Acceptance of ver. angle	±70 mr	±100 mr

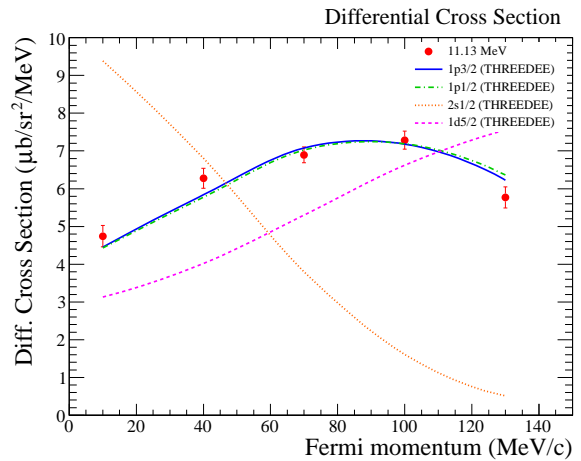


Figure 4. Differential cross section for the 11.13 MeV state. The abscissa shows the proton Fermi momentum in ^{18}O . Differential cross sections for 2s and 1d states are arbitrary scaled.

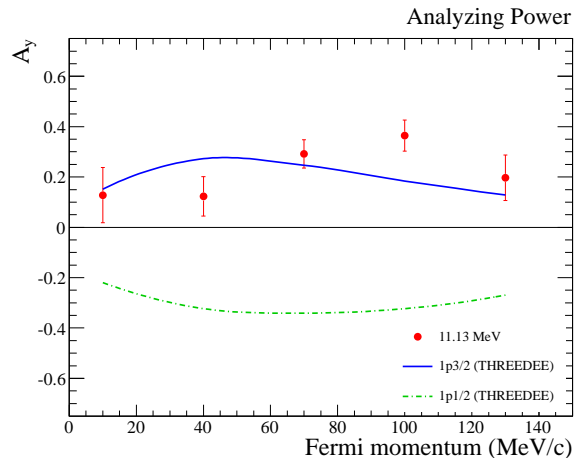


Figure 5. Analyzing power for the 11.13 MeV state. The abscissa shows the proton Fermi momentum in ^{18}O .

Development of heavy-ion detection at GRAND RAIDEN spectrometer for the (^{18}O , ^{18}Ne) reaction

M. Takaki, H. Matsubara, T. Uesaka^a, S. Shimoura, N. Aoi^b, M. Dozono^a, T. Fujii, K. Hatanaka^b, T. Hashimoto^b, T. Kawabata^c, S. Kawase, K. Kisamori, Y. Kikuchi, Y. Kubota, C.S. Lee, H.C. Lee^a, Y. Maeda^d, S. Michimasa, K. Miki^b, H. Miya, S. Noji, S. Ota, S. Sakaguchi^e, Y. Sasamoto, T. Suzuki^b, L.T. Tang, K. Takahisa^b, H. Tokieda, A. Tamii^b, K. Yako^f, Y. Yasuda^b, N. Yokota^c, R. Yokoyama, and J. Zenihiro^a

Center for Nuclear Study, Graduate School of Science, University of Tokyo

^a*RIKEN (The Institute of Physical and Chemical Research)*

^b*Research Center for Nuclear Physics, Osaka University*

^c*Department of Physics, Kyoto University*

^d*Department of Applied Physics, Miyazaki University*

^e*Department of Physics, Kyushu University*

^f*Department of Physics, University of Tokyo*

Heavy-ion double charge exchange reactions (HIDCX) [1, 2] provide a unique spectroscopic tool through which we can transfer isospin quantum numbers by an amount of two to the target nucleus. We apply the HIDCX for spectroscopies of light neutron rich nuclei. Even if we use stable nuclei as a target, we can study the light neutron rich nuclei near the drip line. Also this reaction enables missing mass measurements.

For the first step to establish the HIDCX reaction as a spectroscopic tool, we employ a (^{18}O , ^{18}Ne) reaction for the spectroscopy of the ^{12}Be nucleus. The ground states of ^{18}O and ^{18}Ne nucleus are among the same super-multiplet and the transition between them is just double spin-isospin or isospin flips keeping spatial wave function unchanged. Hence, the transition can be simple and the amplitude can be large. The neutron rich ^{12}Be nucleus is one of the most symbolic nucleus evidencing disappearance of $N = 8$ magicity [3]. In recent years, the ^{12}Be has been studied extensively [4–8]. Its single particle nature of ground and low-lying states are well understood.

We have proposed to measure cross section of the $^{12}\text{C}(^{18}\text{O}, ^{18}\text{Ne})^{12}\text{Be}$ reaction at 80 MeV/u with the high-resolution GRAND RAIDEN (GR) spectrometer at Ring Cyclotron Facility, Research Center for Nuclear Physics (RCNP), Osaka University. This was the first experiment for the GR spectrometer to measure heavy-ion particles whose Z are larger than 4. Therefore, we performed feasibility experiment to ensure that the GR spectrometer has sufficiently resolution of momentum, timing and scattering angle to identify the ^{18}Ne nuclei. In the experiment, the ^{18}O beam was accelerated up to 80 MeV/u by two cyclotrons and bombarded a natural carbon target with an areal density of 2.15(10) mg/cm². Outgoing particles were momentum-analyzed through the GR spectrometer, then detected by two vertical drift chambers (VDCs) optimized for the heavy-ion beam and two plastic scintillators. The detail of experimental setup is found in Ref. [9].

An ion optics of the GR spectrometer should be known to reconstruct scattering angle at the target position from

ray information measured by the focal plane detectors. The scattering angle was calibrated by using sieve-slit data. The sieve-slit has a hole of 3 mm in diameter at the center and the other holes of 2 mm. The GR spectrometer was set to 3°, and the sieve-slit was placed at the entrance of the GR spectrometer. Elastic scattering of $^{18}\text{O} + ^{197}\text{Au}$ data were measured with the sieve-slit. The magnetic field of the GR spectrometer was changed from -1.4 % to +1.4 % in a step of 0.7 % with respect to the standard setting in order to search horizontal detection position (x_d) dependence in reconstructing scattering angle. Horizontal scattering angle (A_I) and vertical scattering angle (B_I) at the target position were calibrated by the equations

$$\begin{aligned} A_I &= \sum_{i=0}^2 \sum_{j=0}^2 \sum_{k=0}^2 a_{ijk} x_d^i \theta_d^j y_d^k, \\ B_I &= \sum_{i=0}^2 \sum_{j=0}^2 \sum_{k=0}^2 \sum_{l=0}^1 b_{ijkl} x_d^i \theta_d^j y_d^k \phi_d^l, \end{aligned} \quad (1)$$

where y_d and ϕ_d are the vertical position and vertical incident angle at the focal plane detectors, respectively. The parameters a_{ijk} and b_{ijkl} were determined by a multi-dimensional least-squares fitting of the sieve-slit data. The scattering angle at the target (Θ_{tgt}) was defined by A_I , B_I and the spectrometer angle θ_s as

$$\Theta_{tgt} = \sqrt{(A_I + \theta_s)^2 + B_I^2}. \quad (2)$$

Figure 1 shows a result of the scattering angle reconstruction. The total scattering angle resolution of 5 mr (FWHM) was achieved. The angular acceptance of the GR spectrometer was ± 20 mr in the horizontal direction and ± 45 mr in the vertical direction.

For the analysis, a reliable particle identification method was indispensable to avoid possible contamination by lighter isotopes. Thus we used A/Q value and energy loss in the plastic scintillators. Since ^9B is unbound, ^{18}Ne is a unique isotope with $A/Q = 1.8$, which enables us to make a safe and reliable particle identification of ^{18}Ne . An A/Q

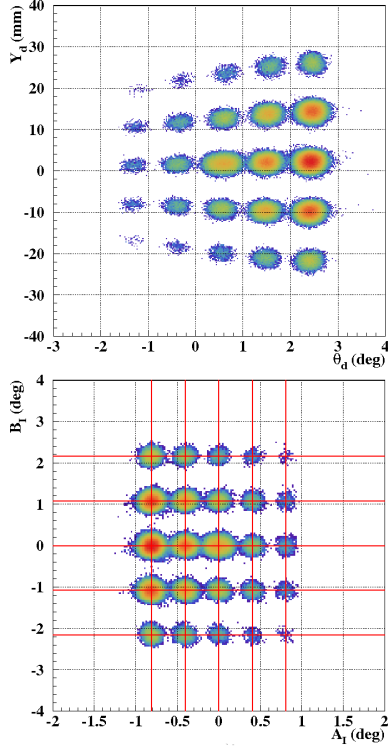


Figure 1. Reconstruction of the horizontal (A_I) and vertical (B_I) scattering angle at the target from the information at the detector position (upper panel). The cross points of the red lines (lower panel) correspond to the hole positions of the sieve-slit.

value can be calculated as a function of magnetic rigidity $B\rho$ and particle velocity β by the function

$$A/Q = \frac{B\rho}{\beta\gamma m_N}, \quad \gamma = \frac{1}{\sqrt{1-\beta^2}}, \quad (3)$$

where m_N is nucleon mass. It is noted that the A/Q value of each isotope should have no dependence on $B\rho$ and β . Since differences of flight length through the spectrometer deteriorate an accuracy of β , the flight length was corrected event by event with $B\rho$ and A_I information. Then, we have achieved satisfactory precision for particle identification. Figure 2 shows a result of particle identification. Figure 3 shows a typical A/Q value distribution with a gate of energy loss in the plastic scintillator. The ^{18}Ne is completely separated from other isotopes.

In summary, we succeeded in clear particle identification of ^{18}Ne with the GR spectrometer and the default detectors setup for it. It was the first case for the GR spectrometer to be used for measurement of heavy-ions with $Z=10$. Our result demonstrates that we can perform HIDCX (^{18}O , ^{18}Ne) reactions measurement with the GR spectrometer. Although the reaction process in a HIDCX transition is unclear so far, we expect that this study can be a valid benchmark to develop the HIDCX reaction model.

References

[1] L.K. Fifield *et al.*, Nucl. Phys. A **385** (1982) 505.

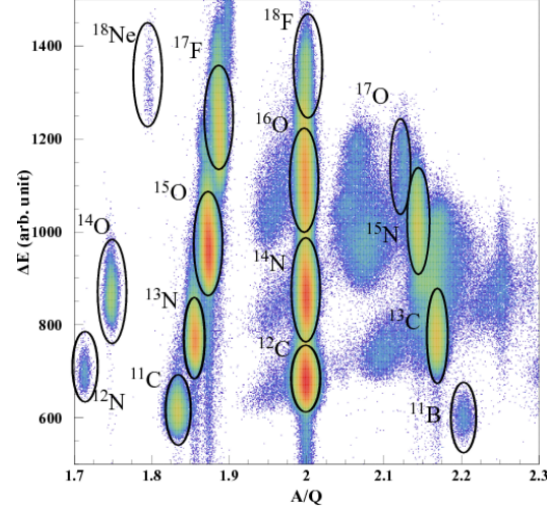


Figure 2. Result of the particle identification. The horizontal axis denotes the A/Q , while the vertical axis expresses the energy loss in the plastic scintillator.

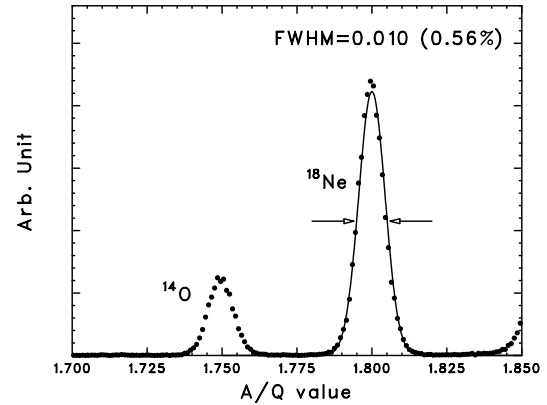


Figure 3. Typical distribution of A/Q value. It clearly shows that the peak at $A/Q = 1.8$, representing ^{18}Ne , is well isolated from other isotopes, the resolution of which is 0.010 (FWHM).

- [2] J. Blomgren *et al.*, Phys. Lett. B **362** (1995) 34.
- [3] A. Navin *et al.*, Phys. Rev. Lett. **85** (2000) 266.
- [4] H. Iwasaki *et al.*, Phys. Lett. B **481** (2000) 7; *ibid.* **491** (2000) 8.
- [5] S. Shimoura *et al.*, Phys. Lett. B **560** (2003) 31; *ibid.* **654** (2007) 87.
- [6] S. D. Pain *et al.*, Phys. Rev. Lett. **96** (2006) 032502.
- [7] N. Imai *et al.*, Phys. Lett. B **673** (2009) 179.
- [8] R. Kanungo *et al.*, Phys. Lett. B **682** (2010) 391.
- [9] H. Matsubara *et al.*, CNS Ann. Rep. 2010 (2012).

**Experimental Nuclear Physics:
PHENIX Experiment at BNL-RHIC and
ALICE Experiment at CERN-LHC**

First Results of Pb+Pb Collisions at $\sqrt{s_{NN}}=2.76$ TeV from LHC-ALICE

T. Gunji, H. Hamagaki, S. Sano Y. Hori, for the ALICE Collaboration

Center for Nuclear Study, Graduate School of Science, University of Tokyo

1. Introduction

The ultra-high energy heavy ion collisions are unique tool in the laboratory to realize the strongly interacting QCD matter composed of quarks and gluons. 10 years heavy ion experimental programs at the Relativistic Heavy Ion Collider in BNL reveals the formation of the hot and dense QCD medium, where the medium are found to be strongly coupled with viscosity to entropy ratio (η/s) of nearly conjectured limit.

The Large Hadron Collider (LHC) at CERN starts its operation since 2009 and first Pb+Pb collisions with the center of mass energy per nucleon ($\sqrt{s_{NN}}$) of 2.76 TeV was conducted in Nov. in 2010. Since the collision energy is 14 times larger than that at RHIC, heavy ion collisions at LHC gives detail and quantitative understanding the properties of strongly interacting QCD matter.

ALICE (A Large Ion Collider Experiment) is one of the experiments performed at LHC and is dedicated for the heavy ion collisions. The ALICE experiment consists of a larger number of detectors [1]. Central barrel detectors measuring hadrons, electrons and photons at pseudo-rapidity of $|\eta| \leq 0.9$ are composed of an Inner Tracking System (ITS) of high-resolution silicon detectors, a cylindrical Time-Projection Chambers (TPC), a Transition Radiation Detectors and a Time-Of-Flight (TOF) detector. A single arm detectors of lead-scintillation ElectroMagnetic Calorimeter (EMCal), a lead-tungsten crystal calorimeter (PHOS), and a ring imaging Cherenkov hodoscope (HMPID) complement the central barrel of ALICE. The forward muon arm consists of a complex of absorbers, a dipole magnet, and tracking and triggering muon chambers. Several smaller detectors (T0, V0, ZDC, FMD, PMD) are also installed at forward rapidity in ALICE for the global event characterization and trigger.

CNS has an activity for the commissioning of the TRD, especially taking a leading role for the development of the slow control system, the calibration and performance evaluation of TPC, and a leading efforts for the R&D of the Forward Calorimeter as one of the ALICE upgrade plans [2–6].

2. First Pb+Pb collisions at LHC-ALICE

The first heavy ion run at $\sqrt{s_{NN}} = 2.76$ TeV took place in November 8th 2010, a couple of days after the LHC switched over the operation from $p + p$ at $\sqrt{s} = 7$ TeV. The heavy ion runs went exceedingly well and the luminosity increased steeply and reached about $2 \times 10^{25} \text{ cm}^{-2} \text{ s}^{-1}$ by the end of the run. The ALICE collected 30 M nuclear MB interactions, where the data was taken with so called MB trigger, defined as two hits out of at SPD, V0A (V0 detector at positive rapidity) and V0C (V0 detector at negative rapidity).

3. First Results of Pb+Pb Collisions

3.1. Particle Multiplicity

The first and most anticipated result from the ALICE is on the measurement of the charged particle multiplicity density in Pb+Pb collisions [7]. The measured value in central collisions is $dN_{ch}/d\eta \sim 1600$, which was somewhat on the high side of more recent (post- RHIC) predictions. From the measured multiplicity in central collisions, the energy density is estimated and found to be at least a factor 3 above RHIC, which indicates that the corresponding increase of the initial temperature is about 30%, even with the assumption that the formation time τ_0 is same from RHIC to LHC. Figure 1 shows the centrality dependence of the charged particle multiplicity measured by the ALICE (Pb+Pb Collisions shown as closed) and the RHIC (Au+Au collisions with $\sqrt{s_{NN}} = 200$ GeV as open symbols) with a scale that differs by a factor of 2.1 on the right-hand side.

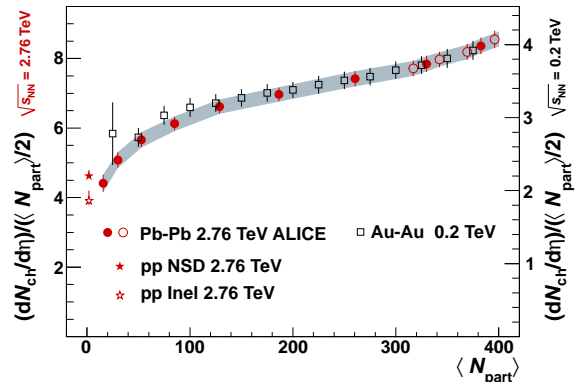


Figure 1. Centrality dependence of charged particle multiplicity measured by LHC-ALICE (closed) and RHIC-average(open).

As is seen in Fig. 1, the centrality dependence of the charged particle multiplicity measured in Pb+Pb collisions is similar to Au+Au collisions at RHIC, even though the impact parameter dependent gluon shadowing/saturation could be expected to be much stronger at LHC (much smaller Feynman-x).

3.2. Elliptic Flow

One of the exciting results observed at RHIC is that there is a large azimuthal anisotropy with respect to the reaction plane, between two colliding nuclei in non-central Au+Au collisions. The magnitude of the anisotropy, its transverse momentum and particle species dependence can be well-described by the ideal hydrodynamics. The systematic measurement of the azimuthal anisotropy has been done in ALICE, where its particle species dependence, transverse momentum dependence, fine centrality dependence, and higher order flow components have been investigated with various

analysis methods to understand, reduce and/or subtract non-flow contributions.

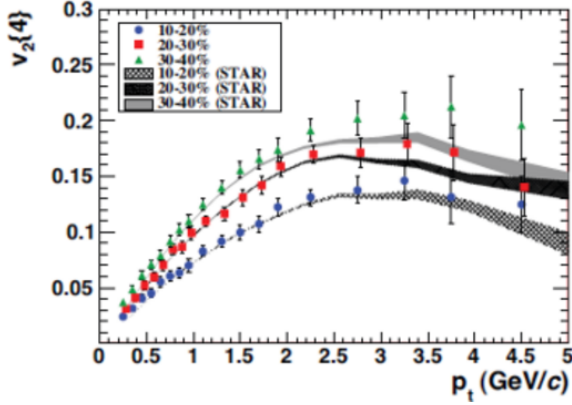


Figure 2. Elliptic flow parameter v_2 as a function of the transverse momentum for the centrality of 10-20/20-30/30-40% at LHC (symbol). For the comparison, results from RHIC are also shown as hatched shapes..

Figure 2 shows v_2 as a function of the transverse momentum obtained with the 4- particle cumulant method for three different centralities, compared to STAR measurements, where the 4-particle cumulant method suppresses auto-correlation between two particles originating from, for instance, hard processes [8]. The transverse momentum dependence is qualitatively similar for all three centrality classes. At low p_T , there is a good agreement of v_2 between ALICE and STAR data. The observed similarity at RHIC and the LHC of p_T differential elliptic flow at low p_T is consistent with predictions of hydrodynamic models with the small viscous corrections ($\eta/s \leq 0.16$).

3.3. Suppression of high p_T particle production

Suppression of high p_T particle production has been observed at RHIC, revealing that the hard scattered partons lose their energy inside the hot and dense QCD medium. The magnitude of the suppression and its momentum dependence clearly relate to the properties of the medium such as initial gluon density, its space-time evolution, equation of state and so on. In Fig. 3, the ALICE result of the nuclear modification factor R_{AA} in central Pb+Pb collisions is compared to measurements of that of charged hadrons by the PHENIX and STAR experiments at RHIC [9]. At 1 GeV/c the measured value of R_{AA} is similar to those from RHIC. The position and shape of the maximum at p_T of 2 GeV/c and the subsequent decrease are similar at RHIC and LHC. When comparing the spectra between RHIC and LHC, the spectra at LHC energy is known to be much flatter for higher p_T due to the increase of hard process at LHC energy, which leads the gradual increase of R_{AA} . However, despite the much flatter p_T spectrum in $p + p$ at the LHC, R_{AA} at $p_T = 6 - 7$ GeV/c is smaller than at RHIC. This suggests that the energy loss at LHC is large and therefore a denser medium is formed at the LHC.

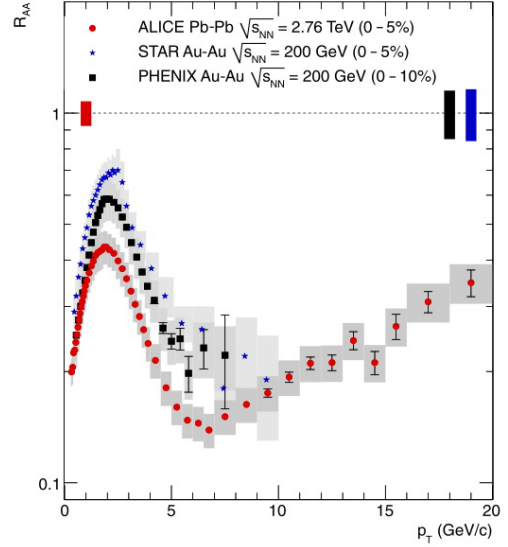


Figure 3. Nuclear modification factor R_{AA} of charged hadrons as a function of p_T measured in Pb+Pb collisions at ALICE (circle),

4. Summary and Outlook

Experimental studies of hot and dense QCD medium in heavy ion collisions have entered the new era in conjunction with the start of the operation of Pb+Pb collisions at LHC. First year Pb+Pb collisions in ALICE was great successful and a wealth of various results reveals a smooth evolution of the medium from RHIC to LHC. Although the results are qualitatively similar, it is mature to have a firm conclusion about the similarity since the initial conditions (e.g. the energy density) are sufficiently different at both energies. Further systematic measurements and many other observables which have different sensitivity to the medium properties are on going.

References

- [1] ALICE Collaboration, Physics Performance Report Vol. 1 J. Phys. **G 30** (2003) 1517.
- [2] T. Gunji *et al.* CNS Annual Report 2007.
- [3] T. Gunji *et al.* CNS Annual Report 2008.
- [4] S. Sano *et al.* CNS Ann. Rep. 2009 (2011).
- [5] Y. Hori *et al.* CNS Ann. Rep. 2010 (2012)x.
- [6] T. Gunji *et al.* CNS Ann. Rep. 2008 (2010), Y. Hori *et al.* CNS Ann. Rep. 2009 (2011), T. Tsuji *et al.* CNS Ann. Rep. 2010 (2012)x, S. Hayashi *et al.*, CNS Ann. Rep. 2010 (2012)x,
- [7] K. Aamodt *et al.*, for the ALICE Collaboration, Phys. Rev. Lett. **105**, 252301, 2010
- [8] K. Aamodt *et al.*, for the ALICE Collaboration, Phys. Rev. Lett. **105**, 252302, 2010
- [9] K. Aamodt *et al.*, for the ALICE Collaboration, Phys. Lett. **B696**, 30-39, 2011

Measurement of multi-strange particles in $\sqrt{s} = 7$ TeV $p + p$ collisions at LHC-ALICE

S. Sano, H. Hamagaki, T. Gunji, for the ALICE collaboration

Center for Nuclear Study, Graduate School of Science, University of Tokyo

1. Introduction

In the Quark Gluon Plasma (QGP) phase, it is predicted that the mass of strange quark is decreased from ~ 500 MeV to ~ 150 MeV and produced rapidly resulting a strangeness-rich matter. This strangeness enhancement is confirmed with the experiments of heavy-ion collisions [1]. Especially, multi-strange hadrons are good probes to search QGP, because they are produced rarely in non-QGP state. Particle ratios including multi-strange particles (Ξ and Ω) have been measured at RHIC and the yields are found to be well described by the statistical models with fully chemical equilibration of strangeness [2, 3].

At the LHC energy, there is possibility of the “heavy-ion-like” collective effects in $p + p$ collisions. According to the LHC-CMS experiment, a long-range ridge-like structure were observed in long-range azimuthal correlation studied for the high multiplicity events of $\sqrt{s}=7$ TeV $p + p$ collisions [4], where this structure was observed in only heavy-ion collisions but not $p + p$ collisions at the RHIC energy.

The aim of this study is to evaluate multiplicity dependence of strange particle production and the QGP search in $p + p$ collisions at LHC energy. In 2010, $\sqrt{s} = 7$ TeV $p + p$ collisions with about 1G events were produced, and about 200M events including low probability of multi-collision in one bunch crossing were analyzed. In this report, the current status of analysis for multiplicity dependence of Ξ and Ω productions in $\sqrt{s} = 7$ TeV $p + p$ collisions is described.

2. Analysis

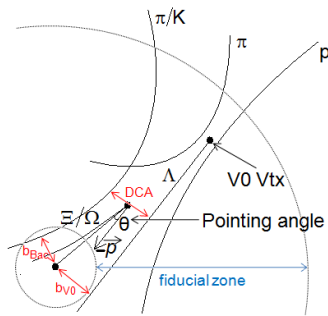


Figure 1. Geometrical selections for cascade reconstruction.

Yields of Ξ and Ω can be measured by detecting decay products of the decay channel ($\Xi/\Omega \rightarrow \Lambda + \pi/K \rightarrow p + \pi + \pi/K$). Strange particles decay by a weak interaction, and their flight lengths $c\tau$ are several centimeters, e.g. $c\tau=7$ cm, 2.5 cm, 5 cm for Λ , Ξ , and Ω , respectively. In ALICE, tracks of charged particles are mainly measured with the Inner Tracking System (ITS) and the Time Projection Chamber (TPC). At the tracking with TPC and ITS, the vertices for $\Lambda \rightarrow p + \pi$ and $\Xi/\Omega \rightarrow \Lambda + \pi/K$ are recon-

structed as “V0” and “Cascade” vertices, respectively. The fiducial zone to reconstruct these vertices is from a few cm to 250 cm in the direction normal to the beam axis. Topological information such as a distance to closest approach (DCA) between tracks or the pointing angle of the flight direction against the primary vertex are useful to select the appropriate track combinations (See Fig. 1). Figure 2 shows the distribution of DCA b_{V0} between the estimated track of Λ and the primary vertex (left panel), and the pointing angle θ for Ξ (right panel) in the experimental results compared to the simulated ones. Green (decay production of true Ξ in simulation) and blue (signal in experimental data) symbols are agreed well.

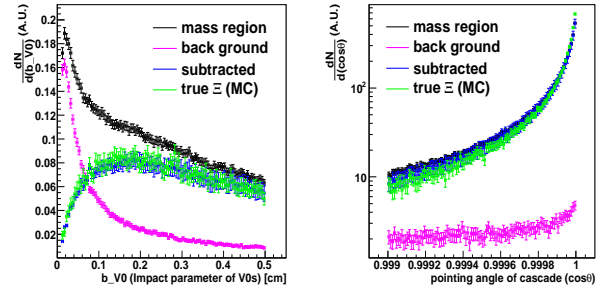


Figure 2. Distributions of DCA b_{V0} between the track of Λ and the primary vertex (left panel) and the pointing angle θ for Ξ (right panel).

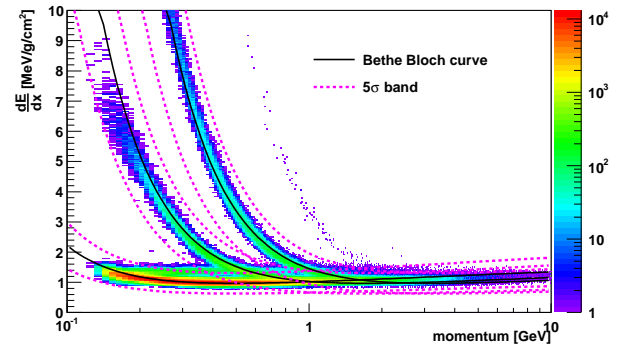


Figure 3. TPC dE/dx vs. momentum measured with ALICE-TPC.

Particle identification (PID) of π , K , and p can be made according to dE/dx measured by TPC. Figure 3 shows dE/dx against momenta of charged particles measured by TPC. Solid lines are the Bethe Bloch curves tuned to be matched with measured dE/dx bands, and dotted lines are 5σ bands i.e. $dE/dx_{exp}(1 \pm 5\sigma)$, where σ is set to 0.07.

The detection efficiencies for Ξ and Ω are calculated using the simulation data of PYTHIA. Figure 4 shows the ob-

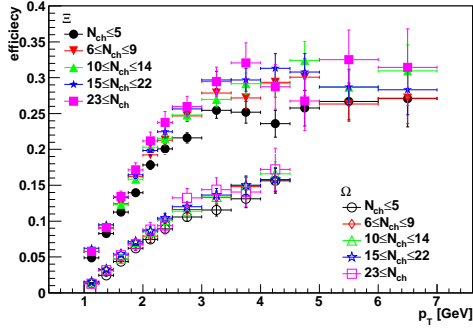


Figure 4. Detection efficiencies of the decay channel $\Xi/\Omega \rightarrow \Lambda + \pi/K \rightarrow p + \pi + \pi/K$ for each multiplicity bin. They include the effect of the tracking efficiency of decay productions, quality cuts, topological cuts, decay branching ratio, and the reconstruction efficiency of primary vertex.

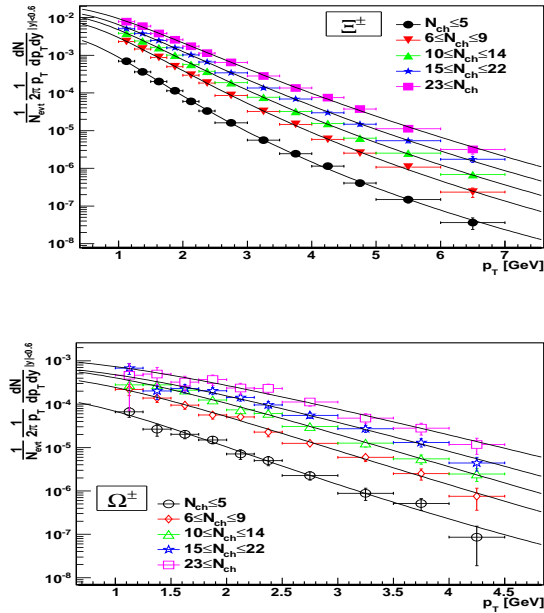


Figure 5. p_T spectra of Ξ (upper panel) and Ω (lower panel) for each multiplicity bin.

tained detection efficiencies including the effect of tracking efficiency of decay products, quality cuts, topological cuts, decay branching ratio, and the reconstruction efficiency of primary vertex as a function of transverse momentum p_T at mid-rapidity ($|y| < 0.6$) for each multiplicity bin. N_{ch} is the number of charged tracks assigned as the primary particles [6]. The reconstruction of primary vertex requires at least 3 tracks, so the efficiency decreases in low multiplicity.

3. Results

Figure 5 shows the corrected invariant yields of Ξ and Ω at mid-rapidity ($|y| < 0.6$) for each multiplicity bin. Bars on symbols show statistical errors. They are fitted with the Levy function, Eq. (1), in order to determine the global in-

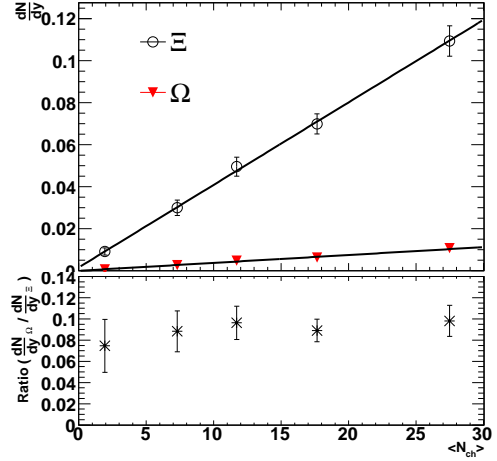


Figure 6. Multiplicity dependence of the yields of Ξ and Ω .

tegrated yields:

$$\frac{1}{2\pi p_T} \frac{d^2N}{dy dp_T} = \frac{dN}{dy} \frac{(n-1)(n-2)}{2\pi n T [nT + m(n-2)]} \times \left(1 + \frac{\sqrt{p_T^2 + m^2 - m}}{nT}\right)^{-n}. \quad (1)$$

Levy function which refers to as the Tsallis function [5] can well describe the spectra in a wide p_T range. Figure 6 shows dN/dy determined from Levy fits, and ratios between Ξ and Ω as a function of the mean number of charged particles $\langle N_{ch} \rangle$ corresponding to each multiplicity bin. The ratio slightly increases as multiplicity increases and then reaches a plateau.

4. Summary and outlook

Measurement of multi-strange particles (Ξ and Ω) has been made in $\sqrt{s}=7$ TeV $p+p$ collisions, and p_T spectra of invariant yields are obtained for each multiplicity bin. The ratio of the integrated yields dN/dy slightly increases as $\langle N_{ch} \rangle$ increases. Comparison with non-strange or single-strange particles ($\pi, K, p, K_s^0, \Lambda$) will be executed and further information on the strangeness production in $p+p$ collisions at $\sqrt{s}=7$ TeV will be obtained.

References

- [1] A.R. Timmins et al, the STAR Collaboration, J. Phys. G **36**, 064006 (2009).
- [2] B.I. Abelev et al, STAR Collaboration, Phys. Rev. C **77**, 044908 (2008).
- [3] M. Kaneta and N. Xu, arXiv:nucl-th/0405068 (2004).
- [4] The CMS collaboration, J. High Energy Phys. **09**, (2010) 091.
- [5] C. Tsallis, J. Statist. Phys. **52**, 479 (1988).
- [6] S. Sano. CNS Ann. Rep. 2009 (2011).

Study of nuclear effects on low p_T direct photon production in $\sqrt{s_{NN}} = 200$ GeV $d+Au$ collisions at RHIC

Y.L. Yamaguchi, H. Hamagaki, Y. Akiba^a, and T. Gunji, for the PHENIX collaboration

Center for Nuclear Study, Graduate School of Science, University of Tokyo

^a RIKEN (The Institute of Physical and Chemical Research)

1. Introduction

Direct photons in the low p_T region of $1.0 < p_T < 5.0$ GeV/ c have been of great interest for a long time since thermal photons from Quark Gluon Plasma (QGP) are considered to contribute predominantly [1]. Thermal photons can provide key inputs to describe a space-time evolution of the matter created by heavy-ion collisions, such as an initial temperature of the matter, thermalization time and so on. Attempts to measure such low p_T direct photons using electromagnetic calorimeters (EMCals) could not succeed since a finite energy resolution of the EMCal precludes separation of a direct photon signal from a huge amount of background photons from hadron decays. Recently, the PHENIX experiment demonstrated that direct photon yield can be obtained even in the low p_T region via di-electron measurements for $p+p$ and Au+Au collisions since virtual direct photon conversions make an enhanced yield of di-electrons over the known hadron decay contributions [2]. According to the $p+p$ and Au+Au results, a clear excess over an expected hard photon yield from the $p+p$ data is observed in $p_T < 3.0$ GeV/ c for $\sqrt{s_{NN}} = 200$ GeV Au+Au collisions.

However, nuclear effects, which are initial state effects involved in $A+A$ collisions not in $p+p$, may modify the direct photon yield in the low p_T region [3]. Thus, nuclear effects need to be investigated to extract the QGP medium effects from the observed excess yield. The $\sqrt{s_{NN}} = 200$ GeV $d+Au$ data taken in the Year-2008 RHIC run can contribute to quantify nuclear effects on direct photon production, and the latest $d+Au$ results are shown in this report.

2. Analysis

All combinations between electrons and positrons in an event are taken. The foreground e^+e^- mass distribution contains various components from different sources. The contributions from sources other than virtual direct photon conversions and known hadron decays are removed using well-established analysis techniques [4].

The virtual direct photon fraction in the obtained e^+e^- mass distribution can be determined by utilizing the mass shape difference between virtual direct photon conversions and known hadron decays according to an important relation between the photon production process and the associated e^+e^- production process, which is described as a higher order diagram by replacing real γ with $\gamma^* \rightarrow e^+e^-$. The relation can be expressed as:

$$\frac{d^2n_{ee}}{dm_{ee}} = \frac{2\alpha}{3\pi} \frac{1}{m_{ee}} \sqrt{1 - \frac{4m_e^2}{m_{ee}^2}} \left(1 + \frac{2m_e^2}{m_{ee}^2}\right) S(m_{ee}) dn_\gamma, \quad (1)$$

where α is the fine structure constant, m_e and m_{ee} are the

masses of the electron and the e^+e^- pair, respectively, and $S(m_{ee})$ is a process-dependent factor that goes to 1 as $m_{ee} \rightarrow 0$ or $m_{ee}^2 \ll p_T^2$ for virtual direct photon conversions. In the case of π^0 and η Dalitz decays, $S(m_{ee})$ is given as $S(m_{ee}) = |F(m_{ee}^2)|^2 \left(1 - \frac{m_{ee}^2}{m_h^2}\right)^3$ [5], where $F(m_{ee}^2)$ is the form factor and m_h is a hadron mass. The factor $S(m_{ee})$ is obviously zero for $m_{ee} > m_h$. This cutoff can dramatically improve the ratio of the direct photon signal to the hadronic background (S/B) in $m_{ee} > m_{\pi^0}$, since more than 80% of hadron decay e^+e^- pairs come from $\pi^0 \rightarrow \gamma e^+e^-$.

To determine the virtual direct photon contribution from the e^+e^- mass distribution, the kinematic region in $0.1 < m_{ee} < 0.3$ GeV/ c^2 and $p_T > 1.0$ GeV/ c is selected since this region satisfies the key assumption of $S(m_{ee}) \sim 1$ for virtual direct photon conversions with a small contribution of $\pi^0 \rightarrow \gamma e^+e^-$. Equation 2 is fitted to the data to quantify the enhanced yield due to virtual direct photon conversions:

$$f(m_{ee}; r_{\gamma^*}) = (1 - r_{\gamma^*}) \cdot f_{cock}(m_{ee}) + r_{\gamma^*} \cdot f_{dir}(m_{ee}), \quad (2)$$

where f_{cock} is the mass distribution from the known hadron decays and f_{dir} is the expected distribution from the direct virtual photon decays, and r_{γ^*} is the virtual direct photon fraction. The mass distribution from the known hadron decays is calculated by a Monte Carlo calculation which incorporates the measured yields of the hadrons at the PHENIX. Figure 1 shows the e^+e^- mass distribution in $d+Au$ col-

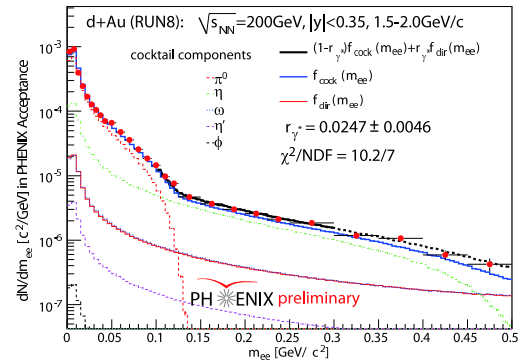


Figure 1. The e^+e^- mass distribution in $d+Au$ collisions for $1.5 < p_T < 2.0$ GeV/ c together with the fit result by Eq. (2).

lisions for $1.5 < p_T < 2.0$ GeV/ c together with the fit result by Eq. (2) shown with a thick solid line. The extended fit result for $m_{ee} > 0.3$ GeV/ c^2 , shown as a dotted line, also well describe the data. The virtual direct photon fraction in $d+Au$ collisions for every 0.5 GeV/ c in $1.0 < p_T < 6.0$ GeV/ c is obtained as shown in Fig. 2 side by side with the $p+p$ and Au+Au results. Expectations

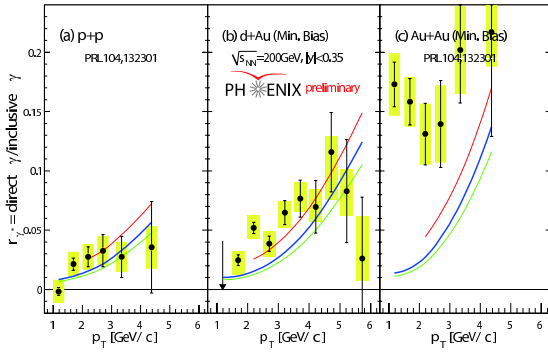


Figure 2. The obtained virtual direct photon fraction in $d+Au$ collisions for every $0.5 \text{ GeV}/c$ in $1.0 < p_T < 6.0 \text{ GeV}/c$ side by side with the $p+p$ and Au+Au results.

from a NLO pQCD calculation [2] with different theoretical scales are also shown for each collision system. Obviously the Au+Au result has a different trend in $p_T < 2.0 \text{ GeV}/c$ compared to the $p+p$ and $d+Au$ results which are almost consistent with the NLO pQCD expectations.

3. Result

Finally, the direct photon yield in $d+Au$ collisions is obtained from the measured virtual direct photon fractions multiplied by the inclusive real photon yield. Figure 3

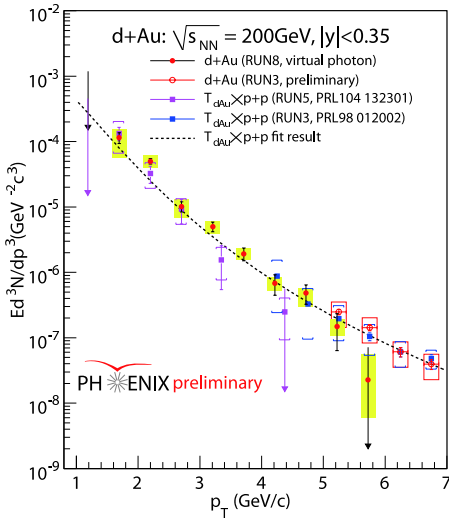


Figure 3. The direct photon spectrum in $d+Au$ collisions compared to the $p+p$ result scaled to the number of binary collisions.

shows the obtained direct photon spectrum in $d+Au$ collisions compared to the $p+p$ result scaled to the number of binary collisions. The $p+p$ and $d+Au$ results are shown as box and circle symbols, and the results from analyses with di-electrons and EMCals are indicated as closed and open symbols, respectively. The binary-scaled $p+p$ fit result is also drawn as a dotted line. The $d+Au$ result is in agreement with the binary collision-scaled $p+p$ result for a wide p_T range. Thus, nuclear effects on the direct photon production seem to be very small.

Furthermore, the $d+Au$ result can serve as a new baseline for the Au+Au result. Figure 4 shows the direct pho-

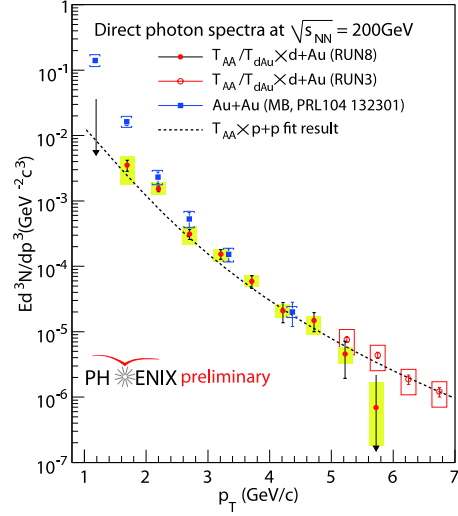


Figure 4. The direct photon spectrum in minimum bias Au+Au collisions compared to the binary collision-scaled $d+Au$ result.

ton spectrum in minimum bias (MB) Au+Au collisions compared to the binary collision-scaled $d+Au$ result. The square and circle symbols show the results in MB Au+Au and $d+Au$ collisions. The Au+Au result can not be described by the scaled $d+Au$ result, especially the significant enhanced yield over the scaled $d+Au$ result is seen for $p_T < 2.0 \text{ GeV}/c$. This fact implies that an additional source of the direct photon production other than initial state effects like nuclear effects exists in Au+Au collisions.

4. Summary

The direct photon measurements via di-electrons has been successfully made for $d+Au$ collisions as well as both $p+p$ and Au+Au collisions at the PHENIX experiment. The $d+Au$ result is consistent with the binary-scaled $p+p$ result indicating that nuclear effects on the direct photon production is very small. Moreover, the significant excess over the binary-scaled $d+Au$ result is still seen for $p_T < 2.0 \text{ GeV}/c$ in Au+Au collisions, implying that an additional source of the direct photon production exists in Au+Au collisions.

References

- [1] S. Turbide *et al.*, Phys. Rev. C **69**, 014903 (2004).
- [2] A. Adare *et al.*, for the PHENIX collaboration, Phys. Rev. Lett. **104**, 132301 (2010).
- [3] I. Vitev, B.W. Zhang, Phys. Lett. B **669**, 337 (2008).
- [4] A. Adare *et al.*, for the PHENIX collaboration, Phys. Rev. C **81**, 034911 (2010).
- [5] L.G. Landsberg, Phys. Rep. **128**, 301 (1985).

Neutral Pion Production with Respect to the Azimuthal Angle in Au+Au Collisions at $\sqrt{s_{NN}} = 200$ GeV

Y. Aramaki, T. Sakaguchi^a, G. David^a, H. Hamagaki^b, for the PHENIX Collaboration

RIKEN (The Institute of Physical and Chemical Research)

^a*Physics Department, Brookhaven National Laboratory*

^b*Center for Nuclear Study, Graduate School of Science, University of Tokyo*

1. Introduction

The production of π^0 in $^{197}\text{Au}+^{197}\text{Au}$ collisions at the center-of-mass energy per nucleon pair ($\sqrt{s_{NN}}$) of 200 GeV has been measured at the PHENIX experiment at Relativistic Heavy Ion Collider in Brookhaven National Laboratory (BNL). There were two major observations for heavy-ion collision at RHIC: jet quenching and large azimuthal anisotropy v_2 . The observed yield of high- p_T π^0 in Au+Au collisions is suppressed by a factor of 5 compared to that in the superposition of nucleon-nucleon collisions, while the yield of π^0 in $d+\text{Au}$ is not suppressed. Therefore, the yield suppression in Au+Au is not initial state effect such as Cronin effect or shadowing observed in $d+\text{Au}$ collisions, and the final state effect is called ‘‘jet quenching’’ [1].

The large azimuthal anisotropy v_2 of hadrons at low p_T was observed, and the hydrodynamical calculation can reproduce the data up to the low- p_T region of about 2 GeV/c [2]. Therefore, it is suggested that the produced medium is strongly coupled perfect fluid.

Parton energy loss models to describe jet quenching predict that the magnitude of the energy loss in the medium depends on the path length L which partons pass through. Thus, the measurement of the energy loss with respect to the path length is expected to enable us to obtain the detail information about parton energy loss mechanism. The path length is strongly associated with the azimuthal angle from the reaction plane in collisions, since the matter created in the non-central heavy-ion collision is almond shape.

If the azimuthal angular distribution of emitted particles is written in the form of Fourier expansion, the second harmonic coefficient is expressed as the strength of the azimuthal anisotropy v_2 . The collective flow is dominant for the azimuthal anisotropy v_2 at low- p_T region, while the v_2 with high p_T is expected to have the information about the initial collision geometry such as the path length. In order to reduce the effect of the collective flow, the azimuthal anisotropy with high p_T should be measured. Since the angle of the reaction plane plays a important role to measure the v_2 , new detectors, Muon Piston Calorimeter (MPC) and Reaction plane detector (RXN) to determine the angle of the reaction plane were installed in PHENIX. The MPC and RXN were used for the determination of the reaction plane, and the azimuthal anisotropy v_2 was measured. Here we report the measurement of the azimuthal anisotropy v_2 by using MPC and RXN.

2. Azimuthal angular dependence of R_{AA}

For the yield measurement of π^0 , two-gammas decay mode from π^0 obtained in RHIC Year-7 Au+Au run was used. The gammas are identified with two kinds of electromagnetic calorimeters; one is the sampling type of lead and scintillator and the other is Cherenkov type of lead-glass.

The nuclear modification factor, R_{AA} , is defined to quantify the suppression of yield in heavy-ion collisions. The R_{AA} as a function of p_T and the centrality ($cent$) is given as,

$$R_{AA}(p_T, cent) = \frac{dN/dy_{AA}}{dN/y_{pp}\langle N_{col}(cent) \rangle}, \quad (1)$$

where dN/dy_{AA} and dN/dy_{pp} correspond to the yields in Au+Au and $p+p$ collisions, respectively, and $\langle N_{col}(cent) \rangle$ is an average number of nucleon-nucleon collisions for a given impact parameter which is associated to the centrality. If R_{AA} is equal to one, the particle production in Au+Au collisions can be considered as a superposition of nucleon-nucleon collisions. In this analysis, the $p+p$ data in RHIC Year-5 run was used as the reference.

The nuclear modification factor R_{AA} of π^0 with respect to the azimuthal angle is given as,

$$R_{AA}(\Delta\phi_i, p_T) = F(\Delta\phi_i, p_T) \cdot R_{AA}(p_T), \quad (2)$$

where $F(\Delta\phi_i, p_T)$ is the ratio of the relative yield, and the ratio is given as,

$$F(\Delta\phi_i, p_T) = \frac{N(\Delta\phi_i, p_T)}{\sum_{i=1}^6 N(\Delta\phi_i, p_T)}, \quad (3)$$

where $N(\Delta\phi_i, p_T)$ is the number of detected π^0 s in a given azimuthal angle bin and p_T bin. Since the created matter has an almond shape, it is symmetrical to the short or long axis of the matter.

Since the detection efficiency and acceptance are corrected for the measurement of the azimuthal-integrated R_{AA} of π^0 , the $F(\Delta\phi_i, p_T)$ is not needed to correct the efficiency. However, $F(\Delta\phi_i, p_T)$ is needed to correct for the resolution of the reaction plane, since the detector determined the reaction plane has a finite resolution.

The azimuthal anisotropy v_2^{raw} in the raw azimuthal angular distribution of π^0 is corrected with the event plane resolution. The ratio of the relative yield of π^0 is given as,

$$F(\Delta\phi_i, p_T) = \frac{F(\Delta\phi_i, p_T)^{\text{meas}}}{C_{\text{width}}} \cdot \left[\frac{1 + 2v_2^{\text{corr}} \cos(2\Delta\phi)}{1 + 2v_2^{\text{raw}} \cos(2\Delta\phi)} \right]. \quad (4)$$

where C_{width} is the number of azimuthal angular bins, and C_{width} is equal to 6 in the case.

Using Eq. 2 and Eq. 4, the R_{AA} with respect to the azimuthal angle are calculated. Figure 1 shows the azimuthal angular dependence of the R_{AA} of π^0 for each centrality class. The systematic uncertainty for the v_2 indicates the band on $R_{AA} = 1$, and the right-side band is the systematic uncertainties of the number of binary collisions, $p + p$ normalization, and the feed-down from K_S^0 . As the centrality increases, the azimuthal angular dependence seems to be large.

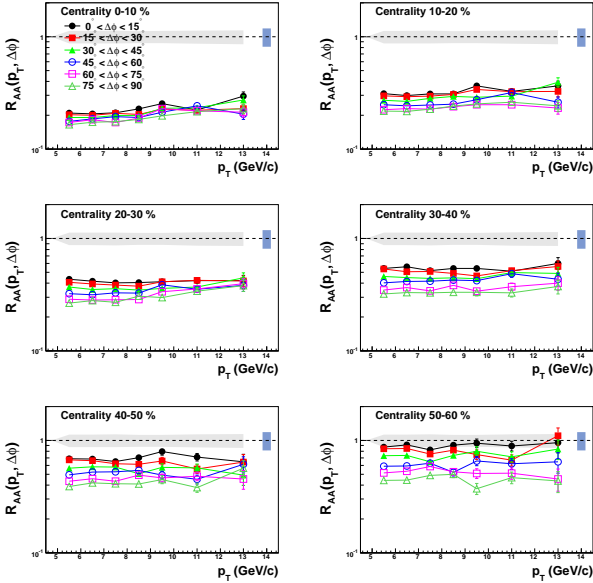


Figure 1. The R_{AA} of π^0 with respect to the azimuthal angle as a function of p_T for each centrality class. The point-by-point systematic uncertainties for the $R_{AA}(\Delta\phi)$ are not shown.

3. Comparison of $\pi^0 R_{AA}(p_T, \Delta\phi)$ and models

The R_{AA} with respect to the azimuthal angle are compared to the two models at the centrality 20–30 % where the $R_{AA}(p_T, \Delta\phi)$ was measured with the smallest uncertainties.

The ASW approach which is used with the comparison includes only radiative energy loss process based on pQCD [3]. The other approach is proposed the energy loss model incorporating the ASW formalism with Anti-de Sitter space/Conformal Field Theory (AdS/CFT) correspondence [4]. The AdS/CFT correspondence which is one of frameworks to describe the strong-coupled system has been developed. For the model, the hard process is treated perturbatively, and the ASW formalism is used, while the soft process which is assumed to be strong coupling dynamics are used with the AdS/CFT correspondence. This model has stronger path-length dependence for the energy loss than the standard ASW formalism.

Figure 2 shows the comparison with the data and the expectation from the two models. The in-plane and out-of-plane R_{AA} are extracted from Fig. 1. The statistical and systematic uncertainties of the $R_{AA}(\Delta\phi)$ indicate the brackets and boxes, respectively. The bands are expressed as

same as Fig. 1. The ASW model based on pQCD fails to reproduce the data especially in lower p_T region, while the ASW model using AdS/CFT correspondence seems to agree with the data well. It suggests that the data requires more stronger path-length dependence.

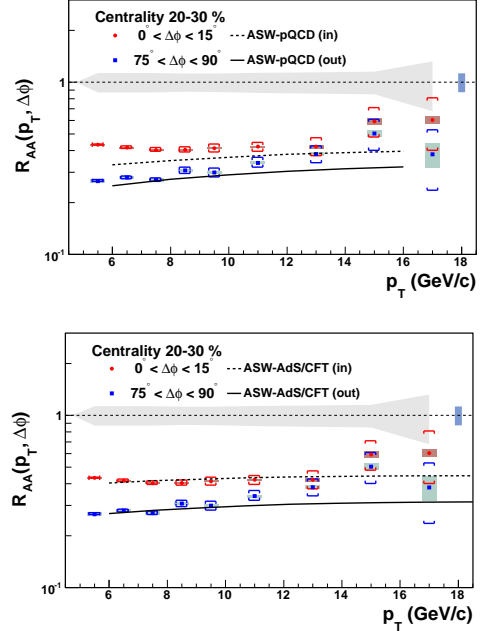


Figure 2. The in-plane (closed circles) and out-of-plane (closed squares) R_{AA} of π^0 as a function of p_T at centrality 20–30 %. The lines in the upper figure is the ASW model based on pQCD, and the lines in the lower figure is the ASW model using AdS/CFT correspondence.

4. Summary

The R_{AA} with respect to the azimuthal angle are measured, it suggests from the model comparison that pQCD might not be applicable to the strong-coupled dynamics in the hot and dense matter created at RHIC. The parton energy loss model with AdS/CFT correspondence can reproduce the azimuthal angular dependence for the R_{AA} , and it predicts that stronger path-length dependence for the energy loss than models based on pQCD. However, one should recognize that the AdS/CFT correspondence is one of approaches to the strong-coupled system and CFT is crucially different from QCD and the parton energy loss mechanism should eventually be clarified by primary QCD calculation.

References

- [1] S.S. Adler *et al.*, Phys. Rev. Lett.**91**, 072301 (2003).
- [2] S.S. Adler *et al.*, Phys. Rev. Lett.**91**, 182301 (2003).
- [3] T. Renk *et al.*, Phys. Rev. **C75**, 031902 (2007).
- [4] C. Marquet *et al.*, Phys. Lett. **B685**, 270 (2010).

Operation and Performance of the Silicon Pixel Detector for the PHENIX Vertex Tracker

R. Akimoto, Y. Akiba^{a, c}, H. Asano^{b, c}, T. Gunji, T. Hachiya^a, H. Hamagaki, M. Kurosawa^c,
H. Sako^{a, d}, S. Sato^{a, d}, A. Taketani^{a, c} (for the PHENIX Collaboration)

Center for Nuclear Study, Graduate School of Science, University of Tokyo

^a*RIKEN (The Institute of Physical and Chemical Research)*

^b*Department of Physics, Kyoto University*

^c*RIKEN BNL Research Center, USA*

^d*Japan Atomic Energy Agency*

1. Introduction

The PHENIX experiment investigates properties of Quark Gluon Plasma (QGP) and spin structure inside polarized proton at Relativistic Heavy Ion Collider (RHIC). We have developed a silicon vertex tracker (VTX) for the PHENIX experiment. The detector is mainly aimed for the measurement of heavy quark (charm and bottom), which is an important probe to study the properties of QGP and to study spin structure function of gluon.

The VTX has been successfully installed at the end of 2010 and $p + p$ collision and Au + Au collision data were taken with the VTX.

In this article, the performances of the VTX during commissioning and physics data taking with $p + p$ and Au + Au run are shown.

2. Physics requirement

The VTX is required to be operated in high multiplicity environment ($dN/d\eta|_{\eta=0} = 687 \pm 0.7(\text{stat.}) \pm 37(\text{syst.})$ in central Au + Au collisions [1]). In the condition, it is the only way for flavor identification of heavy quark to measure distance of closest approach (DCA) of decayed electron or positron from the collision vertex.

The requirements for the VTX are as follows:

- the resolution of the DCA is required to be less than $100 \mu\text{m}$, which is driven by the difference of lifetime and q-value of D and B mesons;
- in order to avoid merging hit clusters, occupancy should be less than 1 % for readout pixels.

3. VTX

The VTX is a barrel detector with four layers. It is installed around the beam collision vertex and covers rapidity of $|\eta| < 1.2$ and almost 2π in azimuthal angle. The magnetic field strength where the VTX is installed is about 0.9 T and its direction is along the beam axis.

A silicon pixel detector consists of inner two layers. Major design parameters are summarized in Table 1. A silicon sensor for the pixel detector has $p^+ - n$ structure whose thickness is $200 \mu\text{m}$. ALICE1LHCB chip [3] is utilized as a readout chip. The chip was originally developed for the silicon pixel detector for the ALICE experiment and the ring imaging cherenkov detector for the LHCb experiment. The pixel modules is made of 16 of the chips, and the inner and the outer layers of the pixel detector are consisted of

Layer	0	1
Radius from the beam axis	2.6 cm	5.1 cm
Pixel size	$50 \mu\text{m} (\phi) \times 425 \mu\text{m} (z)$	
Radiation length	1.2 %	
Occupancy	< 0.53 %	< 0.16 %

Table 1. Major design parameters for the pixel detector. ϕ represents the azimuthal direction and z represents the beam direction. The maximum of the occupancies are evaluated with the multiplicity at central Au + Au collision with $\sqrt{s_{NN}} = 200 \text{ GeV}$.

10 and 20 of the modules, respectively. The position resolution was evaluated by beam test using 120 GeV proton beam and it is $14 \mu\text{m}$ and $152 \mu\text{m}$ for the azimuthal and the beam directions, respectively [2].

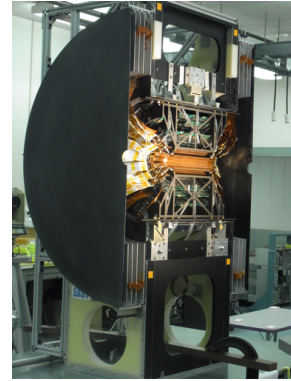


Figure 1. Overview of the VTX.

4. Commissioning

ALICE1LHCB chip has preamplifiers, shapers, discriminators, delay units, and FIFOs. Signals are converted to binary hit information at the discriminators and are delayed at the delay units in order to synchronize with the event trigger. Therefore, latency of the event trigger and threshold at the discriminator should be adjusted.

4.1. Trigger latency

Rates of the events with at least one hit pixel were evaluated with changing the trigger latency. Timing acceptance is one beam clock tick whose width is about 100 ns. Figure 2 shows a distribution of the rate of the event with at least one hit pixel, as a function of the latency. The proper latency is found to be around 9.5.

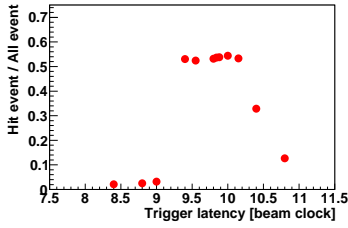


Figure 2. The hit event rate distribution as a function of the event trigger latency. Unit of the latency is the beam clock.

4.2. Threshold

The threshold at the discriminator was adjusted by evaluating noise hit rate with the beam being circulated and with trigger whose latency was five beam clock ticks longer than the adjusted latency. Figure 3 shows a distribution of the adjusted thresholds for all of the chips. The horizontal axis represents the ratio of the threshold to the most probable value (MPV) for charge deposit of the minimum ionizing particle (MIP). The thresholds were set to be much lower values than MPV of the MIP.

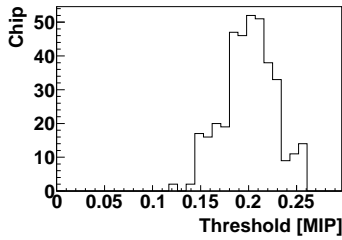


Figure 3. The distribution of the threshold at the discriminators of all of the readout chips.

5. Performance

5.1. Operating status

The fraction of the normally working chips is 96.9 %, when they were installed. But some of the chips became unfunctional due to problems of readout electronics and the fraction decreased to be 73.3 % at the end.

5.2. Noise occupancy

Noise hit occupancies of all of the chips were evaluated with the adjusted thresholds and with the same setup of the threshold adjustment. Figure 4 shows the distribution of the noise hit occupancies. The mean of the occupancies is about 5×10^{-6} .

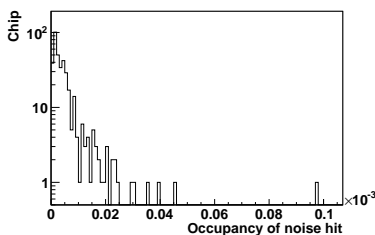


Figure 4. The distribution of the noise hit occupancies of all of the readout chips.

5.3. Hit correlation

Clear correlations in azimuthal angle between hits at different layers can be seen though sensor position calibration has not been completed. The left panel of Fig.5 shows the correlation between the hits in the inner and the outer layers of the pixel detector. The width of the peak is mainly come from track bending by the magnetic field.

A correlation between hits of the pixel detector and those of other detector can also be seen clearly. The right panel of Fig.5 shows the correlation between the collision vertex in the beam axis measured by Beam Beam Counter (BBC) [5] and that measured by the pixel detector. The way to determine the vertex with the pixel detector is as follows:

- calculate projection position from all pairs of hits in different layers to the beam axis;
- find peak of the projected position;
- fit the peak by Gaussian function and the vertex corresponds to the mean of the Gaussian function.

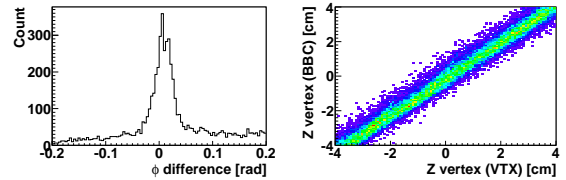


Figure 5. The left figure shows correlation of hit positions in azimuthal direction between the hits in the inner and the outer layers of the pixel detector. The right figure shows correlation between the collision vertex measured by BBC and that measured by the pixel detector.

6. Summary

The VTX has been installed in the PHENIX detector. Parameters for data taking was properly tuned and it is demonstrated that tracking using the VTX is achieved.

As an outlook, the detector position should be calibrated precisely to measure DCA for the flavor identification of heavy quarks.

References

- [1] S. S. Adler *et al.* Phys. Rev. C **71** (2005) 034908.
- [2] M. Kasai *et al.*, RIKEN Accel. Prog. Rep. **42** (2009) 212.
- [3] W. Snoeys *et al.* Nucl. Instr. Meth. A **465** (2001) 176.
- [4] M. Garcia-Sciveres *et al.* Nucl. Instr. Meth. A **511** (2003) 171.
- [5] K. Ikematsu *et al.* Nucl. Instr. and Meth. A **411** (1998) 238.

Study of TPC $E \times B$ distortion at LHC-ALICE experiment

Y. Hori, S. Rossegger^a, J. Thomas^b, M. Ivanov^b, C. Ivan^b, T. Gunji, H. Hamagaki

Center for Nuclear Study, Graduate School of Science, University of Tokyo
European Organization for Nuclear Research (CERN)^a
GSI Helmholtzzentrum für Schwerionenforschung GmbH^b

1. Introduction

Time Projection Chamber (TPC) is a main central tracking device in ALICE detector at LHC. TPC is cylindrical shape and operated in 0.5 T solenoidal B field parallel to the E field axis as shown in Figure 1. A central HV electrode divides TPC into two volumes, which are called A side and C side. The direction of E field at A side is opposite to that of C side. For each side, a maximum drift length is ~ 2.5 m [1].

The direction of electron drift is same as that of E field if $E \times B$ is perfectly zero. However, many imperfect structures lead to E and B field distortions, which in turn lead to space point distortions.

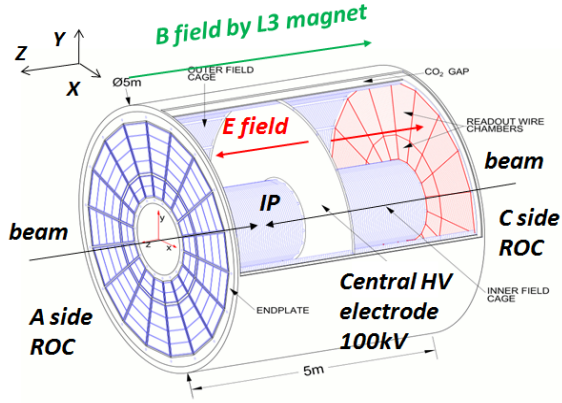


Figure 1. ALICE TPC schematic design

2. Calculation of TPC $E \times B$ distortions

An equation below to calculate space point distortions can be derived from steady-state Langevin equation with 2nd order approximation, which describes a motion of drift electron under E and B field [2].

$$\begin{pmatrix} \delta r \\ r \delta \phi \end{pmatrix} = \begin{pmatrix} c_0 & c_1 \\ -c_1 & c_0 \end{pmatrix} \begin{pmatrix} \int \frac{E_r}{E_z} dz \\ \int \frac{E_\phi}{E_z} dz \end{pmatrix} + \begin{pmatrix} c_2 & -c_1 \\ c_1 & c_2 \end{pmatrix} \begin{pmatrix} \int \frac{B_r}{B_z} dz \\ \int \frac{B_\phi}{B_z} dz \end{pmatrix},$$

$$\text{with } c_0 = \frac{1}{1 + T_2^2 \omega^2 \tau^2}, c_1 = \frac{T_1 \omega \tau}{1 + T_1^2 \omega^2 \tau^2},$$

$$\text{and } c_2 = \frac{T_2 \omega^2 \tau^2}{1 + T_2^2 \omega^2 \tau^2},$$

where T_1 and T_2 parameters depend on B and E field configuration. Magboltz simulation indicates that both T_1 and T_2 are equal to 1 [3]. E_r and E_ϕ are calculated by a poisson relaxation method with the TPC geometry [4]. B_r and B_ϕ are

obtained from the B field map parametrized with Chebyshev polynomials, which is based on precise B field measurement.

3. Difference of Laser track distortions with Gating Grid Voltage (GGV) scan

The Gating Grid Voltage (GGV) decides the E field structures around the gating grid, which is in the ReadOut Chamber (ROC) of TPC. An ideal setting of GGV is 70V. The difference of laser track distortions with GGV = 40V and 70V can be measured. Figure 2 shows the result of this measurement at $B = 0$. The longitudinal axis of Figure 2 is a difference of $r\phi$ distortions. The data points clearly prefer to prediction with $c_0 = 1, c_1 = 1$. This result shows precision of E field distortions calculation.

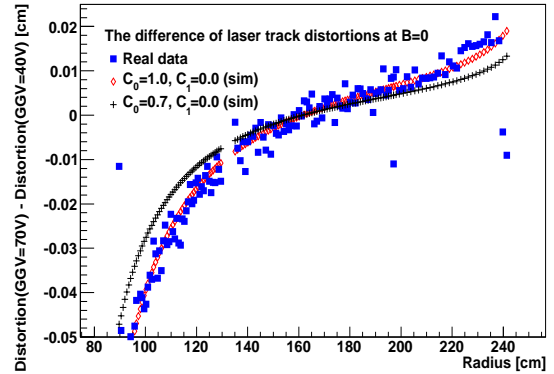


Figure 2. A difference of laser track $r\phi$ distortions with GGV scan vs. radial position of space point

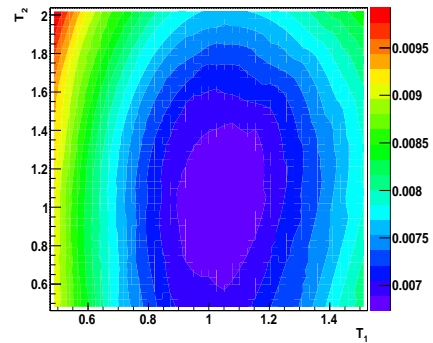


Figure 3. Contour plot for T_1, T_2 optimization with GGV scan data at $B = 0.5$ T

A same measurement was performed at $B = 0.5$ T in order to extract T_1 , T_2 parameters at $B = 0.5$ T. Figure 3 shows RMS of distribution of residual between real data and model calculation with various T_1 , T_2 values. A best value of T_1 , T_2 is 1.0 ± 0.1 and 1.0 ± 0.3 . These values agree with Magbolz results.

4. $E \times B$ twist distortions and A-C vertex shift

The space point distortions due to an angular mismatch between global axis of E and B field can be significant if TPC is slightly inclined in L3 magnet. This $E \times B$ twist distortion can be calculated in a compact form:

$$\begin{pmatrix} \delta x \\ \delta y \end{pmatrix} = \begin{pmatrix} c_2 & -c_1 \\ c_1 & c_2 \end{pmatrix} \begin{pmatrix} \theta_x z_{drift} \\ \theta_y z_{drift} \end{pmatrix}$$

where z_{drift} is a drift length of electron, $\theta_{x,y}$ are the angles between x, y axis and twist vector. The distortions of space point in A side is opposite to that in C side because E field vector in A side is opposite to that in C side as shown in Figure 4. As a result, the distortion of tracks in A side is a parallel shift to the opposite direction of C side track distortion.

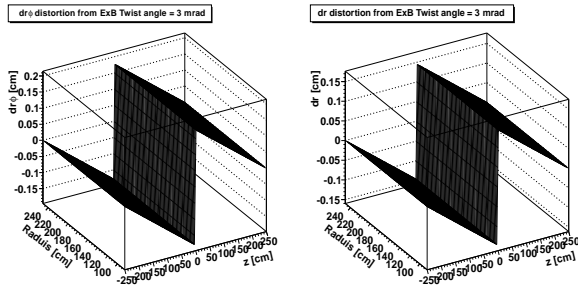


Figure 4. $E \times B$ twist distortion map with twist angle = 3 mrad, the sign of dr and $dr\phi$ is changed at $z=0$ cm.

The effect of $E \times B$ twist distortion can be observed by the measurement of the shift between the collision vertex reconstructed with A side tracks and that of C side tracks, which is called A-C vertex shift. Figure 5 shows that A-C vertex shift is proportional to $E \times B$ twist angle if twist angle is small enough in the MC simulation study.

The A-C vertex shift was found in $p+p$ collision data as shown in Figure 6. Primary vertex is reconstructed with all ITS-TPC tracks and is positioned in the middle of A and C side vertex. Positions of A and C side vertex are swapped with negative and positive B field polarity. Observed A-C vertex shift is ~ 0.33 cm. This results in $\theta_x = -1.7$ mrad, $\theta_y = -0.94$ mrad if this A-C vertex shift is only from $E \times B$ twist distortions. It is confirmed that possible distortions from B field non-uniformity and TPC misalignment can not cause A-C vertex shift by MC simulation. It is also found that A-C vertex shift due to other E field non-uniformity is within a few hundreds μm in $B=0$ runs. The A-C vertex shift is reduced to $300\mu\text{m}$ with correction of $E \times B$ twist distortions according to the twist values above.

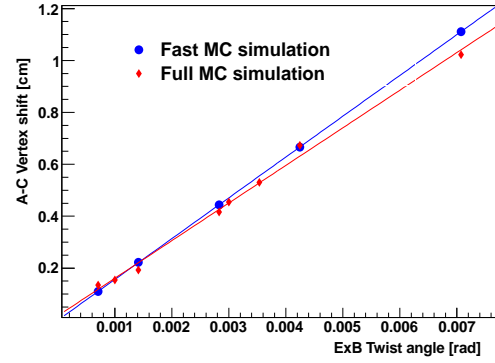


Figure 5. Relation between twist angle and A-C vertex shift calculated by MC simulation

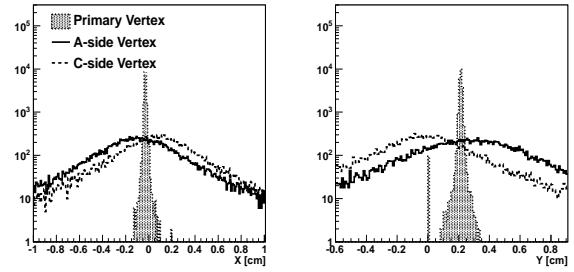


Figure 6. A-C vertex shift measured in $p+p$ collision data

5. Summary

A framework to calculate $E \times B$ distortions and correct them during track reconstruction was constructed. A calculation of E field distortion due to GGv error agrees with the measurements of laser track distortions in GGv scan $B=0$ runs very well. T_1 and T_2 parameters in case of ALICE TPC configuration are extracted with GGv scan $B=0.5$ T runs and agree with Magbolz simulation results. A-C vertex shift found in $p+p$ collision data can be considered as a result of $E \times B$ twist distortions and twist angle was extracted with a help of full MC simulation study.

References

- [1] The ALICE TPC, *a large 3-dimensional tracking device with fast readout for ultra-high multiplicity events*, Nuclear Inst. and Methods in Physics Research, A (2010), NIM.Ref.: NIMA51562
- [2] W. Blum, W. Riegler and L. Roland, *Particle Detection with Drift Chamber*, 2nd ed.(Springer, 2008)
- [3] S. Rossegger, *Simulation and Calibration of ALICE TPC Including Innovative Space Charge Calculations*, PhD thesis, University of Technology, Graz, 2009, CERN-THESIS-2009-124
- [4] R.V. Southwell, *Relaxation methods*, Oxford engineering science series (Oxford Univ. Press, 1940)

Simulation study of the Forward Calorimeter for LHC-ALICE

T. Tsuji, H. Hamagaki, T. Gunji, Y. Hori

Center for Nuclear Study, Graduate School of Science, University of Tokyo

1. Introduction

The parton density inside the proton and a nucleus is described by the parton distribution function (PDF). According to the results given by the HERA experiments, gluon PDF grows quickly with decreasing Bjorken's x (x_B) and gluon density becomes much larger than the valence and sea quark densities. According to Quantum chromodynamics (QCD), gluon density tends to saturate due to the balance between gluon splitting and gluon fusion at high density. Such state is called as gluon saturation [1].

At the ALICE, the study of gluon distribution in heavy nuclei has been done with p+Pb collision. In a heavy ion collision, the nucleus acts as an amplifier of the saturation effect because of the thickness of the nucleus. In the simple process $1 + 2 \rightarrow 3 + 4$, Bjorken's x_B of colliding partons are related to rapidity y of produced particles as,

$$x_{B1} = \frac{p_T}{\sqrt{s}}(e^{y_3} + e^{y_4}), \quad x_{B2} = \frac{p_T}{\sqrt{s}}(e^{-y_3} + e^{-y_4}),$$

where p_T is the transverse momentum of the scattered partons and \sqrt{s} is center-of-mass energy. These relations indicate that small x is accessible by measuring particles at forward rapidity. The BRAHMS experiment at RHIC reported the suppression of charged particle yield in d+Au collisions at forward rapidity, which is consistent with the saturation of gluons at small- x [2].

The forward calorimeter (FOCAL) has been proposed to study more extensively the gluon distributions in proton and in nuclei at small x via measurements of inclusive direct photon production and of production of π^0 at forward rapidity.

2. FOCAL for the ALICE

The FOCAL is designed to cover the forward region. The layout of FOCAL is summarized in Table 1. Figure 1 shows

Distance from IP	350 cm
Outer Radius	70 cm
Inner Radius	10 cm
Pseudo-rapidity coverage	2.5 – 4.2
ϕ coverage	2π
Area coverage	0.6 m ²

Table 1. FOCAL layout of the ALICE

a longitudinal structure of a single FOCAL supertower. It is a silicon-tungsten sampling calorimeter, which is longitudinally composed of 3 calorimeter segments. The size of Si readout pads is 1.1×1.1 cm². The thickness of each Si pad detector is 0.5 mm and that of W absorber is 3.5 mm. Each segment has 7 radiation length. Since tungsten has a small Moliere radius (9.3 mm), two photons decayed from

π^0 can be separate up to high p_T . Tungsten also has an excellent ratio of radiation and interaction lengths, which is important for electromagnetic energy measurements in the presence of heavy hadronic background. In addition, there are three sections of strip detectors with 700 μ m pitch located in the first longitudinal segment to identify π^0 s to high energy even when there is an overlap of showers in the pads. This also allows discrimination of direct photons and high energy π^0 s.

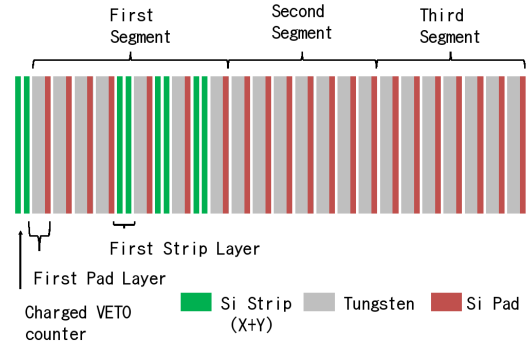


Figure 1. Longitudinal structure of a single calorimeter supertower showing the location of the three calorimetric segments.

3. FOCAL performance in p+p and p+Pb collisions

We evaluated FOCAL performance of π^0 reconstruction in p+p and p+Pb collisions. In order to study performance of FOCAL, we have done simulations by implementing geometry and material into AliRoot which is simulation and analysis framework for the ALICE.

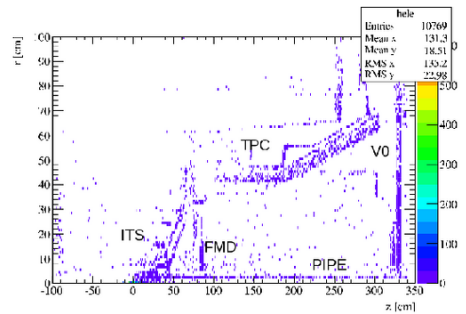


Figure 2. Origin of secondary e^\pm and γ in p+Pb collisions.

Figure 2 shows origin of secondary e^\pm and γ in p+Pb collisions. If number of e^\pm and γ from collision is 100 %, additional contribution is 12.1 % from pipe, 10.7 % from the V0 detector, 1.6 % from the Inner Tracking System (ITS), 8.2 % from the Forward Multiplicity Detector (FMD) and 1.3 % from the ALICE Time-Projection Chamber (TPC).

Figure 3 (left) shows signal to noise ratio and Fig. 3 (right) shows a π^0 reconstruction efficiency. Filled and open ones are efficiencies with and without secondary

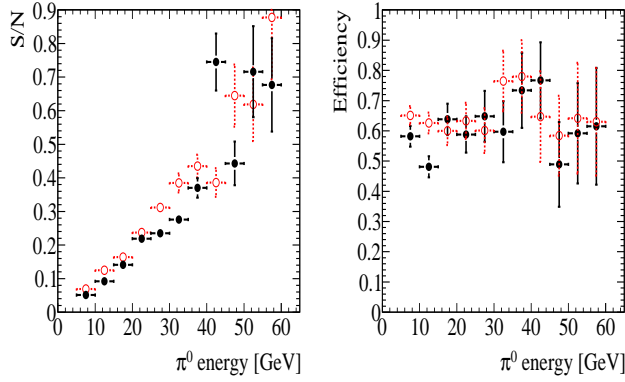


Figure 3. Left: Signal to noise ratio. Right: π^0 reconstruction efficiency. (Filled and open ones show efficiency with and without secondary particles, respectively.)

particles, respectively. S/N is slightly worse by secondary particles while efficiency is almost unchanged.

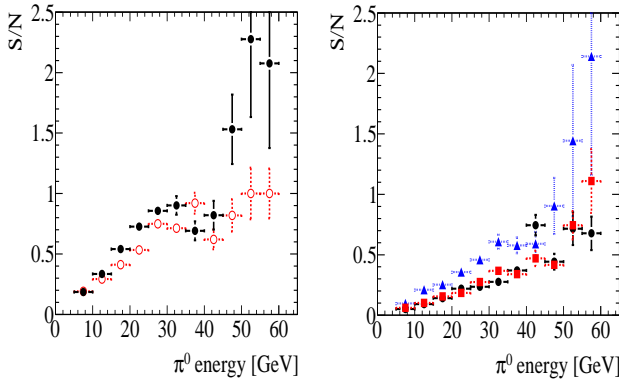


Figure 4. Left: S/N of π^0 by pads in p+p collision. Right: S/N of π^0 by pads in p+Pb collision.

Figure 4 (left) shows S/N of π^0 by pads in p+p collision. Filled and open ones show S/N for minimum bias and jet process, respectively. Figure 4 (right) shows S/N of π^0 by pads in p+Pb collision. Circles, squares and triangles show S/N for impact parameter with 0-3 fm, 3-6 fm and 6-9 fm, respectively. S/N is small at p+Pb central collision because multiplicity is large in p+Pb central collision.

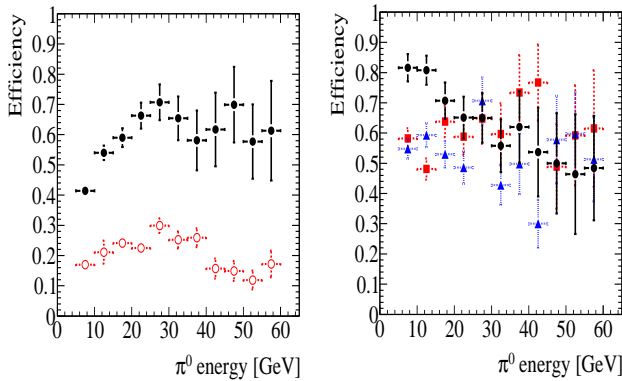


Figure 5. Left: π^0 detection efficiency by pads in p+p collision. Right: π^0 detection efficiency by pads in p+Pb collision.

Figure 5 (left) shows a π^0 detection efficiency by pads in p+p collision. Filled and open ones show S/N for minimum bias and jet process, respectively. Figure 5 (right) shows a π^0 detection efficiency by pads in p+Pb collision. Circles, squares and triangles show S/N for impact parameter with 0-3 fm, 3-6 fm and 6-9 fm, respectively. Efficiencies except p+p jet-process are about more than 50%. Jet-process efficiency is very small maybe due to the high local multiplicity.

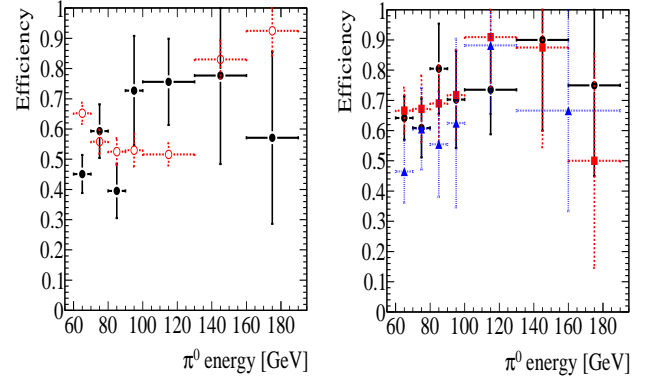


Figure 6. Left: π^0 detection efficiency in p+p collision. Right: π^0 detection efficiency in p+Pb collision.

Finally, there is a π^0 detection efficiency by strips. Figure 6 (left) shows an efficiency in p+p collision. Filled and open ones show efficiencies for minimum bias and jet process, respectively. Figure 6 (right) shows an efficiency in p+Pb collision. Circles, squares and triangles show efficiencies by strips for impact parameter of 0-3 fm, 3-6 fm and 6-9 fm, respectively. Efficiencies using strip are unchanged by process.

4. Summary and Outlook

FOCAL has been proposed as a LHC-ALICE upgrade designed for the measurement of π^0 and direct γ at forward rapidity in order to study the gluon PDF in proton and nuclei at small- x . FOCAL is silicon and tungsten sampling calorimeter. We evaluated FOCAL performance of π^0 reconstruction in p+p and p+Pb collisions. π^0 detection efficiency is unchanged by background from secondary particles. π^0 detection efficiencies by pads are 60% in p+p collision at minimum bias and p+Pb collision respectively. π^0 detection efficiencies by strips are 60% in all collision. To evaluate FOCAL performance and π^0 reconstruction in Pb+Pb collision will be done.

References

- [1] E. Inauch, R. Venugopalan, hep-ph/0303204
- [2] I. Arsene *et al.*, for the BRAHMS collaboration, Phys. Rev. Lett **93** (2004) 242303.

ASIC development for ALICE FOCAL readout

S. Hayashi, H. Hamagaki, T. Gunji, Y. Hori, M. Tanaka^a, M. Kurokawa^b, Y. Katayose^c, and H. Ikeda^d,

Center for Nuclear Study, Graduate School of Science, University of Tokyo

^aHigh Energy Accelerator Research Organization, KEK, Open-It

^bRIKEN (The Institute of Physical and Chemical Research)

^cYokohama National University

^dJapan Aerospace Exploration Agency, JAXA

1. Introduction

As one of the upgrade plans for the ALICE detector, an Electromagnetic Calorimeter at a forward rapidity region (FOCAL) plans to be installed for study of a gluon distribution function at the small Bjorken x region ($10^{-4} < x < 10^{-3}$) in a proton and a nucleus, where a gluon saturation effect such as Color Glass Condensate (CGC) occurs, through measurements of direct photons and π^0 .

FOCAL is composed of 3 longitudinal segments consisting of 7 layers of W absorbers and Si pads. FOCAL is required to have a wide dynamic range (MIP - 200 GeV γ) and a separation capability for two photons from π^0 decays to measure direct photons and π^0 separately. Electromagnetic showers are easily separated due to a small Moliere radius of W (~ 9.3 mm). Si strip layers are additionally put in the first segment to realize high position resolution (~ 0.25 mm) as shown in Fig. 1. The details of the detector design

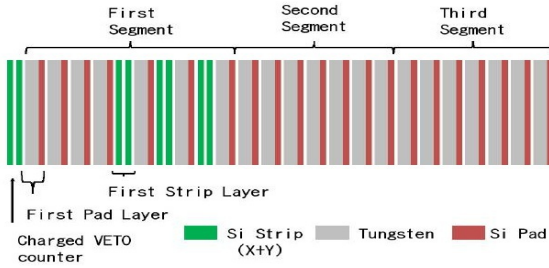


Figure 1. Longitudinal structure of FOCAL module

and basic features are reported in Ref. [1, 2]. Signals from the Si pads are summed up at each segment and the signal sums are input to readout circuits. The readout circuit must cover a wide dynamic range about 10^4 because an input charge range is from 50 fC to 200 pC. The readout circuit also has to fulfill some requirements. To reconstruct electromagnetic showers properly, a cross-talk between channels should be less than 1%. Signal to Noise ratio must be 10 for MIP. A pulse shaping time should be shorter than 800 ns in order to generate ALICE Level0 (L0) trigger signals.

Furthermore the total number of FOCAL channels is about 25000. Thus, ASIC has been developed to control such a large number of channels collectively. In this report, we show the current status of development of ASIC for the FOCAL front-end circuits.

2. Design of DGCSA

We propose a dual-gain system consisting of two charge sensitive preamplifiers (DGCSA), which fulfills the require-

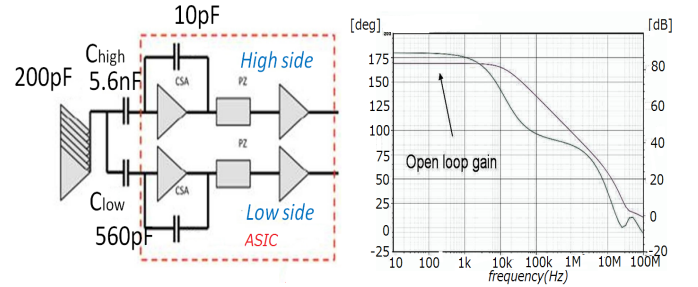


Figure 2. Left: Schematic of DGCSA, Right: Dependence on frequency of open loop gain and phase of amplifier

ment of a wide dynamic range of 10^4 . The left panel of Fig. 2 shows a schematic of DGCSA [3]. The ratio of input impedances between high gain side coupled C_{high} and low gain side coupled to C_{low} as shown Fig. 2 is expressed as

$$\frac{Z_{high}}{Z_{low}} = \frac{1/sC_{high} + z/A}{1/sC_{low} + z/A}, \quad (1)$$

where s is a variable of Laplace transformation and z is an impedance of feedback elements. A is an open loop gain of the preamplifier. If an open loop gain is large enough compared to z/A , an input impedance simply depends on a coupling capacitor. Therefore an input charge can be divided asymmetrically in proportion to the ratio of input impedances, and the divided fraction of the charge is given by a ratio of two coupling capacitors. The designed ratio is 10, *i.e.* $C_{high}/C_{low} = 5.6 \text{ nF}/560 \text{ pF}$. The decay constant is 80 μs due to the feedback capacitor C_f of 10 pF. Small (50 fC \sim 10 pC) and large (10 \sim 200 pC) signals are selectively read out in the high and low gain sides, respectively.

The preamplifier has folded cascade and source follower stages. As shown in the right panel of Fig. 2, an open loop gain reaches 82 dB due to a large drain current, and then connects to a current source as an effective resistance.

It is also important to prevent from saturation and reduction of a dynamic range. If saturation occurs in the high gain side, an input impedance in the high gain side becomes very large. Consequently, almost all charges flow to the low gain side. Consequently, reduction of the dynamic range occurs. To prevent this situation, a NMOS switching circuit is connected in the high gain side. If an output value exceeds the threshold value, NMOS turns on and absorbs charge. Therefore the saturation is prevented.

Figure 3 shows transients of a preamp output in the high (left) and low (right) gain sides. A spike can be seen in

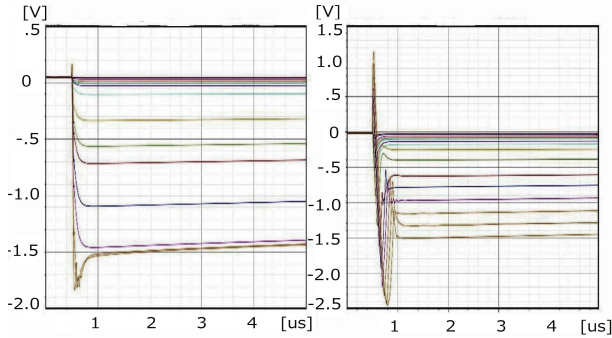


Figure 3. Left: Transient of preamp output in high gain side (An input charge is from 50fC to 10pC), Right: Transient of preamp output in low gain side (An input charge is from 1pC to 200pC)

the low gain side. This spike results from a phase gap between the high and low gain sides. If z/A in Eq. 1 can not be negligible due to a too fast signal, a real part of an input impedance becomes dominant. The same amount of an input charge flow into both sides. This makes a spike in the low gain side. Thus, a shaping time should be long enough (a few μs) to cancel out the fast component of a signal.

A linearity with a shaping time of 2 μs is also checked using a circuit simulator HSPICE. Results of the high and low gain sides are shown in Fig. 4. The dynamic ranges of the high and low gain sides can reach up to 200 pC. Finally, the DGCSA ASIC was fabricated with the 0.5 μm CMOS process of Taiwan Semiconductor Manufacturing Company (TSMC).

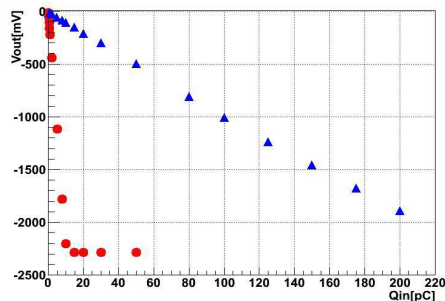


Figure 4. Output voltage of shaping amplifier at each gain side

3. QTC fabrication

Charge-to-Time converter (QTC) has been also developed. QTC is a kind of sample and hold circuits, and a time width as a QTC output corresponds to an input pulse height. Figure. 5 shows the transient behavior of QTC with five switches. An input pulse is sampled by a 5 pF sampling capacitor with switch1 on. Then, ramp-up starts with a 25 μA current source after holding of a peak value with switch1 off. Then, if an output of sample and hold circuit exceeds the threshold of a comparator, a duration of ramping defined as QTC time is output from QTC. One of advantages of QTC is release from reduction of the resolution by ADC. Because output is digital signal, noise tolerance and management of cable driving for output is better than analog output. The QTC with 5 switches connected to DGCSA was designed. A linearity of QTC is checked with HSPICE.

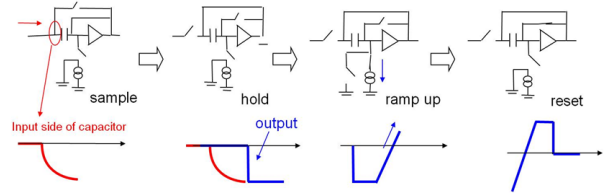


Figure 5. Schematic and operational order of QTC

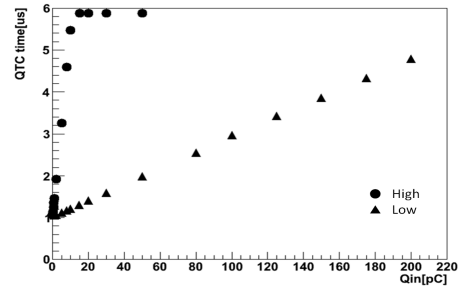


Figure 6. Linearity of QTC in each gain side

Results of the high and low gain sides are shown in Fig. 6. The dynamic ranges of the high and low gain sides can reach to 10pC and 200 pC, respectively. Finally, QTC with DGCSA ASIC was fabricated with the 0.5 μm CMOS process of TSMC.

4. The problem of DGCSA and solution

FOCAL needs to generate the L0 trigger signal within 800 ns from collisions, then a shaping time is required less than 800 ns. It conflicts with the DGCSA requirement on its shaping time of a few μs , as already described. A current amplifier with a current conveyor is one of alternatives to DGCSA. Current conveyor is composed of input and mirror stages. It has good time reaction and, a shorter shaping time can be realized compared to DGCSA.

5. Summary and outlook

FOCAL is proposed as one of the upgrade plans for ALICE to study small-x physics in a proton and a nucleus at LHC energy. The readout circuit for FOCAL must have a wide dynamic range $\sim 10^4$. We designed DGCSA and QTC as a candidate of the readout circuit. It was confirmed by simulations that DGCSA and QTC fulfill the requirements for the FOCAL readout and we fabricated their prototype ASIC by a 0.5 μm process. In future, a new readout circuit needs to be developed to fulfill the requirement for L0 trigger generation.

References

- [1] Y. Hori *et al.*, CNS Ann. Rep. 2009 (2011)
- [2] T. Gunji *et al.*, CNS Ann. Rep. 2009 (2011)
- [3] M. Kurokawa *et al.*, RIKEN Accel. Prog. Rep., **43**, 182 (2010)

Measurement of J/ψ photoproduction in ultra-peripheral Au+Au collisions at $\sqrt{s_{NN}}=200\text{GeV}$ using the PHENIX detector

A Takahara, H Hamagaki, T Gunji, Zaida Conesa del Valle^a, Yasuyuki Akiba^b Mickey Chiu^e,
Joakim Nystrand^d, Sebastian White^e, Kyrre Skjerdal^d, Ermias T. Atomssa^c

Center for Nuclear Study, Graduate School of Science, University of Tokyo

^aCERN

^bRIKEN BNL Center

^cStony Brook University

^dDepartment of Physics, Lund University

^eBrookhaven National Laboratory

1. Introduction

We present measurements of the photoproduction of the J/ψ photoproduction in ultra-peripheral nucleus-nucleus interactions of Au nuclei at $\sqrt{s_{NN}} = 200$ GeV at RHIC. An Ultra-Peripheral Collision (UPC) is referred to a collision in which an impact parameter is greater than the sum of nuclear radii. UPC has attracted considerable interests at hadron colliders in recent years [1–3]. UPC can be used for determining gluon density in nuclei at small Bjorken x . Measurements of $J/\psi \rightarrow e^+e^-$ at mid-rapidity and $J/\psi \rightarrow \mu^+\mu^-$ at forward-rapidity have been performed using data of Year-2007 and 2010 Au+Au collisions taken by PHENIX, respectively. The current status of $J/\psi \rightarrow e^+e^-, \mu^+\mu^-$ measurements are presented in this report.

2. Data analysis

The definition of UPC trigger are "Zero degree calorimeter detects at least one spectator neutron", "Beam Beam counter, which usually detects secondary charged particles, doesn't detect anything", and "Energy deposition in the ElectroMagnetic Calorimeter is larger than 1 GeV." or "at least 2 tracks reach MUID gap2(for $\mu^+\mu^-$)"

2.1. e^+e^- analysis

In addition to the trigger described above, it is required that there are only two electron tracks in the PHENIX central arms for $J/\psi \rightarrow e^+e^-$ analysis.

The J/ψ cross section in a given rapidity as a function of p_T is given by,

$$\frac{1}{2\pi p_T dp_T dy} \times \frac{B_{ee} d^2\sigma_{J/\psi}}{2\pi p_T dp_T dy} = \frac{N_{J/\psi}}{(\epsilon_{Acc} \cdot \epsilon_{reco} \cdot \epsilon_{cuts}) \cdot \epsilon_{trigger} \cdot \mathcal{L}_{int}} \quad (1)$$

where B_{ee} is the $J/\psi \rightarrow e^+e^-$ branching ratio, $N_{J/\psi}$ is the number of J/ψ . Figure 1 shows the number of measured J/ψ as a function of p_T . \mathcal{L}_{int} is the integrated luminosity of $527.45 \pm 23 \mu\text{b}^{-1}$, ϵ_{acc} is the acceptance of detectors for $J/\psi \rightarrow e^+e^-$. ϵ_{reco} is efficiency of reconstruction. ϵ_{cuts} is the cuts applied to identify electron or positron.

To evaluate $\epsilon_{acc} \cdot \epsilon_{reco} \cdot \epsilon_{cuts}$, about 2M J/ψ events with flat p_T (0-2.5 GeV/c) were generated. In this simulation, 2 cases of the J/ψ polarization, full transverse polarized and non-polarized, were studied.

There are two types of J/ψ production in UPC, where one is the coherent J/ψ production ($g + A \rightarrow J/\psi + X$) and the other is incoherent process ($g + n \rightarrow J/\psi + X$). Coherent J/ψ 's are concentrated at very low p_T , and due to spin conservation and γ full transverse polarization of g , J/ψ should be full transverse polarized. Incoherent UPC J/ψ 's can be distributed in a wide p_T range, and the spin polarization is not clear. For $p_T < 0.4$ GeV/c, because coherent production should be dominant at the p_T region, only transverse polarized simulation data are used for $\epsilon_{acc} \cdot \epsilon_{reco} \cdot \epsilon_{cuts}$ determination. For $p_T > 0.4$ GeV/c, because incoherent production should be dominant at the p_T region and polarization isn't clear. transverse full polarized and non polarized case $\epsilon_{acc} \cdot \epsilon_{reco} \cdot \epsilon_{cuts}$ is extracted by taking the average between the values obtained by full transverse polarization and no polarization. The difference in the values is taken into account as the systematic uncertainty. Figure 2 shows p_T de-

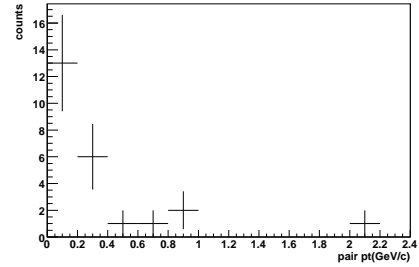


Figure 1. 2007 run central, p_T dependence of UPC J/ψ counts

pendence of $\epsilon_{Acc} \cdot \epsilon_{reco} \cdot \epsilon_{cuts}$.

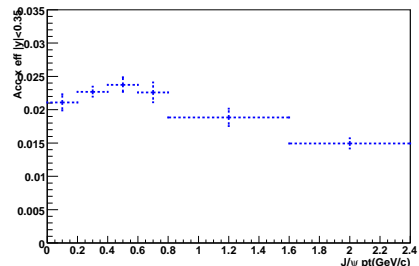


Figure 2. 2007 run central, p_T dependence of UPC $\epsilon_{Acc} \cdot \epsilon_{reco} \cdot \epsilon_{cuts}$.

$\epsilon_{trigger}$ is $\epsilon_{VETO_{BBC}} \cdot \epsilon_{ZDC} \cdot \epsilon_{EMCAL} \cdot \epsilon_{VETO_{BBC}} \cdot \epsilon_{ZDC}$ can be treated always nearly equal 1. Trigger efficiency of EMCAL

for $J/\psi \rightarrow e^+e^-$, ε_{EMCAL} , has p_T dependence. Here, ε_{EMCAL} is defined as $1 - (1 - \varepsilon_{EMCALfortrack1})(1 - \varepsilon_{EMCALfortrack2})$. Where $\varepsilon_{EMCALfortrack}$ corresponds to the trigger efficiency for the single electron track.

PHENIX EMCAL has 8 sectors. Sector by sector EMCAL trigger efficiency was measured from electron tracks in real minimum bias data.

Correlation between ε_{EMCAL} and J/ψ p_T is shown in Fig. 3.

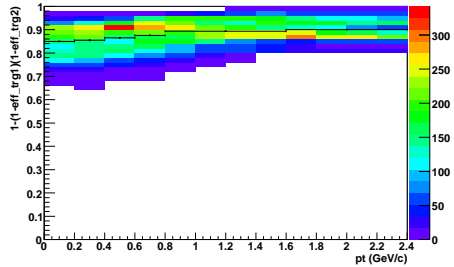


Figure 3. 2007 run central, p_T dependence of UPC $\varepsilon_{trigger}$

Figure 4 shows J/ψ $\frac{B_{ee}d^2\sigma_{J/\psi}}{2\pi p_T dp_T dy}$ distribution. J/ψ from coherent and incoherent process can be seen.

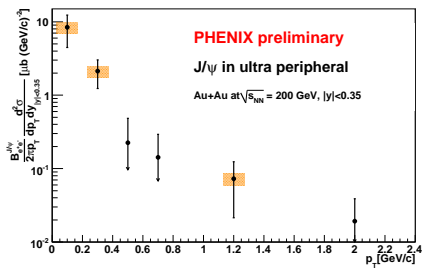


Figure 4. 2007 run central, J/ψ $\frac{B_{ee}d^2\sigma_{J/\psi}}{2\pi p_T dp_T dy}$

2.2. $\mu^+\mu^-$ analysis

Integrated luminosity of 2010 Au+Au collisions is 2 times larger than that of 2007 Au+Au collisions.

Detection of neutrons in both south ZDC and north ZDC is required to determine the collision vertex along the beam axis. The offline cut was applied to select the events which have two tracks in muon arm (forward rapidity) and no tracks in central arm.

Fig. 5 shows invariant mass plot of muon pairs in north and south muon arm. Very clear J/ψ peak was observed. Fig. 6 shows the number of measured J/ψ as a function of p_T . Coherent signal should have very low p_T peak. Even if the smearing effect due to the momentum resolution is taken into account, the region which has p_T greater than 0.5 GeV/c, should be pure incoherent. Both theoretical calculations [6] [7] expect incoherent dominant at forward rapidity.

3. Summary and Outlook

UPC data taken in 2007 and 2010 by PHENIX were analyzed.

The p_T dependence of the UPC J/ψ cross-section was extracted for mid-rapidity. Both coherent and incoherent process can be seen. For forward-rapidity, the analysis was

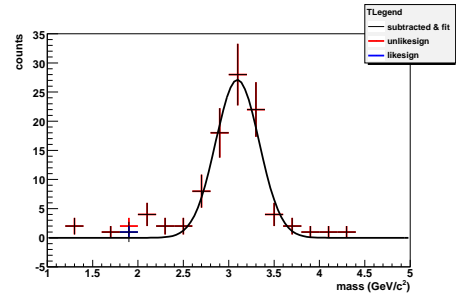


Figure 5. PHENIX 2010 RUN UPC J/ψ mass distribution (North case)

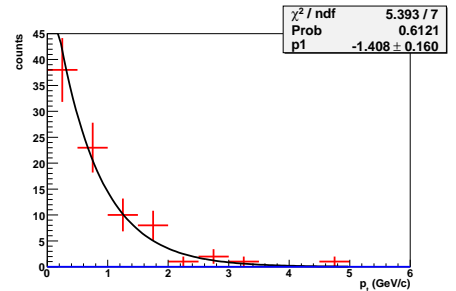


Figure 6. PHENIX 2010 RUN UPC J/ψ p_T distribution (North case)

not finished yet but 2010 forward rapidity total cross section and $\frac{B_{\mu\mu}d^2\sigma_{J/\psi}}{2\pi p_T dp_T dy}$ distribution will be analyzed soon.

References

- [1] G. Baur, K. Hencken, D. Trautmann, S. Sadovsky, and Y. Kharlov: Phys. Rep. B, **359**, (2002).
- [2] C. A. Bertulani, and S. R. Klein, J. Nystrand, Ann. Rev. Nucl. Part. Sci. B, **271**, (2005).
- [3] A. Baltz et al.: Phys. Rep. B **171**, (2008).
- [4] S. Afanasiev PHENIX Collaboration: Phys. Lett. B, **321**,(2009).
- [5] K. T. R. Davies and J. R. Nix: Phys. Rev. B 1977 (1976).
- [6] M. Strikman, M. Tverskoy and M. Zhalov, Phys. Lett. B 626 **72** (2005)
- [7] Yu. P. Ivanov, B. Z. Kopeliovich and I. Schmidt, arXiv:0706.1532 (2007).

Accelerator and Instrumentation

SHARAQ Project — Progress in FY2010 —

S. Michimasa, T. Uesaka^a, S. Ota, Y. Sasamoto, K. Miki^b, S. Noji, H. Matsubara, H. Miya, H. Tokieda, S. Kasase, Y. Kikuchi, S. Sasano^c, H. Kurei, T. Kawabata^d, K. Yakou^e, N. Yamazaki, A. Yoshino, S. Shimoura, H. Sakai^a, T. Kubo^a, Y. Yanagisawa^a, H. Baba^a, G.P. Berg^f, P. Roussel-Chomaz^g, D. Bazin^c, for the SHARAQ collaboration.

Center for Nuclear Study, Graduate School of Science, University of Tokyo

^a*RIKEN Nishina Center*

^b*RCNP, Osaka University*

^c*NSCL, Michigan State University*

^d*Department of Physics, Kyoto University*

^e*Department of Physics, University of Tokyo*

^f*Department of Physics, Notre Dame University*

^g*CEA Saclay*

The progress of SHARAQ project in the fiscal year 2010 is reviewed in this article. We have performed two physics runs with the SHARAQ spectrometer [1] and the high-resolution beam line [2] in October 2010. We have also done several detector developments and ion optics studies for upcoming physics experiments.

1. Optics study and detector development for experiments in SHARAQ

Prior to the experiment, we have studied the high-rate capability of beamline detectors; LP-MWDC [3], and the plastic tracking detector [5]. To optimize the operating parameters for the LP-MWDC under the high-irradiation condition, we performed irradiation test by using the Pelletron beamline at RIKEN. The MWDCs were confirmed to be stably operational under intense beam of 2×10^6 particle/sec and operated stably through the experiment. The detail is described in Ref. [4]. Plastic tracking detector is developed for beam tracking under the high-rate and high-dense condition such as an achromatic focus. The details of the tracker is described in Ref. [5]. In the experiments in October, 2010, the tracking detector was installed at the F3 achromatic focus of BigRIPS, which is the starting point of beam transport of SHARAQ. Beam spot at F3 is approximately 3 mm in diameter and the beam rate reaches $\sim 10^6$ counts/sec/mm². The detector was also stable during the experiment. Combined with the LP-MWDC, RI beam tracking at F3 was successfully carried out.

In the optics study, we demonstrated dispersion-matching (DM) beam optics of RI beam for the first time. The momentum-independent tuning method [6] efficiently worked at momentum-dispersive foci. The DM focus condition was achieved against beams with wide momentum spread. Conclusively we achieved the momentum resolution of approximately 1/5000. Further studies of improve the momentum resolution are in progress.

For upcoming experiments in SHARAQ, we started mainly two development projects. First, we studied two tracking capability of SHARAQ final focal plane system, which consists of Cathode-Readout Drift Chambers (CRDCs) and a three-layer plastic scintillator hodoscope

[7]. To track two particles by this system, we needed to create two strobe triggers for CRDCs, because the hit timings of two particles are different. We built a trigger logic circuit in FPGA module, and demonstrated the two particle tracking. Details on the logic of the circuit are shown in Ref. [8].

Second, we developed the CVD diamond detector which has extremely good timing resolution. The detector is expected to improve the resolution of time-of-flight very much. To examine the response of a CVD diamond detector, we did an irradiation study by using α particles at 32 MeV in January 2011, and we estimated detection efficiency and timing resolution of the detector. Detail is reported in Ref. [9]. Consequently CVD diamond detector has better than the timing resolution of 30 ps. To put this performance to good use, we plan to measure of nuclear masses of short-lived nuclei far from stability, combined the high-B ρ -resolution performance of the SHARAQ spectrometer. This timing resolution is estimated to achieve the mass resolution of 1/4000 atomic mass unit.

2. Physics runs: (¹⁰C, ¹⁰B($T = 1$)) and (¹²N, ¹²C) experiments

Two physics programs on Isovector-type responses in nuclei with the SHARAQ spectrometer were performed in October 2010. Each program is characterized by its reaction selectivity of the RI-induced reaction: The (¹⁰C, ¹⁰B($T = 1$)) reaction is a probe of $\Delta T = 1$, $\Delta S = 0$ mode, which is considered to be sensitive to Isovector spin-non-flip monopole transition in nuclei, and the (¹²N, ¹²C) reaction is a probe of $\Delta T = 1$, $\Delta S = 1$ mode with largely positive Q value, which is considered to be sensitive to Isovector spin monopole transition in nuclei. In these experiments, we adopted dispersion-matched RI beams of ¹⁰C and ¹²N and analyzed the momenta of ejectiles from ⁷Li and ⁹⁰Zr targets with the SHARAQ spectrometer. Details of these experiments are described in Refs [10, 11]

References

- [1] T. Uesaka *et al.*, Nucl. Instrum. Methods B **266** (2008) 4218.

- [2] T. Kawabata *et al.*, Nucl. Instrum. Methods B **266** (2008) 4201.
- [3] H. Miya *et al.*, CNS Ann. Rep. 2010 (2012).
- [4] S. Noji *et al.*, CNS Ann. Rep. 2010 (2012).
- [5] Y. Kikuchi *et al.*, CNS Ann. Rep. 2010 (2012).
- [6] Y. Sasamoto *et al.*, CNS Ann. Rep. 2010 (2012).
- [7] S. Michimasa *et al.*, CNS Ann. Rep. 2009 (2012) 37, and references therein.
- [8] K. Kisamori *et al.*, CNS Ann. Rep. 2010 (2012).
- [9] S. Michimasa *et al.*, CNS Ann. Rep. 2010 (2012).
- [10] Y. Sasamoto *et al.*, CNS Ann. Rep. 2010 (2012).
- [11] S. Noji *et al.*, CNS Ann. Rep. 2010 (2012).

Development of CVD Diamond Detector

S. Michimasa, M. Takaki, M. Dozono^a, S. Go, E. Ideguchi, K. Kisamori, H. Matsubara, H. Miya, S. Ota, H. Sakai^a, S. Shimoura, A. Stolz^b, Tsz Leung Tang, H. Tokieda, T. Uesaka^a, R.G.T. Zegers^b

Center for Nuclear Study, Graduate School of Science, University of Tokyo

^aRIKEN Nishina Center

^bNSCL, Michigan State University

The diamond is an attractive material for a radiation detector, and has actually a long history in radiation applications. However, the use of diamond detector was restricted owing to price and size of the natural materials. The chemical vapor deposition (CVD) technique [1–3] has made it possible to create the high-quality diamond material with applicable size, and has provided opportunities of practical use of diamond radiation detectors [4].

The properties of diamond are shown in Table 1, together with those of silicon for comparison. The large displacement energy of diamond indicates its inherent radiation hardness. Its small dielectric constant and large band gap result in low detector capacitance and low leakage current, and thus low-noise level is expected. Its large mobility and saturation velocity of charge carriers promise very good timing resolution of signal responses, combined with a large breakdown field.

Physics properties at 300 K	Diamond	Silicon
Band gap (eV)	5.5	1.12
Breakdown field (V/m)	10^7	3×10^5
Resistivity (Ω cm)	$> 10^{11}$	2.3×10^5
Electron mobility ($\text{cm}^2/\text{V/s}$)	1800	1500
Hole mobility ($\text{cm}^2/\text{V/s}$)	1200	600
Saturation velocity (km/s)	220	82
Dielectric constant	5.7	11.9
Displacement Energy (eV/atom)	43	13-20
Energy to create an e - h pair (eV)	13	3.6
Thermal conductivity (W/cm/K)	20	1.27
Lattice constant (\AA)	3.57	5.43

Table 1. Properties of the diamond and the silicon.

Based on the outstanding properties of diamond, we aim at developing a CVD diamond detector as a thin and large-area counter with extremely good timing resolution. The detector development has been performed by the collaboration of CNS and NSCL.

In FY2010, we manufactured a diamond detector with striped cathodes. Its photograph and cathode design are illustrated in Fig. 1. The cathode has multi-layer structure of 10-nm nickel and 100-nm gold. The nickel layer is important for the ohmic contact between a diamond and a gold layer. The material is polycrystalline CVD (pCVD) diamond crystal. Its size and thickness are $30 \times 30 \text{ mm}^2$ and 0.2 mm, respectively. The cathode is $28 \times 28 \text{ mm}^2$. The detector has one pad on one side (Side A), and 4 strips the other side (Side B). On Side A, 4 readout wires are bonded to the corners. On Side B, 2 readout wires are bonded to the

both edges of each strip. The four strips are 9 mm, 5 mm, 5 mm, 9 mm in width, respectively, since the center strips receive higher beam rate. Totally a detector has 12 readouts in order to deduce hit position and timing. SMA connectors are used to reduce signal strength loss in a radio frequency region ($\sim 10 \text{ GHz}$). In operation, 400 cols was applied to the pad (Side A).

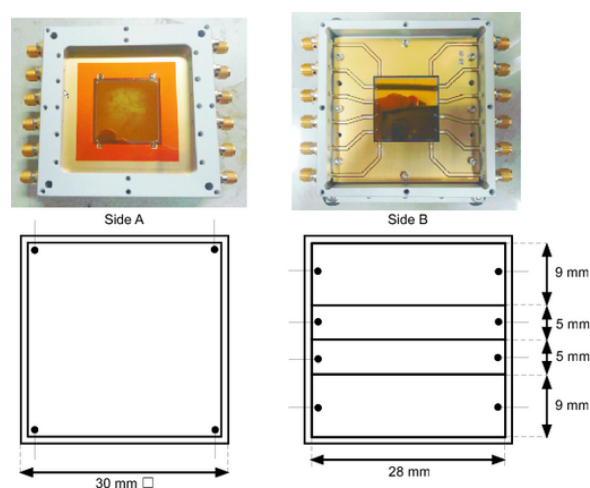


Figure 1. Photographs and cathode pattern of a manufactured diamond detector.

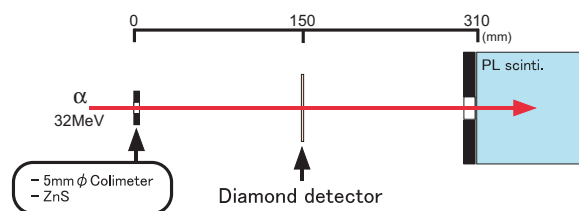


Figure 2. Detector setup of irradiation experiment by α beam.

To examine basic performance of the detector, we have performed an irradiation experiment in 2011. The experimental setup is shown in Fig. 2. The setup was placed in the E7b course in RIKEN accelerator facility, and α beam at 32 MeV was used. Beam intensity was controlled to be approximately 1000 counts/sec and beam spot size was typically 1 cm diameter at the diamond detector.

For signal processing from the diamond detector RF preamplifiers were connected to its readouts. Figure 3 is a snapshot showing the outputs: Yellow line shows from Side A; cyan and magenta lines show signals from edges of 1 strip on Side B, respectively. A typical signal has rise time of 0.7 ns and decay time of 10 ns. In the experiment, we obtained charge information and time-of-flight (TOF) between a diamond detector and plastic scintillator. The TOF

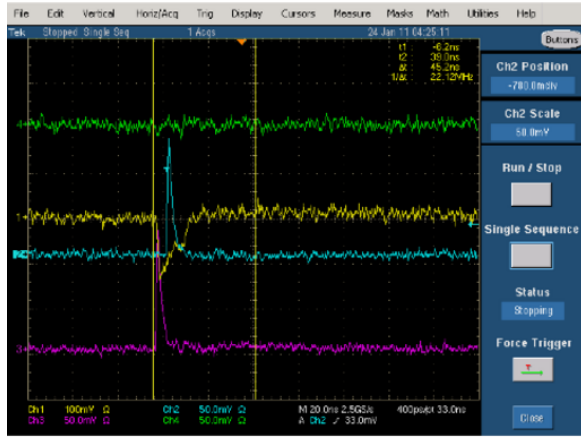


Figure 3. Snapshot of oscilloscope showing the outputs: Yellow line shows from Side A; cyan and magenta lines show from edges of 1 strip on Side B, respectively.

was measured by using TAC and 13-bit ADC modules. The timing resolution of this system was estimated to be 6.5 ps by measuring constant time difference created by a pulser signal.

To estimate detection efficiency of the diamond detector, we checked the coincidence ratio of signals from the diamond detector and from the plastic scintillator. We deduced the detection efficiency of the diamond detector to be almost 100% for 32-MeV α particles. The energy deposit in the diamond detector corresponds to that of 320A-MeV ^{12}N isotopes. The diamond detector is therefore usable for intermediate-energy RI beams.

We analyzed charge distributions of the pulse signal from the pad (Side A) to estimate the collection depth of a pCVD crystal. The collection depth is an indication of how much charge carriers is lost by unconformity of diamond crystal. Deduced correction depth is $\sim 190 \mu\text{m}$ and is comparable to the physical thickness of $200 \mu\text{m}$. Thus the carrier loss in diamond is considered to be very small.

To deduce timing resolution of diamond detector, we made a spectrum of time difference between signal pulses from both edges of a strip of diamond detector, shown in Fig. 4. The width of the spectrum indicates $\sqrt{2}$ times of the timing resolution under a condition of extremely small beam spot size. Actually beam spot size on diamond detector is estimated to be $\sim 1 \text{ cm}$, therefore the main part of the width is considered to originate from hit position dependence. However the upper limit of time resolution of this diamond detector is estimated to be 27 ps in one sigma.

We have started to manufacture the second diamond detector in FY2011, which has identical design with the first one. By using two detectors, we will be able to measure TOF with extremely good resolution. Combination with this detector and the high momentum resolution of SHARAQ spectrometer enables us to realize a unique experiment to measure precisely the mass of radioactive nuclei far from stability.

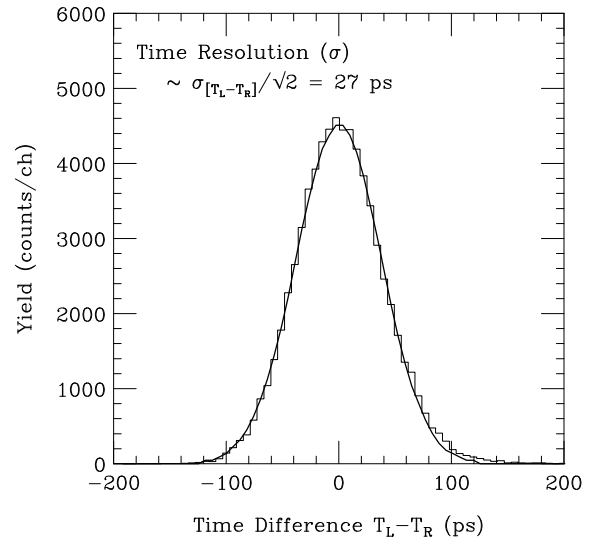


Figure 4. Time difference spectrum between both edges of a strip of the diamond detector. We deduce the time resolution to be 27 ps from the spectrum.

References

- [1] W.G. Eversole, U.S. Patent Nos. 3030187 and 3030188 (1958).
- [2] J.C. Angus, H.A. Will and W.S. Stanko, J. Appl. Phys. **39** (1968) 2915.
- [3] B.V. Deryaguin *et al.*, J. Cryst. Growth **2** (1968) 380.
- [4] The RD42 Collaboration, Nucl. Instr. and Meth. A **435** (1999) 194.

Focus tuning method of the high-resolution beam line for the SHARAQ spectrometer

Y. Sasamoto, T. Uesaka, T. Kubo^a, H. Takeda^a, and G.P.A. Berg^b

Center for Nuclear Study, Graduate School of Science, University of Tokyo

^aRIKEN Nishina center

^bDepartment of Physics and Joint Institute for Nuclear Astrophysics, University of Notre Dame

1. introduction

New missing mass spectroscopy with RI beams is planned at RI beam Factory (RIBF) with the SHARAQ spectrometer [1] in combination with a variety of radioactive beams from BigRIPS [2]. To avoid deterioration of energy resolution due to the momentum spread of RI beams, the dispersion matching (DM) technique is applied in high resolution measurements [3].

Figure 1 shows the layout of the high-resolution beam line. The RI beam produced at the production target at F0 is achromatically focused at F3 which is the ion-optical starting point of the high-resolution beam line. The beam line after F3 consists of more than 30 magnetic elements. While the initial settings for each magnets were determined from the ion optical calculation based on the precise magnetic field measurement [4], fine tuning is still needed for the high-resolution measurements. In this report, the tuning method which is applied to the high-resolution beam line for the SHARAQ spectrometer is described.

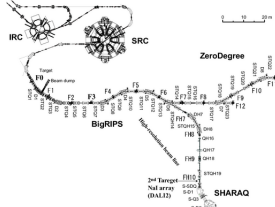


Figure 1. Layout of the high-resolution beam line. It branches from BigRIPS after F6. F3 is the ion-optical starting point of the high-resolution beam line.

2. Focus tuning at the focal planes with low dispersion

Our beam tuning is based on the particle trajectories measured by using the tracking detectors. This enable us to deduce the elements of the transfer matrix R directly, which connects the initial and final coordinate vectors X and X' as $X' = RX$ in the first-order optics.

The practical way to transport the beam as designed is to achieve the focus condition at each focal plane. Phase-space variables in the first-order optics between the initial and the final plane is described as

$$x_f = (x|x)_{if}x_i + (x|\delta)_{if}\delta + (x|a)_{if}a_i, \quad (1)$$

where the each digit in the subscript means the initial and final focal plane. To examine the focus condition $(x|a)_{if} = 0$, the correlation between the position x_f and the angle a_i is to be examined. In the case of the focal planes where $(x|\delta)$

and $(a|\delta)$ are not large, the angle of the final focal plane a_f can be used as a substitute for a_i in the focus tuning. Since both of $(x|\delta)$ and $(a|\delta)$ are large at some focal planes in the high resolution beamline to achieve dispersion matched condition, we use the angle a_i at the initial plane.

In the correlation of x_f and a_i , the slope of the plot corresponds to the magnitude of $(x|a)_{if}$. In this report, we call this method, which involves the use of the correlation between x_f and a_i directly, the standard focus tuning method. Actually, the standard focus tuning method is used for the beam tuning of the high-resolution beam line between F3 and F4 shown in Fig. 1, where the ion-optical dispersion is not so large. The correlation of the positions at F4 with the angles at F3 can be used as shown in Fig. 2.

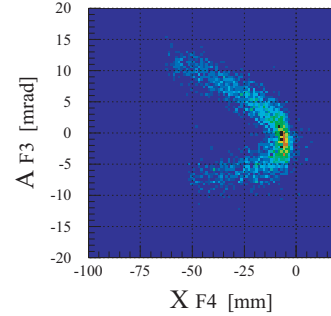


Figure 2. The correlation between F3 and F4, whose slope corresponds to $(x|a)_{34}$.

3. Focus tuning at the largely dispersive focal planes

In transporting RI beams with large momentum spread in beam line with large dispersion, the standard tuning method is not always effective. Upper panel of Fig. 3 shows the correlation of the angle at F3 with the position at FH7 with the secondary ^{10}C beam using the standard focus tuning method. The position and angle are determined experimentally by using multiwire drift chambers [5]. The upper-three figures in Fig. 3 were obtained at different magnetic-field settings. Therefore, the slopes in the panels should be different. However, it is difficult to identify the difference.

The difficulty is caused by the spread of the image at the focal plane due to the large dispersion and beam energy spread. The dispersion at the focal planes in the DM mode are summarized in Table 1. When the primary beam with the momentum spread of $\Delta p \sim \pm 0.1\%$ is used, the horizontal beam image, for example, at FH7, spreads by about ± 8 mm due to the dispersion. The beam spread smears in-

formation about $(x|a)$. Even if momentum slits are used to reduce the beam momentum, the reduced momentum is almost the same order of the primary beam. The standard tuning method could be applied between F3 and F4 as described above because the spread caused by the dispersion is not considerably larger than that at other points.

Table 1. Design dispersion $(x|\delta)$ for the DM mode.

Focal plane	F4	F6	FH7	FH9	FH10
Design value	-19	76.7	-73.7	229	150
(mm/%)					

3.1. Momentum independent focus tuning method

Tuning method, which we introduce, is to use quantities which do not depend on the beam momentum. In this report, we call this method the momentum independent tuning method. This method is effective for the tuning in the focal planes which have the large dispersion.

In addition to the information at the initial and final plane, the information at an intermediate plane m between initial and final planes are needed to check the focus condition independent of beam momentum. The considerable equation in the first-order optics as

$$\begin{aligned} x_f &= (x|x)_{if}x_i + (x|a)_{if}a_i + (x|\delta)_{if}\delta \\ x_m &= (x|x)_{im}x_i + (x|\delta)_{im}\delta \end{aligned} \quad (2)$$

where $(x|a)_{im} = 0$ because the focus condition at the intermediate plane is tuned prior to the tuning at the final plane. Beam momentum δ is obtained from Eq. (2) as $\delta = \frac{x_m - (x|x)_{im}x_i}{(x|\delta)_{im}}$. Inserting the δ to Eq. (2) and subtract the dispersion term from x_f , we can obtain,

$$x_f - (x|\delta)_{if}\delta = x_f - (x|\delta)_{if} \frac{x_m - (x|x)_{im}x_i}{(x|\delta)_{im}} \quad (3)$$

$$= (x|x)_{if}x_i + (x|a)_{if}a_i. \quad (4)$$

Assuming that the magnification terms are negligible compared with dispersion terms, the equation of

$$x'_f = x_f - \frac{(x|\delta)_{if}}{(x|\delta)_{im}}x_m = (x|a)_{if}a_i \quad (5)$$

is deduced. x'_f is independent of the beam momentum by eliminating the spread due to the beam-energy spread using the intermediate focal plane m . With introduction of the correlation between x'_f and a_i , the focus condition $(x|a)_{if}$ is clearly seen as the slope in the correlation.

To evaluate the left-hand side term of Eq. (5), the $x_f - x_m$ correlation should be experimentally deduced from the correlation of x_i and x_f . By applying this method, the focus tuning at FH7, where the focus condition is difficult to see as shown in the upper panel of Fig. 3 due to the large dispersion, is possible as shown in the lower panel of Fig. 3.

4. Summary

For the focus tuning, the standard tuning method to use the correlation between x_f and a_i cannot be used in the

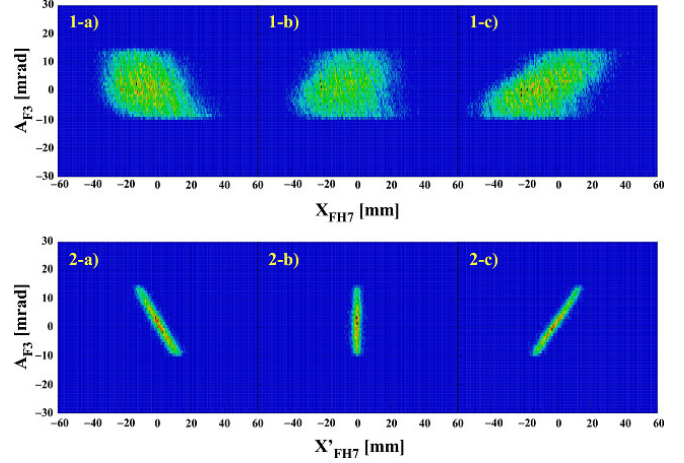


Figure 3. Correlation between the angles at F3 and x' at FH7 with secondary ^{10}C beam under different field settings. The slope corresponds to the magnitude of $(x|a)_{37}$.

largely dispersive focal planes. Accordingly we introduce the momentum independent focus tuning which is eliminating the spread due to the beam energy spread. With this method, the focus tuning in the largely dispersive focal planes was successfully verified. This is the expeditious tuning method because it doesn't require the complicated procedure. This method enables us to quickly optimize the magnetic settings of the high-resolution beam line for the SHARAQ spectrometer.

References

- [1] T. Uesaka et al.: Nucl. Instrum. Meth. in Phys. Res. B **266**, 4218 (2008).
- [2] T. Kubo et al.: Nucl. Instrum. and Meth. B **204**, 97 (2003).
- [3] T. Kawabata et al.: Nucl. Instrum. and Meth. in Phys. Res. B **266**, 4201 (2008).
- [4] H. Takeda et. al.: Private communication.
- [5] A. Saito et. al.: RIKEN Accel. Prog. Rep. **43**, 176 (2010).

Performance test of low-pressure multi-wire drift chambers for SHARAQ beamline with high-intensity proton beam at the Pelletron Accelerator at RIKEN

S. Noji¹, S. Ota^a, S. Kawase^a, Y. Kikuchi^a, K. Kisamori^a, M. Takaki^a, S. Michimasa^a, K. Miki², H. Miya^a

Department of Physics, University of Tokyo

^aCenter for Nuclear Study, Graduate School of Science, University of Tokyo

In October 2010, we performed a series of experiments at the SHARAQ Spectrometer to search the isovector spin-flip/spin-non-flip monopole resonances in ^{90}Nb by using the $^{90}\text{Zr}(^{12}\text{N}, ^{12}\text{C})^{90}\text{Nb}$ and $^{90}\text{Zr}(^{10}\text{C}, ^{10}\text{B}^*(\text{IAS}))^{90}\text{Nb}$ reactions at 200 MeV/nucleon [1, 2]. In these two experiments, it was necessary to determine angles of incoming particles at the target position with an accuracy of about 2 mrad in order to separate the monopole resonances ($\Delta L = 0$) from higher ΔL components with the information of the angular distributions of the cross sections.

For that purpose, the low-pressure multi-wire drift chambers (LP-MWDC's) [3] were planned to be used at the F-H10 focal plane of the high-resolution beam line. The counting rates of the incoming particles necessary for the physics experiments were about ≤ 2 Mcps. The spread of the beams at F-H10 were estimated to be ± 50 mm and ± 20 mm in x and y , respectively. This means that the rate for one cell, whose size is 9-mm, was as much as 500 kcps for the y plane. Since we did not have an experience to operate the LP-MWDC's at such high counting rates, therefore, in order to evaluate the efficiency and resolution under high counting rates, we decided to perform a test prior to the SHARAQ experiments.

We carried out the test experiment with the Pelletron tandem accelerator at the Nishina Center Development Building on the RIKEN campus in June, 2010. A hydrogen ion (H^+) beam extracted from a cesium sputter ion source was accelerated to 3 MeV by the Pelletron. We used this beam since the energy deposit of this beam to the detector was estimated to be comparable to that of the $^{12}\text{N}/^{10}\text{C}$ beams at 200 MeV/nucleon, with which we would run the physics experiments.

Figure 1 shows the setup of the experiment. A gold foil with a thickness of $2.5 \mu\text{m}$ was installed to spread out the incoming beam. A mylar window with a thickness of $25 \mu\text{m}$ was used to separate the vacuum region from the gas-filled region. The counter gas was isobutane ($i\text{-C}_4\text{H}_{10}$) at pressures of 15 and 20 kPa. A plastic scintillator with a size of 50×50 mm and a thickness of 5 mm was used as a trigger counter. The data were taken with the standard DAQ system for the LP-MWDC. The counting rates of the plastic scintillator and the cathode of the LP-MWDC were recorded.

The LP-MWDC worked stably under counting rates of 2.0(2.8) MHz for the plastic (cathode). The high voltages supplied were 1200–1350 V for 15 kPa, and 1400–1500 V

for 20 kPa. Analysis was done by following the standard procedure described in Ref. [3]. The detection efficiency was 100% under all the conditions described above. If the events with single hits for all the layers were selected, the position resolution was estimated to be $500 \mu\text{m}$. Events with multiple hits were not analysed for the present data.

In the physics runs in October, 2010, the LP-MWDC's at F-H10 stably worked for the ^{12}N and ^{10}C beams at 200 MeV/nucleon, which is described in Ref. [4].

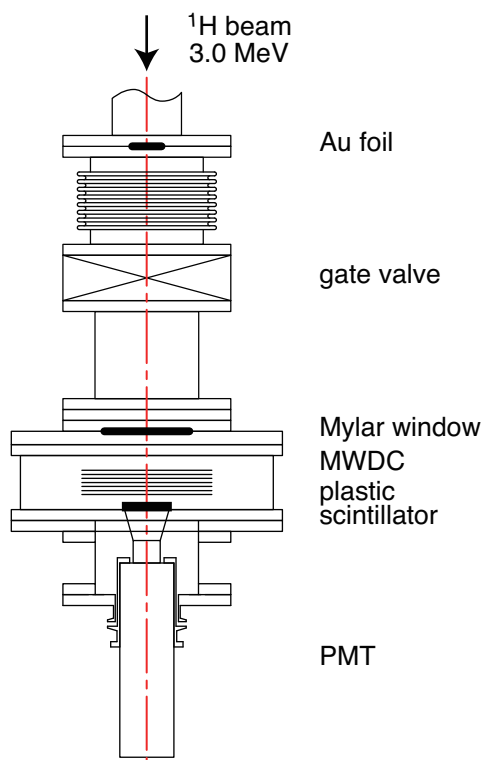


Figure 1. Schematic experimental setup.

Acknowledgement

The authors are thankful to the Pelletron accelerator staff for providing excellent quality beam for the test experiment.

References

- [1] S. Noji et al., CNS Ann. Rep. 2010 (2012).
- [2] Y. Sasamoto et al., CNS Ann. Rep. 2010 (2012).
- [3] H. Miya et al., CNS Ann. Rep. 2008 (2010), H. Miya et al., CNS Ann. Rep. 2009 (2011).
- [4] H. Miya et al., CNS Ann. Rep. 2010 (2012).

¹Present address: Center for Nuclear Study, Graduate School of Science, University of Tokyo.

²Present address: Research Center for Nuclear Physics, Osaka University.

Performance of Low-Pressure Multi-Wire Drift Chamber for High-Intensity Heavy Ion beam

H. Miya, S. Ota, H. Matsubara, S. Noji, Y. Kikuchi, K. Kisamori, M. Takaki, S. Michimasa, K. Miki^a, T. Uesaka^b, and S. Shimoura

Center for Nuclear Study, Graduate School of Science, University of Tokyo

^a*Research Center for Nuclear Physics, Osaka University*

^b*RIKEN (The institute of Physical and Chemical Research)*

We are developing Low-pressure Multiwire Drift Chambers (LP-MWDCs) for tracking heavy ion beam particles (mass number around 10; energy around 200 MeV/nucleon). The LP-MWDCs are used in BigRIPS and high-resolution beamline at the Radioactive Isotope Beam Factory (RIBF). The past development of the LP-MWDCs was reported elsewhere [1].

In high resolution nuclear spectroscopy experiments performed with SHARAQ spectrometer [2], a secondary target should be sufficiently thin so that the overall energy resolution is not deteriorated. This in turn requires the use of a high-intensity beam. RI beams at an intensity of 1–2 MHz are transported to the target in the actual experiments [3,4]. Although these experiments have been conducted under lateral and angular dispersion matching condition, the beam tracks on the target had to be measured at an angular resolution of 1 mrad (FWHM) to correct the angular spread of the RI beams. Tracking detectors are required to have a position resolution less than 350 μm in FWHM when the two detectors are installed at a distance of 500 mm from each other. The new LP-MWDCs were developed to achieve the position resolution at the intensity of 1–2 MHz. Here, we report the position resolution and tracking efficiency as a function of the beam intensity with ^{12}N at 200 MeV/nucleon.

The LP-MWDC consists of four cathode and three anode planes with wire operation ($X:0^\circ$, $U:30^\circ$, $V:-45^\circ$). By using the inclined wire planes, the counting rate per cell can be reduced for the beam with a narrow width on the vertical axis. The effective area and the cell size are $216 \times 144 \text{ mm}^2$ and $9 \times 9 \text{ mm}^2$, respectively. The counter gas is pure isobutane at the pressure of 10 kPa. The effect of multiple scattering can be diminished by operating the low pressure gas to reduce the material. The specifications of the LP-MWDCs are summaries in table 1.

The position resolution and the tracking efficiency were evaluated by using the ^{12}N beam at 200 MeV/nucleon with

the intensity of 1 kHz–1 MHz at the high-resolution beam-line. The two LP-MWDCs were installed at a distance of 500 mm from each other at the focal plane of F-H10. The LP-MWDCs were operated at -1 kV on the cathode planes. The signals from anode wires were amplified and discriminated by REPIC RPA-132. The leading edge timing and pulse width were used for the drift time and energy loss information [1]. The pulse width is the time difference between the leading and trailing edges across the threshold level for amplified signals. The pulse width is correlated with the pulse height. The timing informations were recorded by using CAEN V1190 multihit TDCs. Plastic scintillators of the thickness of 1 mm and 3 mm were placed at the focal planes of F-3 and F-H10, respectively. The scintillator at the focal plane of F-3 was used as a trigger counter. The time zero for the drift chamber was determined by the scintillator at the F-H10. The signals from the scintillators at F-3 and F-H10 were discriminated by Lecroy 623B and Iwatsu Charge-to-Time Converter Module [5, 6], respectively. The discriminated signals were stored with the TDCs.

Configuration	C-V(-45°)-C-U(30°)-C-X(0°)-C
Effective area	$216 \times 144 \text{ mm}^2$
Cell size	$9 \times 9 \text{ mm}^2$
Channels	24 ch (AX), 24 ch (AU), 16 ch (AV)
Anode wire	Au-W, $20 \mu\text{m}^\phi$
Potential wire	Cu-W, $75 \mu\text{m}^\phi$
Cathode foil	Al-Mylar, $1.5 \mu\text{m}$
Detector gas	pure isobutane, 10 kPa

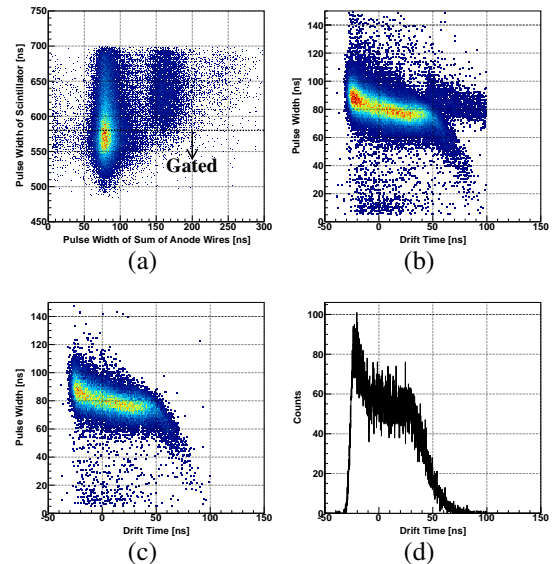


Figure 1. (a) Contour plot of the pulse width of the scintillator at F-H10 and the sum of pulse width of the anode wires. (b), (c) Contour plots of the pulse width and drift time without and with the gate on the pulse width of the scintillator, and (d) the drift time distribution with the gate at 10 kPa and -1 kV.

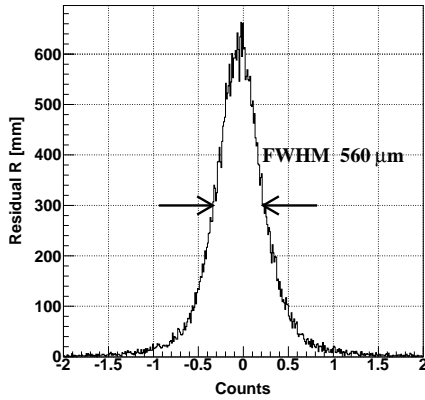


Figure 2. Residual distribution of $U_U - U_{XV}$ at the gas pressure and applied voltage of 10 kPa and -1 kV. Position resolution was estimated to be 306 μm in FWHM.

When the beam intensity is high, an event which two heavy ion beam particles pass through the LP-MWDCs in one RF timing is a problem. In the analysis, the pile-up event was rejected by using the energy information of the scintillator. Figure 1 (a) shows a scatter plot between the pulse width of the scintillator at the focal plane of F-H10 and the sum of the pulse width over all the anode wires at the beam intensity of 1 MHz. The number of beam particles which pass through the detectors were count by summing the pulse width as the energy information. The peak of 160 ns in the sum of pulse width indicates a pile-up event. The pulse width of the scintillators are selected between 450 ns and 580 ns to analyze the event which one beams pass. Figure 1 (b) and (c) shows scatter plots between the pulse width and drift time without and with the gate on the pulse width of the scintillator, respectively. Figure 1 (d) shows the drift time with the gate on. The drift time-to-space relation was determined by this distribution.

In order to estimate the position resolution, the residual distribution of $U_U - U_{XV}$ was investigated. Here, U_U is a hit position in the U layer, and U_{XV} is a hit position along the U axis and is determined from the hit positions in layers X and V. The geometrical configuration of the planes helps in unambiguous determination of the hit position. Figure 2 shows the residual distribution of $U_U - U_{XV}$. Considering the error propagation, the position resolution is estimated to be about 300 μm in FWHM.

Figure 3 shows the position resolutions as a function of the beam intensity of ^{12}N at 10 kPa and -1 kV. The position resolution are between 250 and 300 μm (FWHM) for the beam intensity from 1 kHz to 1 MHz. The resolution is sufficient for the required performance.

Figure 4 shows tracking efficiencies as a function of the beam intensity. The tracking efficiency was defined as the ratio of the number of the events having the residual within 3σ to the counted number of the beams by using the scintillator at the downstream of the LP-MWDCs. The tracking efficiencies are typically about 90%, independent from the beam intensity.

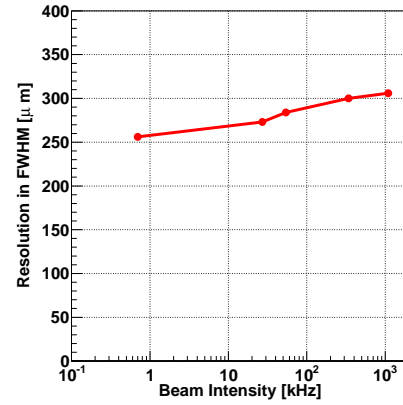


Figure 3. Position resolutions as a function of beam intensity of ^{12}N at the gas pressure and applied voltage of 10 kPa and -1 kV, respectively.

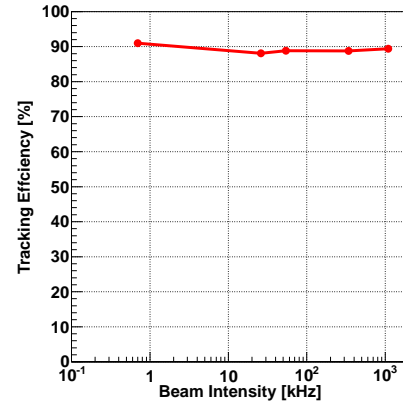


Figure 4. Tracking efficiencies as a function of beam intensity of ^{12}N at the gas pressure and applied of 10 kPa and -1 kV, respectively.

We have respectively developed the LP-MWDC as the tracking detector at the high resolution experiments for high intensity heavy ion beam. By using ^{12}N beam at the intensity between 1 kHz and 1 MHz, which is position resolution and tracking efficiency were evaluated. The position resolution was about 300 μm (FWHM) at the intensity of 1 MHz, the performance was sufficient for the requirement. The tracking efficiencies are typically 90% independent on the beam intensity.

References

- [1] H. Miya et al.: CNS Ann. Rep. 2009 (2011) 53.
- [2] T. Uesaka et al.: AIP Conf. Proc. **1235** (2010) 308.
- [3] Y. Sasamoto et al.: CNS Ann. Rep. 2010 (2012).
- [4] S. Noji et al.: CNS Ann. Rep. 2010 (2012).
- [5] S. Ota et al.: CNS Ann. Rep. 2009 (2011) 51.
- [6] S. Kawase et al.: CNS Ann. Rep. 2009 (2011) 55.

Development of two-alpha detection system in SHARAQ spectrometer for measurement of (^8He , ^8Be) reaction

K. Kisamori, S. Shimoura, S. Michimasa, S. Ota, S. Noji^a, A. Tokieda, H. Baba^b

Center for Nuclear Study, Graduate School of Science, University of Tokyo

^a*Department of Physics, University of Tokyo*

^b*RIKEN (The Institute of Physical and Chemical Research)*

1. Introduction

Multi-neutron systems in nuclei have attracted much attention both from experimental and theoretical point of view since candidates of bound tetra-neutron system were reported [1], [2].

We plan to measure a missing-mass spectrum for a tetra-neutron system produced by the double charge exchange reaction $^4\text{He}(^8\text{He}, ^8\text{Be})4n$. Small momentum transfer is achieved by the exothermic nature of the (^8He , ^8Be) reaction.

For this experiment, we develop a trigger logic to track two alpha particles produced by ^8Be ejectile at the final focal plane of SHARAQ spectrometer.

2. Detection system for two alpha particles

The momentum distribution of two alphas are less than $\pm 0.73\%$ of that of ^8Be ejectile if we choose the incident beam energy of 200 A MeV. This kinematics enables to detect two alpha particle at the same time in SHARAQ spectrometer.

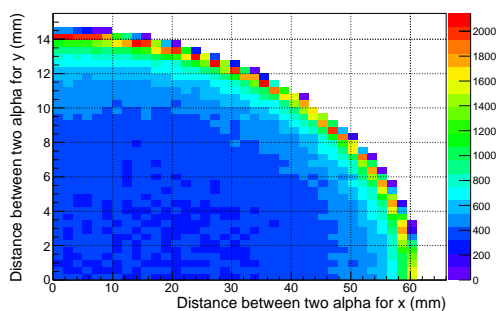


Figure 1. Distance of two alpha particles at the focal planes obtained by a Monte Carlo simulation.

Figure 1 shows the distance of two alpha particles at the focal plane, which was obtained by a Monte Carlo simulation using the transfer matrix and the angular acceptance of SHARAQ spectrometer. The maximum size of decay-corn is estimated to be 60 mm in x direction and 14 mm in y direction. To cover this size sufficiently, we use the present Cathode Readout Drift Chamber (CRDC) which has a large effective area (x: 550 mm, y: 300 mm) and no dead-space as two-particle detection system.

Figure 2 shows a schematic view of CRDC. Two CRDCs and three plastic scintillator for trigger are used. The vertical and horizontal positions of charged particles are determined by measuring the drift time of electrons in the

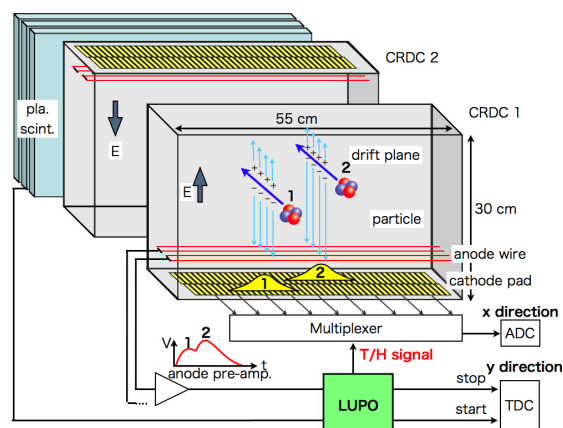


Figure 2. Schematic view of readout system of S2 focal plane

drift plane and by the center of the distribution of induced charges on the cathode pads, respectively. The cathode signals are read out by multiplexer chips triggered signal (Track and Hold: T/H) generated by anode signal. The CRDC has two signals from anode wire and two multiplexed signal from cathode pad. Detailed structure of the CRDC is described in Refs. [3], [4].

Two alpha events derived from background will be distributed uniformly at focal plane compared with events produced by ^8Be which has correlation of phase space seen in Fig. 1. If two-particle tracks can be obtained, signal to noise ratio will be improved by the difference of the distribution. In the present readout system, because the T/H signals are generated by the anode signal from the particle reached to anode wire at first, signal from cathode pad cannot read out correctly for second one. Therefore, it is necessary to develop the logic circuit of the T/H signals for each cathode pad separately. For this reason, we use FPGA-based circuit named LUPU (Logic Unit for Programmable Operation) as trigger logic which easily makes us to develop complicated circuit systematically.

3. LUPU Module as Trigger Logic Module

The LUPU is the VME module having FPGA chips and has the interface of the FPGA and the VME bus. The LUPU module has 4ch NIM input, 4ch NIM output, 16ch LVDS input/output and 8 LEDs. Note that the LUPU not only help us to create complicated logic circuit, but also can be selected, for example, operating modes and settings of delay times as remote control by the VME commands. In addition, only one VME module, LUPU can replace to a lot of NIM standard modules.

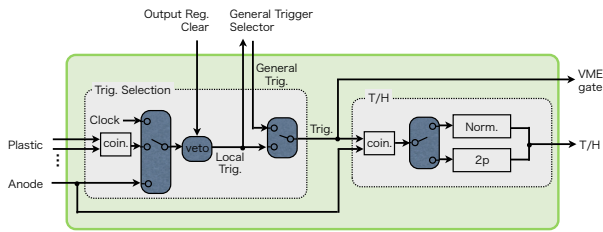


Figure 3. Schematic view of circuit at LUPO as the readout system of CRDC

Figure 3 shows a schematic view of trigger logic. The CRDC trigger module is mainly consisted of two sections.

First one is a trigger selector section where the trigger can be selected for

- coincidence signal of plastic scintillator
- anode signal
- 100 Hz clock signal

as local trigger. This system allows us to test the CRDC system.

Once the local-trigger signal is created, it is sent to the general-trigger selector which can be selected for the local-trigger or another one as the general-trigger of the whole SHARAQ DAQ system. After receiving the general-trigger, the signal originated from the T/H signal can be selected for

- the local-trigger signal
- general-trigger signal of SHARAQ DAQ system.

This system allows us to operate the local DAQ system separately from the total one.

The second one is the T/H create section. It can be selected for

- normal mode
- two particle mode.

If two particles come into the detector, the T/H signal for first cathode-pad plane should be created by the first particle reaching anode wire, and for the second plane by the second particle. On the other hand, if only one particle comes, the T/H signal for each two plane should be created by the same timing of anode signal. This trigger logic is created as the two particle mode. The normal mode create the T/H signal from timing of anode signal for both planes of the CRDC.

The system successfully has worked using test pulse simulating anode and plastic scintillator signals. We plan to test the whole readout system using a beam in the next SHARAQ experiment.

References

- [1] F.M.Marques *et al.*, Phys. Rev. C **65**, 044006 (2002)
- [2] S.C.Pieper, Phys. Rev. Lett. **90**, 252501 (2003)
- [3] S. Michimasa *et al.*, CNS Ann. Rep. 2009 (2011)
- [4] H. Tokieda *et al.*, CNS Ann. Rep. 2009 (2011)

CNS Active Target Development and Test Experiment at HIMAC

S. Ota, S. Michimasa, T. Gunji, H. Yamaguchi, H. Tokieda, T. Hashimoto, R. Akimoro, D. Kahl, M. Dozono, S. Hayakawa, S. Kawase, Y. Kikuchi, Y. Maeda^a, H. Matsubara, H. Otsu^b, S. Kubono, H. Hamagaki, T. Uesaka

Center for Nuclear Study, Graduate School of Science, University of Tokyo

^aDepartment of Physics, Miyazaki University

^bNishina Center for Accelerator-Based Science, RIKEN

We are developing two types of active targets to realize the forward-angle scattering measurement in inverse kinematics. One type is for measuring deuteron-induced reaction to study spin-isospin response and nuclear matter property. The other is for measuring low-energy α -induced reaction to study the reaction rate at the point of view of nuclear astrophysics. To maximize the efficiency in the development we have an intergroup collaboration among SHARAQ, CRIB and quark-physics group. Two physics measurements were performed at CRIB [1, 2] and one test experiment was performed at HIMAC. The property of deuterium gas as a detector gas for GEM was studied [3] before the experiment at HIMAC. In this paper we report the test experiment at HIMAC.

The supernova nucleosynthesis is one of the attractive subject. In the supernova nucleosynthesis various nuclei from the iron-group nuclei to the uranium are produced in the short period. The life time and scale of explosion of supernova depends on the electron-capture rate by the nuclei therein. The core of the star in the pre-stage of supernova is formed by the iron-group nuclei and electrons. The degeneracy pressure of electrons balances the gravity of nuclei at first. When the electrons are captured by the iron-group nuclei and the degeneracy pressure becomes small, then the supernova explosion occurs. Since the dynamics of the supernova explosion depends the electron capture rate not only by the iron but also the nuclei around the iron, the electron capture rates of the iron-group nuclei are important. The electron capture rate strongly depends on the beta+ type Gamow-Teller strength $B(GT+)$. So far, the strengths are theoretically calculated, however, the results using various interactions are different from each other. The measurement of the $B(GT)$ provides the information connected to the electron capture rate without the model of the nuclear structure.

The $B(GT)$ can be extracted from the measurement of β decay for the state locating at the lower energy than the threshold energy of electron capture (Q_{EC}). On the other hand in the star where the temperature is more than 10^9 K, the electrons which have the kinematic energy of a few MeV can populate the excited state which have higher energy than the Q_{EC} . The measurement in the higher-energy range over the Q_{EC} can be performed only in the manner of the charge exchange reaction. To measure the Gamow-Teller transition strength, the missing mass spectroscopy via the charge exchange reaction of $(d, ^2\text{He})$ is the promising tool for the inverse kinematics because of its capability of

the identification of spin, isospin and angular momentum transfer. In this study, we are aiming at the measurement of $B(GT+)$ strength of the iron-group unstable nuclei, especially ^{56}Ni nuclei, which is one of most important nuclei.

The difficulty in the measurement of $(d, ^2\text{He})$ reaction in inverse kinematic is the detection of the low-energy recoiled particles. The low energy recoils cannot exit the commonly-used deuterized target such as deuterized polyethylene or liquid deuterium target. To overcome this difficulty we are developing the active target using deuterium gas, which acts as the target and detection gas at the same time. The active target is a time-projection chamber which has the position sensitivity in three dimensional direction. The region along beam path is masked in our active target so that the electric field is not affected by the spacial charges produced by the beam particles.

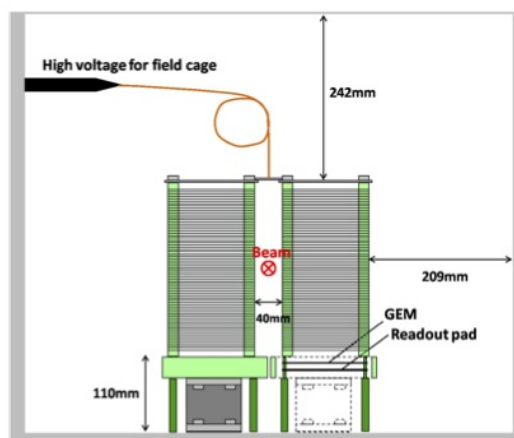


Figure 1. Schematic view of field cages

Fig. 1 shows the schematic view of the active target. There are two field cages to detect the recoiled proton from the decay of ^2He . The electric field is typically 1 kV/cm and drifted electrons are amplified by Gas Electron Multipliers (GEMs). The readout pad is composition of the triangle-shaped electrodes to deduce two dimensional position by means of the charge division. Deuterium gas is filled with 5% mixture of CO_2 gas to decrease the discharge probability. Typical gas flow is 20 cc/min and exhaust gas is collected into balloon filled with N_2 gas keeping the deuterium concentration below the explosion limit. The oxygen concentration in the chamber is also monitored and kept below 2% in the operation. The experiment was performed at PH2

course in HIMAC. A photo of setup is shown in Fig. 2. The beam of ^{56}Fe at 250 MeV/nucleon was irradiated the active target. Two arrays of NaI crystals were attached to the both side of the chamber in order to detect the recoils which have relatively large kinetic energy. The timing and position of the beam particles were monitored by the plastic scintillator hodoscope. The two GEMs were set in each cage to obtain large gas gain. The readout signals from the pad were sampled by using a sampling ADC system COPPER-II with 50 MHz sampling rate. The trigger was generated by the logical add of two signals. One is the logical product of the beam timing and NaI timing, the other one is the logical add of the GEMs timing.

Analysis is in progress.

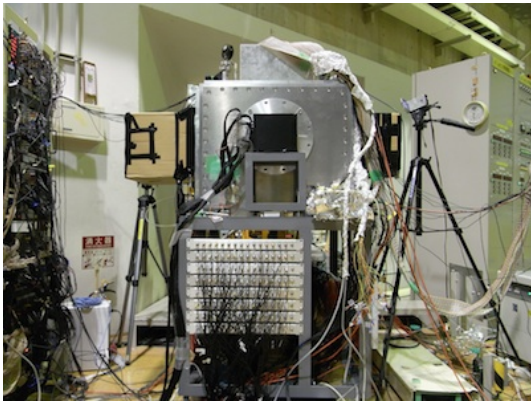


Figure 2. Photo of experimental setup at PH2 course.

References

- [1] T. Hashimoto *et al.*, CNS Ann. Rep. 2010 (2012).
- [2] D. Kahl *et al.*, In preparation.
- [3] H. Tokieda *et al.*, CNS Ann. Rep. 2010 (2012).

Performance of Gas Electron Multiplier with Deuterium Gas

H. Tokieda, S. Ota, T. Hashimoto^a, S. Michimasa, M. Dozono^b, H. Matubara, Y. Kikuchi, T. Gunji, H. Yamaguchi, D. M. Kahl, R. Akimoto, H. Hamagaki, S. Kubono, and T. Uesaka^b

Center for Nuclear Study, Graduate School of Science, University of Tokyo

^a*Research Center for Nuclear Physics, Osaka University*

^b*RIKEN (The Institute of Physical and Chemical Research)*

An active target by using a Gas Electron Multiplier (GEM) are being developed. The active target is of the “beam transparent type” and is intended for the study of nuclear structures through the measurement of the Gamow-Teller strength in the ($d, ^2\text{He}$) reaction by using intense unstable beams of iron group nuclei; inverse kinematics and missing mass spectroscopy will be used in the study. We need to measure the position of the recoiled particle ^2He , which decays into two protons instantly, with a low kinetic energy.

The structure of the active target is optimised so as not to measure the beam particles for high beam rates up to 10^7 Hz and with a high incident energy in the range 150–200 MeV/u. Figure 1 shows a photograph (left) and a schematic view (right) of the active target.

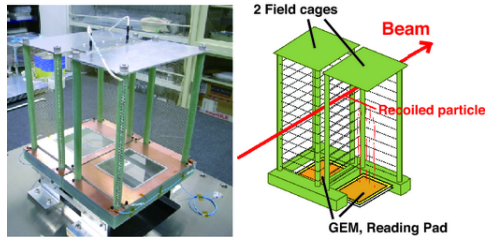


Figure 1. Photograph (left) and schematic view (right) of the active target. The structure is optimised so as not to measure the beam particles.

The required gas gain, angular resolution, energy resolution, and operation beam rate for this active target to successfully be used in studies are approximately 10^4 , 7.5 mrad in the lab frame, 10%, and 10^7 Hz, respectively. This report describes the basic performance of the GEM with deuterium (D_2) gas at 1 atm.

The GEM used in the performance test was a CNS-GEM (for details, see, e.g., [1]). It was $100 \mu\text{m}$ thick and consisted of an insulator Liquid Crystal Polymer (LCP) and copper. The pitch and diameter of the holes were $140 \mu\text{m}$ and $70 \mu\text{m}$, respectively. Performance test were carried out with a single GEM layer and a double GEM layer mounted in a chamber. We used D_2 gas as the counter gas and CO_2 as the quencher gas at 1 atm.

Figure 2 shows two schematic views of the performance test setup with the single GEM layer mounted in the chamber. The upper panel shows the position of the GEM relative to the 3-compound α source. The lower panel shows the resistive chain to which a high-voltage (HV) is applied.

Figure 3 shows a schematic view of the performance test

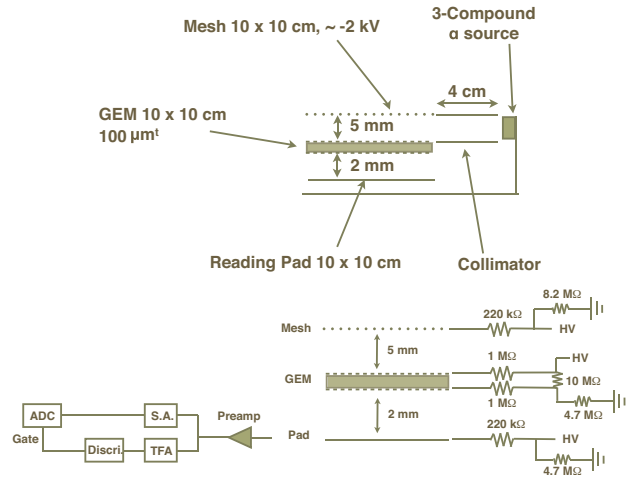


Figure 2. Two schematic views of the performance test setup for the single GEM layer. The upper panel shows the position of the GEM relative to the 3-compound α source. The lower panel shows the resistive chain to which a HV is applied.

setup with the double GEM layer mounted in the chamber. This view shows the voltage divider resistive chain to which a HV is provided.

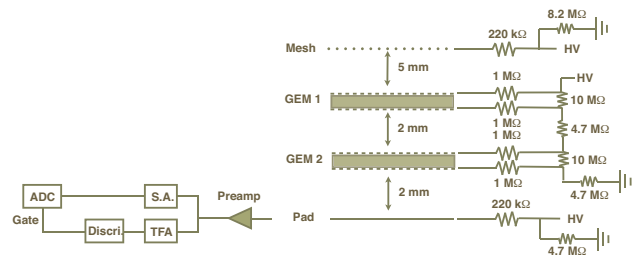


Figure 3. Schematic view of the performance test setup with the double GEM layer. This view shows the HV being supplied to the resistive chain.

The distance between the mesh and the top of the GEM and that between the bottom of the GEM and the pad are 5 mm and 2 mm, respectively. In the case of the double GEM layer, the distance between the GEM layers is 2 mm. The size of the mesh, GEM, and pad is the same, $10 \times 10 \text{ cm}^2$. The HV applied to the mesh, GEM, and pad is supplied from a separate HV source. The voltage between the mesh and GEM is denoted by V_f . During our measurement, V_f and the HV applied to the pad were kept at about 300 V

and 50 V, respectively.

The voltage applied between the GEM electrodes is denoted by V_{GEM} . We measured the gas gain of the GEM with D_2 gas, as well as the discharge-starting voltage.

Pure D_2 gas and D_2 (95%) + CO_2 (5%) gas were used in this test at 1 atm.

The signal was read out from the pad and input to a preamp (ORTEC 142AG) and a shaping amplifier (SA, ORTEC 572A). The data were recorded by an ADC (CAEN V785). A trigger was provided through a timing-filter amplifier (TFA, ORTEC 474) by using the signal read out from the pad.

When the V_{GEM} was more than 600 V for pure D_2 gas, discharges occurred. Hence, we were not able to obtain sufficient data to evaluate the gas gain.

We measured the gas gain for the single GEM layer and double GEM layer for D_2 (95%) + CO_2 (5%) gas at a pressure of 1 atm. In the single GEM layer, the data were recorded at V_{GEM} values of 710, 716, 720, 730, 740, 750, and 760 V. When the V_{GEM} was 760 V, discharges started. In the double GEM layer, the data were obtained at V_{GEM} values of 600, 625, 650, and 675 V. When the V_{GEM} was 675 V, discharges started.

Figure 4 shows preliminary values of the gas gain as a function of V_{GEM} for the single GEM layer and double GEM layer for D_2 (95%) + CO_2 (5%) gas at a pressure of 1 atm. The highest gas gain for the two GEM layers was about 20 and 280, respectively.

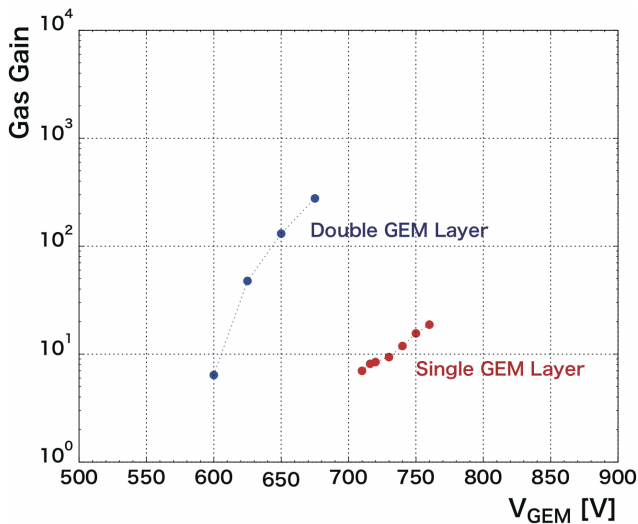


Figure 4. Preliminary values of the gas gain as a function of V_{GEM} for the single GEM layer and double GEM layer for D_2 (95%) + CO_2 (5%) gas at a pressure of 1 atm.

In the summary, we measured the gas gain for a single GEM layer and a double GEM layer for D_2 (95%) + CO_2 (5%) gas at a pressure of 1 atm. The gas gain obtained in this test doesn't reach the requirement. In respect of pure D_2 gas we were not able to obtain sufficient data to evaluate the gas gain owing discharges.

To accomplish the required gas gain, the development such as changing a gas pressure is currently in progress.

References

- [1] Y. L. Yamaguchi *et al.*: CNS-REP-69(2005) 83–84.

Development of position extraction for segmented Ge detectors by using pulse shape analysis

S. Go, S. Shimoura, E. Ideguchi, S. Ota, H. Miya, H. Baba^a

Center for Nuclear Study, Graduate School of Science, University of Tokyo

^aRIKEN (The Institute of Physical and Chemical Research)

Extraction of gamma-ray interaction positions is important for the correction of Doppler shift broadening. We are developing a method to extract gamma-ray interaction positions in the segmented planar Ge detector array, CNS-GRAPE [1]. The total array of CNS-GRAPE consists of 18 detectors and each of which contains two Ge planer crystals with the effective radius of 30 mm and the thickness of 20 mm. The cathode of each detector is divided into 9 segments, and the anode is common (Fig.1). The pulse shape data from cathodes are taken by 100 MHz Flash ADC. Output pulses from each cathode show different shapes depending on gamma-ray interaction points and its deposited energy.

In order to extract three-dimensional interaction position, a detailed comparison between the measured and simulated pulse shapes is important. The time evolution of induced charge signal $Q(t)$ can be simulated by calculating the three dimensional electrical potential and using the weighting potential method by the Schockley-Ramo theorem [3]. By using this theorem, induced charge is expressed as,

$$Q(t) = n_0 e \phi_w(\mathbf{r}_e(t)) - n_0 e \phi_w(\mathbf{r}_h(t)), \quad (1)$$

where \mathbf{r}_i ($i = h, e$) are three dimensional position of the hole and electron as a function of time. n is the number of carriers created by the interaction of gamma-ray and e equals to elementary charge. The velocity of each carrier is approximated by the following equation [4],

$$\frac{dz}{dt} = v(E(z)) = \frac{\mu_0 E(z)}{[1 + (E(z)/E_0)^\beta]^{1/\beta}} \approx \frac{\mu_0 E(z)}{1 + E(z)/E_0}. \quad (2)$$

Empirical parameters E_0 , β , μ_0 are given in Table 1. In this simulation, the electron and the hole are assumed to move to electrodes in z -direction.

$$E(z) = \frac{V}{d} + \frac{\rho}{\varepsilon} \left(\frac{d}{2} - z \right). \quad (3)$$

	Hole	Electron
E_0 (V/cm)	210.5	275.0
μ_0 (cm ² /V·s)	4.2×10^4	3.6×10^4
β (unitless)	1.36	1.32

Table 1. Empirical parameter of carrier velocity [4].

V is an operating voltage, d is the distance from the anode to the cathodes, ε is permittivity of crystal and ρ is the impurity density of the crystal. When the electrical field in

the crystal is correctly formed, carriers can reach electrodes and the count rate of gamma-ray becomes stable. ρ is evaluated to be $0.70 - 0.80 \times 10^{10}$ e/cm³ from the count rate of gamma-ray as a function of voltage. With these parameters, pulse shapes at each segment are simulated in the effective area.

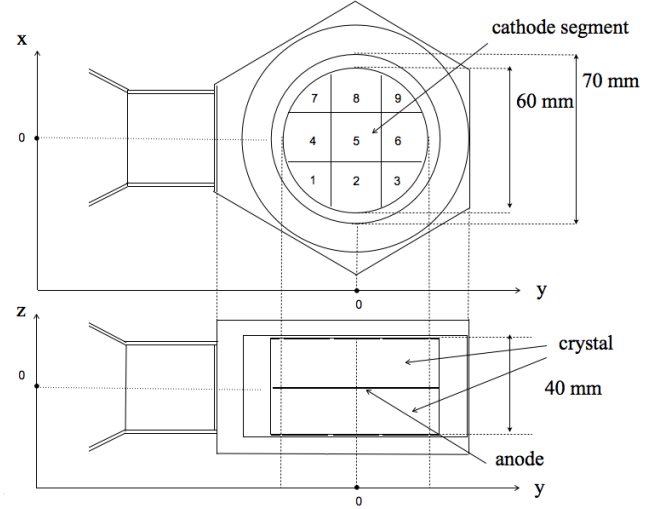


Figure 1. Schematic drawing of a GRAPE detector. Two crystals are in chassis with an anode between them. The size of each crystal are 20 mm thickness and 70 mm diameter. The cathodes are divided into 3 × 3 segments. Each number is the segment number.

To characterize the pulse shapes and to deduce interaction positions, centroid and width of the current pulses shapes, $f(t) = dQ(t)/dt$, are introduced. These values are given by,

$$\langle T \rangle_H - \langle T \rangle_S = \frac{\sum_i t_i \times f_H(t_i)}{\sum_i f_H(t_i)} - \frac{\sum_i t_i \times f_S(t_i)}{\sum_i f_S(t_i)}, \quad (4)$$

$$\langle \sigma \rangle_H = \frac{\sqrt{\sum_i (t_i - \langle T \rangle)^2 \times f(t_i)_H}}{\sum_i f(t_i)_H}, \quad (5)$$

where t_i denotes digitized time, and suffix ‘‘H’’ and ‘‘S’’ at $f(t)$ mean the signal of ‘‘Hit segment’’ and ‘‘Sum of the surrounding segment’’, respectively. To cancel the offset of time, the form $\langle T \rangle_H - \langle T \rangle_S$ are taken. These value have the characteristic dependence of z -direction (Fig.2). $\langle T \rangle_H - \langle T \rangle_S$ tend to be small in case the interaction points is near the anode because rise time of charge signals depend mainly on the movement of holes. The width of the current pulse shape is narrow in the center of the detector because the sum of the contribution of electron and hole are larger

than around electrodes, and the rise time of the charge signal becomes fast. Similar correlations are also seen in the other segment.

To deduce radial position x, y the following values are taken.

$$\langle T_x \rangle_{\text{Center}} = \frac{\sum_i t_i \times f_{5+8}(t_i)}{\sum_i f_{5+8}(t_i)} - \frac{\sum_i t_i \times f_{5+2}(t_i)}{\sum_i f_{5+2}(t_i)}. \quad (6)$$

$$\langle T_y \rangle_{\text{Center}} = \frac{\sum_i t_i \times f_{5+6}(t_i)}{\sum_i f_{5+6}(t_i)} - \frac{\sum_i t_i \times f_{5+4}(t_i)}{\sum_i f_{5+4}(t_i)}. \quad (7)$$

The sum of the current signal at the nearest segment and the surrounding segment has dependency of x, y . Suffix number in $f(t_i)$ corresponds to the segment number shown in Fig.1. Correlation between $\langle T_x \rangle$ and $\langle T_y \rangle$ in the center segment is shown in Fig.3. Similar correlations are also seen in the other segment.

$\langle T_x \rangle, \langle T_y \rangle, \langle T_H \rangle - \langle T_S \rangle$, and $\langle \sigma_H \rangle$ have the less dependency of gamma-ray energy. It means that these values can be applicable for wide range of energy to extract interaction position.

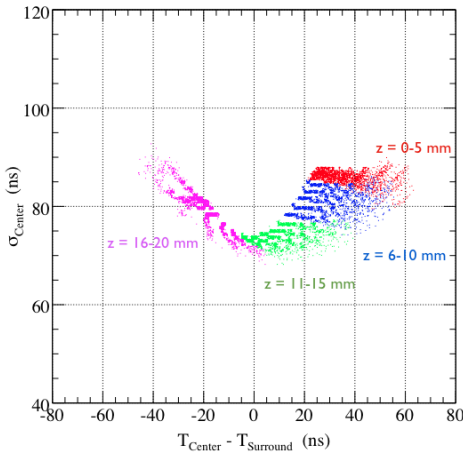


Figure 2. Correlation between the centroid of current pulse $\langle T_H \rangle - \langle T_S \rangle$ and width $\langle \sigma_H \rangle$ in center segment. Each point corresponds to the interaction point of gamma-ray, and each color to depth of detector in the simulation. $\langle T_H \rangle - \langle T_S \rangle$ and $\langle \sigma_H \rangle$ are less dependent on the zero point of pulse-shape. $\langle T_S \rangle$ is created by the signal of (2+4+5+6+8) in the case that gamma-ray interacts in the center area.

Summary and Outlook

The current pulse shapes from segmented Ge detectors are sensitive to the interaction position of gamma-ray. Correlation between centroid and width of current signal are important to deduce interaction position.

Three-dimensional position extraction by using these characteristic correlation will be tested.

Acknowledgement

This work is supported by the PACIFIC project, upgrading of data acquisition system of high-rate RI beam experiments.

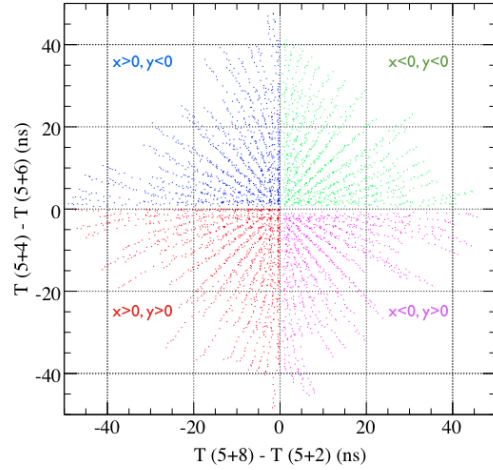


Figure 3. Correlation between the centroid of current pulse $\langle T_x \rangle_{\text{Center}}$ and $\langle T_y \rangle_{\text{Center}}$ ($z \leq 10$). Each point corresponds to the interaction point of gamma-ray, and each color to breadth of detector in the simulation. $\langle T_x \rangle_{\text{Center}}$ and $\langle T_y \rangle_{\text{Center}}$ are less dependent on the zero point of pulse shape.

References

- [1] S. Shimoura, Nucl. Instr. and Meth. A **525** (2004) 188.
- [2] W. Schockley, J. Appl. Phys. **9** (1938) 635.
- [3] S. Ramo, Proc. IRE **27** (1939) 584.
- [4] M. Burks *et al.*, NSS Conference Record, IEEE **2** (2004) 1114.

Development of a Readout System for the GEM-based X-ray Imaging Detector

A. Nukariya, H. Hamagaki, Y. Tanaka^a, T. Fusayasu^a, and T. Kawaguchi^a

Center for Nuclear Study, Graduate School of Science, University of Tokyo

^a *Nagasaki Institute of Applied Science*

1. Introduction

Film shots are a popular way for detection of X-rays in non-destructive inspections. However, film shots are not suitable for real-time imaging, and it is difficult to make a device size small. As a new compact device of real-time imaging, a GEM-based X-ray imaging detector is proposed. The GEM-based imaging device is composed of a photo-electron converter, GEMs, strip anodes and a readout system [1]. Development of the readout system is needed because the readout system for the GEM-based imaging detector doesn't exist. A frame rate of the readout system needs to be variable depending on target materials.

Field Programmable Gate Array (FPGA) and SiTCP are employed in the readout system to achieve a high speed data transmission. FPGA is popularly used for image processing since an internal logic can be modified easily by FPGA. SiTCP can transmit data by 1GHz, and it is easily operated together with FPGA. Therefore, they can realize a high speed readout system with a flexibility for user's demands. In this report, we show the current status of development of the readout system for a GEM-based real-time imaging device.

2. GEM-based X-ray Imaging Device

Imaging size of the present system is 200 mm × 200 mm. An imaging procedure from X-ray detections is as follows. First, X-rays come in a device. They are converted to electrons by a photo-electron converter made of lead, whose conversion rate is 10% [3]. Then electrons are multiplied by GEMs. Electrons are detected by strip type anodes. Anodes are put in X and Y directions. Compared with a pixel type anode, a strip type anode has advantage on cost, readout speed and a variation of a detector size. The required position resolution is several mm. A charge is converted to a digital signal by a 10-bit pipeline ADC with 10Msps. Furthermore, time information is given by a 4-bit 100Msps TDC and a 6-bit 10MHz clock counter. Time information is needed for coincidence of data from X and Y readout strips. FPGA formats digital signals from front-end chips to data so that PC can read data. SiTCP can transmit formatted data to PC with a maximum rate of 1Gbps. Finally, an image with 200mm × 200mm is constructed from obtained events.

3. Readout System

The readout system is composed of front-end chips (GEMFE2), FPGA, SiTCP and PC. A schematic of the readout system is shown in Fig. 1. A data flow is indicated by solid lines. Dotted lines show control signals. Data are transmitted according to solid lines.

The clocks are used in FPGA, and they are generated by

a crystal unit.

- MCLK - Clock for GEMFE2.
- RCLK - Readout clock defining a readout speed.
- HCLK - High speed clock for TDC.

In the readout system, a data size is 24 bits. 4 bits are used for STATUS, which indicates whether data can be correctly processed by GEMFE2.

- FIFO Full - The number of data is over a depth of FIFO.
- FIFO Empty - All data in a channel are read.
- FIFO Busy - FIFO is in writing mode.
- Chip Full - GEMFE2 fails to read all channels.

10 bits are dedicated for two kinds of time informations of electron detection. A 6-bit counter with a 10MHz clock provides Coarse Time, which represents an electron input time. The other input time, Fine Time, is provided by a 100Msps 4-bit TDC with a 10 times better time resolution compared to Coarse Time. Input times informations of charges from X and Y readout strips are checked if they are coincidence, using Coarse time and Fine time. The rest 10 bits are used for ADC, which represents an electric charge from readout strips.

FPGA reads 4 GEMFE2 chips at once. GEMFE2 has MCLK-based 7-bit counter, two 10-depth 23-bit FIFOs. When either FIFO is in writing mode, the other is always in reading mode. This method is efficient to take data fast. Readout channel is changed when FIFO Empty is obtained. MSB of the 7-bit counter is used for switching of the IO mode. GEMFE2 has interfaces for both MCLK and RCLK since 80 readout clocks are needed for full data in FIFO.

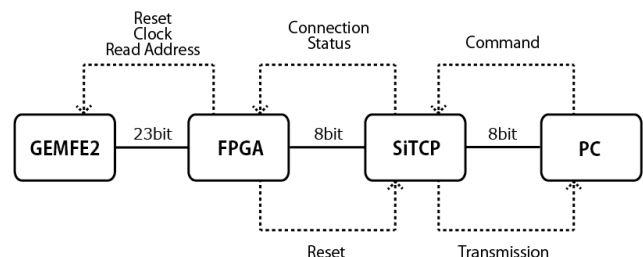


Figure 1. Readout System

FPGA also controls DAC which determines a threshold value. A threshold value can be changed easily depending on various conditions (noise, target object, etc).

FPGA converts 24-bit data into three 8-bit data sets, and then SiTCP transmits one 8-bit data set per a clock to PC.

The transferred data from SiTCP are decomposed into charge and time information separately. Time information is used in determining the position of electrons. An image is constructed from charge and position information. Average ADC counts in multi-events are used to reduce statistical errors.

4. FPGA

Figure 2 is a block diagram of FPGA. Control Manager controls all parts of FPGA and peripheral devices such as DAC, SiTCP and clocks. The process sequence of Control Manager is shown in Fig. 3. Control Manager resets GEMFE2 and the other part of FPGA in STATE RESET. The threshold value determined by DAC is configured in STATE CONFIGURE if the threshold is not configured. Finally, are transmitted from GEMFE2 to PC in STATE TRANSFER. The state moves and stays in STATE RESET if data transmission is terminated due to a trouble.

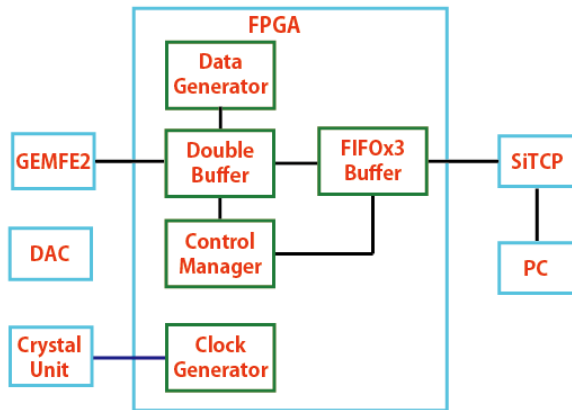


Figure 2. Block diagram of FPGA

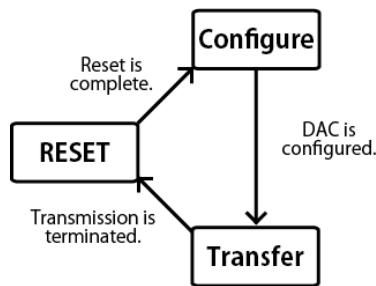


Figure 3. State machine of Control Manager

5. FPGA Simulation

FPGA simulations have been made by the simulator Xilinx ISE to verify if the designed readout system works correctly. First, a behavior model simulation is conducted. In this simulation level, any circuits are not implemented on FPGA, but only functions are considered. Figure 4 shows a sample event generated by a test bench written in VHDL.

One normal data without any STATUS and following eight data with FIFO Empty are input. Correct responses of FPGA to the inputs are seen as shown in Fig. 5.

Next, circuits are implemented on FPGA. Data Generator generates events to Double Buffer on FPGA. With this configuration, the designed circuit behavior without control signals to GEMFE2 chips is simulated. Outputs from FPGA are checked by a readout software every 1 byte. In this simulation, FPGA works correctly. Finally, controls of GEMFE2 chips are tested with an input wave form as shown in Fig. 6. An input cycle is 16 μ s, and a duty cycle is 23%. A peak value is set above threshold. However, expected ADC value is not obtained. This is caused from wrong control of GEMFE2 in the current design of the readout system.

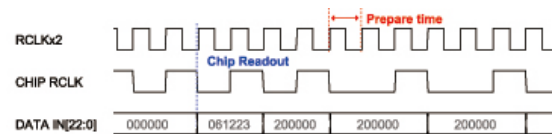


Figure 4. Sample event for the behavior model simulation

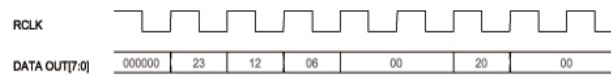


Figure 5. Responses of FPGA in the behavior model simulation

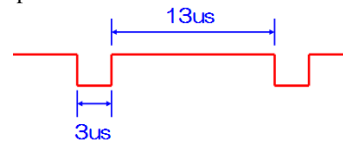


Figure 6. Input wave form

6. Summary and outlooks

We have developed the readout system for a GEM-based X-ray imaging device. The behavior of the current design was checked by simulations. The readout system can work correctly without control of GEMFE2 chips. A wrong control of GEMFE2 chip was found in the current specification document of GEMFE2. Therefore, the document should be revised. Process speed isn't considered in the current design. After revision is finished, we will improve a readout speed. An image processing software will also be developed. After we finish to develop the readout system, a test experiment with 500 keV X-ray will be conducted.

References

- [1] T. Fusayasu *et al.*, 2009 IEEE Nuclear Science Symposium Conference Record N19-5, pp.1100-1102
- [2] T. Fusayasu *et al.*, 2007 IEEE Nuclear Science Symposium Conference Record, pp.305-308
- [3] J. Missimer *et al.*, Phys. Med. Biol. 49 (2004) 2069-2081

Production of stable metallic ion beams of Hyper ECR ion source

Y. Ohshiro, S. Yamaka, S. Watanabe, H. Muto and S. Kubono *Center for Nuclear Study, Graduate School of Science, University of Tokyo*

1. Introduction

Center for Nuclear Study, University of Tokyo (CNS) is the laboratory for studying mainly heavy ion nuclear physics in RIBF facility collaborating with RIKEN. Heavy ion beams are necessary for these studying. Therefore, we are producing gaseous and metallic heavy ion species for nuclear and biological experiments. Recently, we improved an evaporation system of Hyper ECR ion source [1] and succeeded in producing high intensity heavy ion beams from solid materials and supplying these stable beams. Typical examples of ${}^6\text{Li}^{3+}$, ${}^{28}\text{Si}^{9+}$, ${}^{40}\text{Ca}^{12+}$, ${}^{59}\text{Co}^{15+}$ beams were extracted two times higher intensity than previous system. In this paper, we describe the new evaporation system.

2. Evaporation system of Hyper ECR ion source

We introduce an inserting-rod-method in the case of high-melting-point materials and use a crucible-method in the case of low-melting-point one. As shown in Figure 1, ECR zone is formed by mirror and sextuple magnetic fields. Maximum magnetic field of a mirror coil is 1.3 T and surface strength of a sextuple magnet is 1.1 T. The ECR zone length is approximately 70 mm. Microwave power of 14.24GHz is guided into the plasma chamber to generate the ECR plasma. Solid-material rod is set near ECR zone. Electrons are accelerated by RF field in the ECR zone. Evaporated neutral gases from one are diffused to the center of plasma chamber and ionized by electron impact process.

3. Optimization of the rod position

In the case of the inserting-rod-method [2], we had experienced sometimes beam intensity fluctuations. The solid-material-rod has 4 mm in diameter and 60 mm in length. Usually, the one was located 75 mm away from the edge of the ECR zone so as to evaporate a surface of the one. In this insertion way, a density control of evaporated materials was difficult. If we put the one much closer to the ECR zone at the center axis it stopped energetic electrons and resultant beam intensity was seriously reduced.

In order to improve this difficulty, we have studied insertion-way of the solid-material-rods to the ECR zone. It was found that the rods are set near the plasma chamber wall in 150 degrees to the center axis without disturbing energetic electron movements. And we succeeded in obtaining a stable high intensity beams. We call this method as “new rod method” for introducing the rods from the plasma chamber wall.

4. Optimization of the crucible vapor

Figure 2 shows cross section of the plasma chamber with introduced crucible. In ordinary method [3], it was difficult to obtain high enough extraction voltage because high extraction current flow was observed under high-RF-power condition.

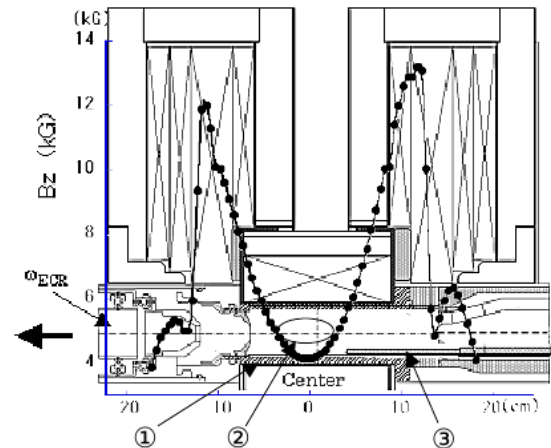


Figure 1. Schematic cross section of the Hyper ECR ion source. 1: Plasma chamber 2: ECR zone. 3: Solid material rod

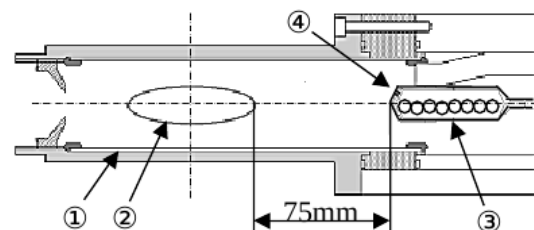


Figure 2. Detail of the center region of Hyper ECR ion source. 1: Plasma chamber 2: ECR zone 3: Crucible 4: Jet nozzles

Diameter of a hole of the crucible was 4 mm and it was too large to exhaust metal vapor. Materials of low melting temperature are usually over supply to the ECR zone from the crucible. When the crucible is heated at the high temperature, evaporated materials are exhausted through the hole. The excessive heating to the materials exhaust it through the boiling process. The melted materials are dropped and stacked on the plasma chamber.

Recently we changed diameter of the hole of the crucible 2 mm from 4 mm and made 5 holes from one. And we succeeded continuous vapor evaporation and we can put high extraction voltage stably even under high RF power condition. Remaining materials after operation were small granules in the chamber and it was easy to take out. Consumption rate of evaporated materials was reduced to 1/3. We call this method as "new crucible method" for introducing the low melting point materials.

5. Ionization of solid materials

Table 1 shows beam intensities of the typical ion species from the ion source. New rod method is being applied to high melting point materials. Typical examples of $^{28}\text{Si}^{9+}$, $^{40}\text{Ca}^{12+}$ and $^{59}\text{Co}^{15+}$ ions were produced from materials of SiO_2 (melting point is 1500 degrees), CaO (melting point is 2572 degree) and Co (melting point is 1495 degree) respectively. Beam intensities of $^{28}\text{Si}^{9+}$, $^{40}\text{Ca}^{12+}$ and $^{59}\text{Co}^{15+}$ ions were 32, 25 and 15 μA , respectively. The tip of the rod can be closed to the ECR zone and stable high beam intensity can be obtained.

In the case of new crucible method we can select number of holes of the crucible to control the quantity of evaporation of low melting point materials. When we operate multi-charge ions of low melting point materials, we reduce the holes of the crucible and feed high RF power. Typical examples of $^7\text{Li}^{2+}$, $^6\text{Li}^{3+}$ and $^{32}\text{S}^{9+}$ ion beams were produced by the new crucible and the number of evaporation holes were 5, 3 and 1 respectively. And the beam intensities of $^7\text{Li}^{2+}$, $^6\text{Li}^{3+}$ and $^{32}\text{S}^{9+}$ ions were 200, 75 and 47 μA respectively as shown in Table 1. Consumption rate of the materials was about 13 mg/h and capacity of the crucible was 10 ml.

Table 1. Beam intensities of the typical ion species.

Ion	Beam Intensity [μA]	Charged materials	m.p.($^\circ\text{C}$)
$^7\text{Li}^{2+}$	200	^7Li pure elemen (crucible)	180
$^6\text{Li}^{3+}$	75	^6Li pure elemen (crucible)	180
$^{28}\text{Si}^{9+}$	35	SiO_2 rod	1500
$^{32}\text{S}^{9+}$	47	S pure elements (crucible)	119
$^{40}\text{Ca}^{12+}$	25	CaO rod	2572
$^{59}\text{Co}^{15+}$	20	co pure elements (rod)	1495

6. Performance of metal ion beams

Metal ion beams were operated and supplied for experiments smoothly without sudden fluctuations. Beam transport efficiency is shown in Figure 3. In the case of $^6\text{Li}^{3+}$ and $^{28}\text{Si}^{9+}$ ion beams of 20-30 μA , these beams were injected to the AVF cyclotron and extraction efficiency was about 10%. Those beams were transported to the experimental target and on-target beam intensities were 1-2 μA . Irradi-

ation ratio was 70-90%. Improvements of the evaporation system at the ion source are contributing experimental results drastically. Arrangements of new rod method also improved day's continuous operation. We operated $^{28}\text{Si}^{9+}$ ion beam for 17 days continuously without any troubles. New crucible method also achieved 12 days continuous operation for $^6\text{Li}^{3+}$ ion beam. These improvements completely solved serious beam intensity reduction and fluctuations.

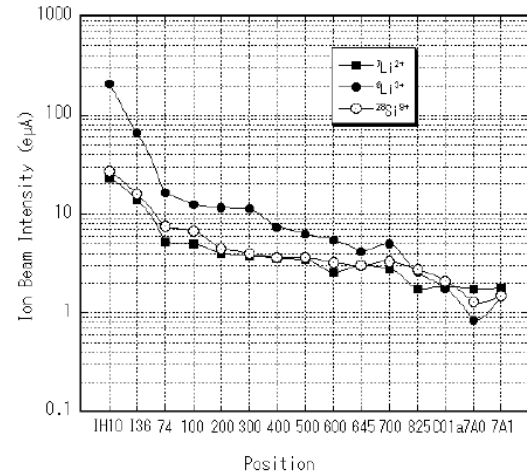


Figure 3. Beam transmission currents from the ion source to the exit of the cyclotron. IH10 and C01a are extraction points of the ion source and the cyclotron respectively. 7A1 is the position [4] of the nuclear target for experiment.

7. Summary

We succeeded in new evaporation systems of solid materials to extract stable high intensity beams. By using these new methods, we are planning to produce and supply new heavy ion species for heavy ion experiments.

References

- [1] Y. Ohshiro *et al.*, RIKEN Accel. Prog. Rep. 35 (2002) 256
- [2] Y. Ohshiro *et al.*, RIKEN Accel. Prog. Rep. 38 (2005) 253
- [3] Y. Ohshiro *et al.*, RIKEN Accel. Prog. Rep. 39 (2006) 231
- [4] Y. Yanagisawa *et al.*: Nucl. Instrum. Methods Phys. Res. A 539, 74 (2005).

Theoretical Nuclear Physics

Large scale nuclear shell-model calculations in CNS

N. Shimizu^a, T. Otsuka^{a,b,c}, Y. Utsuno^d and T. Abe^a

^aCenter for Nuclear Study, Graduate School of Science, University of Tokyo

^bDepartment of Physics, Graduate School of Science, University of Tokyo

^cNational Superconducting Cyclotron Laboratory, Michigan State University

^dAdvanced Science Research Center, Japan Atomic Energy Agency

1. Introduction

Our group has actively performed nuclear shell-model calculations to investigate nuclear structure and its underlying physics. These theoretical works have been supported by the CNS, RIKEN Nishina Center [1, 2], and the Department of Physics, University of Tokyo [3]. We report progress on the developments of the Monte Carlo shell model (MCSM) framework [4] and its applications in the fiscal year 2010. These activities were strongly motivated by High Performance Computing Infrastructure (HPCI) Strategic Program Field 5 “The origin of matter and the universe”, which launches at the beginning of the fiscal year 2011.

2. Fast computation of the Hamiltonian kernel for the MCSM

The MCSM is a powerful method for performing a shell-model calculation which is not feasible by the conventional diagonalization method because of huge dimensionality of the Hamiltonian. In this section, we report new algorithm to accelerate the MCSM calculations which enables much faster computation than the former MCSM code that has been used in many applications [4].

In the MCSM calculation, most of the computation time is devoted to the evaluation of the Hamiltonian kernel given by $\langle V \rangle = \sum_{l_1 l_2 l_3 l_4} \rho_{l_3 l_1} \bar{v}_{l_1 l_2 l_3 l_4} \rho_{l_4 l_2}$, where $\bar{v}_{l_1 l_2 l_3 l_4} = \langle l_1 l_2 | V | l_3 l_4 \rangle$ and ρ is the density matrix. The l_i denotes an index of a single particle state. It is not efficient to directly execute this formula because many of the matrix elements $\bar{v}_{l_1 l_2 l_3 l_4}$ vanish owing to the symmetry of the Hamiltonian. To avoid the operation of the vanishing matrix element, the former MCSM code adopted the so-called list-vector method. In this numerical method, a set of (l_1, l_2, l_3, l_4) with non-vanishing $\bar{v}_{l_1 l_2 l_3 l_4}$ is stored in memory and the summation over l_1 to l_4 takes place in the set only.

We find another method for efficient computing. The symmetry of the Hamiltonian requires that $J_z(l_1) + J_z(l_2)$ should be equal to $J_z(l_3) + J_z(l_4)$ to have non-vanishing $\bar{v}_{l_1 l_2 l_3 l_4}$, equivalent with $J_z(l_3) - J_z(l_1) = -(J_z(l_4) - J_z(l_2))$, where $J_z(l)$ is the z component of the angular momentum of the orbit l . This imposes restriction on the indexes (l_1, l_2, l_3, l_4) to be summed over. In addition, by mapping the set (l_1, l_3) onto a one-dimensional index l_{31} , the expression of V becomes a sum of (vector)^T × (matrix) × (vector), where most of the matrix elements are non vanishing. This is called the matrix method.

In the MCSM, since a number of Slater determinants are superposed, similar calculations with different density matrices should be done at the same time, keeping $v_{l_1 l_2 l_3 l_4}$

fixed: to be clearer, the (matrix) × (vector) operations are now written as Av_1, Av_2, Av_3, \dots , where A is the matrix commonly used and v ’s are different vectors. By binding those vectors into a matrix, it is equivalent with a product of matrices AU , where $U = (v_1, v_2, v_3, \dots)$. This is called the matrix method with binding vector.

By implementing the matrix method with binding vector, the performance of the MCSM code was far improved and reaches 70% of the theoretical peak performance on a recent Intel CPUs. This is because the product of matrices needs much less memory access per floating-point operation than the product of a matrix and a vector by utilizing the Level 3 BLAS library. The code development in this direction will become more important for utilizing future massively parallel supercomputers, since memory bandwidth of future computers will be small in comparison with the enhancement of floating point operation performance.

3. Energy-variance extrapolation method in the MCSM

We introduced an extrapolation method utilizing energy variance in the MCSM to estimate the energy eigenvalue and observables accurately [6]. In the MCSM, a wave function is represented by a linear combination of angular-momentum, parity projected Slater determinants. By increasing the number of the Slater determinants, N , successively, we obtain a successive sequence of the approximated wave functions $|\Phi_1\rangle, |\Phi_2\rangle, \dots, |\Phi_N\rangle, \dots$. For each N , we evaluate the energy variance as

$$\langle \Delta H^2 \rangle_N \equiv \langle \Psi_N | H^2 | \Psi_N \rangle - \langle \Psi_N | H | \Psi_N \rangle^2 \quad (1)$$

and we plot the energy E_N as a function of its variance. As we increase N and improve the approximation, the resulting energy approaches the exact energy, and the corresponding energy variance approaches zero. These values are fitted by a second-order polynomial, and the energy is extrapolated to the limit of $\langle \Delta H^2 \rangle \rightarrow 0$ in the same manner as other applications of energy-variance extrapolation [5].

The feasibility of this method was demonstrated for the full $f5pg9$ -shell calculation of ⁶⁸Se. Figure 1 plots the approximated energies as functions of the corresponding energy variances. The red solid lines are fitted for these points, and it can be easily seen that the extrapolated energies, or the y -intercepts of the fitted lines, agree quite well with the exact values. The applicability of the method to a system beyond the current limit of exact diagonalization has been also verified for the $pf + g_{9/2}$ -shell calculation of ⁶⁴Ge [6].

We further discussed the behavior of the energy-variance extrapolation in comparison with other extrapolation methods, and also discussed the nuclear structure of ⁷²Se, which

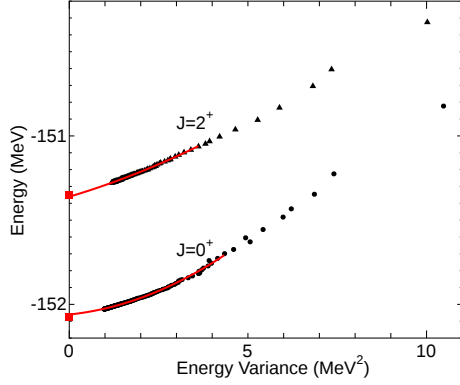


Figure 1. (Color online) Energy variance vs. energy plot of 0_1^+ and 2_1^+ states of ^{68}Se with JUN45 effective interaction. The square symbols on the y-axis denote the exact values obtained by the shell-model code MSHELL64 [7].

is known to show features of shape coexistence [8].

4. Benchmark calculations of the no-core MCSM in light nuclei

One of the major challenges of nuclear theory is to understand the nuclear structures and reactions from *ab-initio* calculations with realistic nuclear forces. The no-core shell model (NCSM) is one of these *ab-initio* methods. One obstacle for carrying out these calculations is the demand for extensive computational resources. Even at state-of-the-art computational facilities, the NCSM calculations are restricted up to the p-shell nuclei with sufficiently large model spaces. Therefore, a method to overcome the current computational limitation of the standard NCSM calculations is needed.

With this motivation, the MCSM applied to no-core full configuration interaction (FCI) calculations [9]. As the benchmark, we select 9 states of light nuclei; ^4He (0^+), ^6He (0^+), ^6Li (1^+), ^7Li ($1/2^-$, $3/2^-$), ^8Be (0^+), ^{10}B (1^+ , 3^+), and ^{12}C (0^+). The calculated observables are seven ground- and two excited-state energies. The model space is truncated by the number of the major shells for the single-particle states. We adopt $N_{\text{shell}} = 2, 3,$ and 4 in this work. The oscillator energy, $\hbar\Omega$, is optimized to give the lowest energy for that state and model space. The effects of the Coulomb force and the spurious center-of-mass excitation are not considered at the moment. The MCSM results are compared with those of FCI, which gives the exact results in the chosen single-particle model space. The FCI results are obtained by the MFDn code, and the MCSM results by the newly developed code [1, 2]. We extrapolate the MCSM results by using the energy variance [6], which was discussed in Sect.3. Both in the MCSM and FCI calculations, we use the JISP16 NN interaction.

The binding energies obtained by MCSM and FCI are compared in Fig. 2. The MCSM results are extrapolated by the energy variance with the second-order polynomials. The differences between them are around a few tens of keV at most, and cannot be recognized at the energy scale of the figure. The binding energies of ^{10}B (1^+ , 3^+) and ^{12}C (0^+) are obtained by MCSM. These calculations exceed the

current computational limitation of FCI.

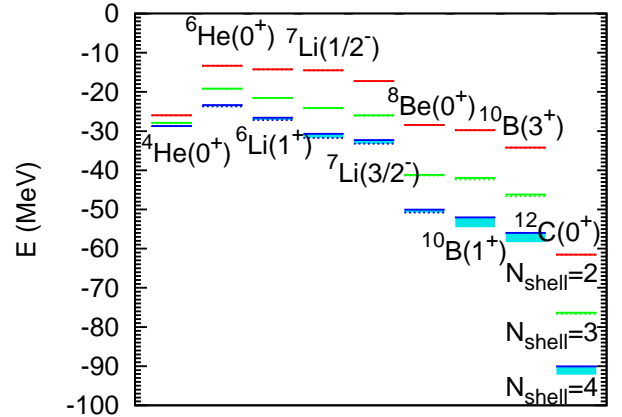


Figure 2. (Color online) Comparison of the ground- and some excited-state energies between the MCSM and FCI. The results of the MCSM without the extrapolation (FCI) are shown as the solid (dashed) lines. The extrapolations of the MCSM results are described by the bands. From top to bottom, the truncation of the model space is $N_{\text{shell}} = 2$ (red), 3 (green), and 4 (blue). Note that all of the results for ^{10}B and ^{12}C at $N_{\text{shell}} = 4$ were obtained only by MCSM. See Ref. [9] for details.

References

- [1] N. Shimizu, Y. Utsuno, T. Abe and T. Otsuka, RIKEN Accel. Prog. Rep. **43**, 319 (2010).
- [2] Y. Utsuno, N. Shimizu, T. Otsuka and T. Abe, RIKEN Accel. Prog. Rep. **44**, (2011) in press.
- [3] Grant-in-Aid for Scientific Research (20244022) from the Ministry of Education, Science, Sport, Culture and Technology.
- [4] For a review, T. Otsuka, M. Honma, T. Mizusaki, N. Shimizu and Y. Utsuno, Prog. Part. Nucl. Phys. **47**, 319 (2001).
- [5] T. Mizusaki and M. Imada, Phys. Rev. C **65**, 064319 (2002); **67**, 041301 (2003).
- [6] N. Shimizu, Y. Utsuno, T. Mizusaki, T. Otsuka, T. Abe and M. Honma, Phys. Rev. C **82** 061305(R) (2010).
- [7] T. Mizusaki, N. Shimizu, Y. Utsuno, and M. Honma, unpublished.
- [8] N. Shimizu, Y. Utsuno, T. Mizusaki, T. Otsuka, T. Abe and M. Honma, AIP Conf. Proc. **1355**, 167 (2011).
- [9] T. Abe, P. Maris, T. Otsuka, N. Shimizu, Y. Utsuno and J.P. Vary, AIP Conf. Proc. **1355**, 173 (2011).

Gamow-Teller Strengths in Ni Isotopes and Electron Capture Reactions

T. Suzuki, M. Honma^a, and T. Otsuka^{b,c}

Department of Physics, College of Humanities and Sciences, Nihon University

^a*Center for Mathematical Sciences, University of Aizu*

^b*Center for Nuclear Study, Graduate School of Science, University of Tokyo*

^c*National Superconducting Cyclotron Laboratory, Michigan State University, East Lansing, Michigan, 48824, USA*

Electron capture reactions play the most essential roles in the core-collapse processes at the last stage in the life cycle of stars. Accurate evaluations of the electron capture rates at high temperature and density are quite important to determine the initial conditions for the nucleosynthesis in supernova explosions.

Gamow-Teller (GT) transition strength in Ni isotopes is studied by shell model calculations with use of a new Hamiltonian in fp -shell, GXPF1J [1]. The GT strengths obtained are used to evaluate electron capture rates at stellar environments [2]. Calculated sum of GT strength for ^{58}Ni and ^{60}Ni is shown in Fig. 1, together with the experimental data [3,4] for comparison. The calculated sum of the GT strengths obtained by GXPF1J are in fair agreement with the experimental data for both ^{58}Ni and ^{60}Ni . Calculated electron capture rates for ^{58}Ni and ^{60}Ni are shown in Figs. 2 and 3, respectively.

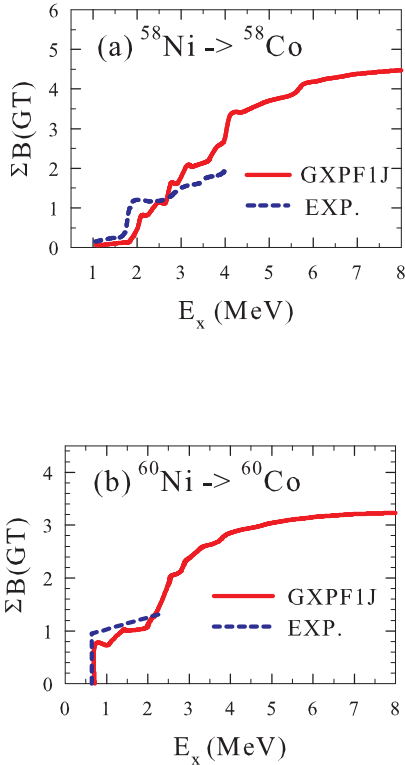


Figure 1. The sum of GT strengths in (a) ^{58}Ni and (b) ^{60}Ni up to the excitation energies (E_x) of ^{58}Co and ^{60}Co , respectively. Experimental data are taken from Refs. [3,4].

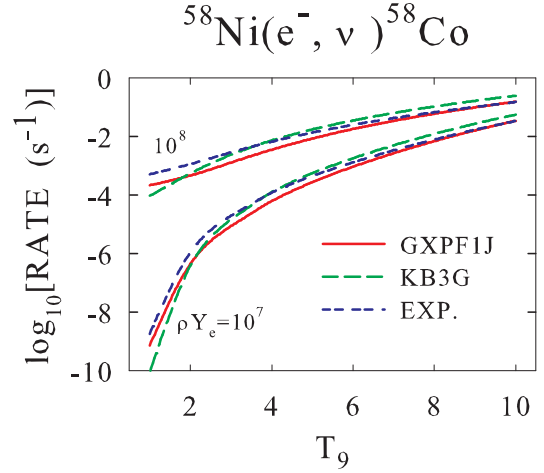


Figure 2. Electron capture rates on ^{58}Ni obtained for GXPF1J and KB3G [5] as well as those obtained by experimental GT strength [3].

The calculated capture rates in ^{58}Ni and ^{60}Ni are found to reproduce well the rates obtained using the experimental GT strengths [3,4]. As we see from Fig. 2 for ^{58}Ni , the calculated rates with GXPF1J are close to those using the experimental data at high T_9 , and reproduce well the temperature dependence of the rates with the experimental data at low T_9 . In case of ^{60}Ni , better evaluations of the capture rates have been obtained with GXPF1J compared with the rates using KB3G [5] as shown in Fig. 3.

The capture rates for ^{56}Ni , and neutron-rich ^{62}Ni and ^{64}Ni isotopes as well as Co and Mn isotopes are also investigated, and compared with previous results [6].

The GT strengths calculated using GXPF1J are generally more fragmented compared to those calculated with conventional Hamiltonians such as KB3G. In the study of neutrino-nucleus reactions on ^{56}Ni induced by supernove neutrinos, the reaction cross section for proton emission channel is found to be enhanced due to considerable GT strength in ^{56}Ni remaining at high excitation energies in case of GXPF1J. This enhancement is pointed out to lead to the enhancement of the production yield of ^{55}Mn in population III stars [7].

The calculated capture rates for ^{56}Ni are shown in Fig. 4 in case of GXPF1J and KB3G. The capture rates with GXPF1J are reduced by about 30% at high T due to larger

- [7] T. Suzuki et al., Phys. Rev. C **79** (2009) 061603(R).
 [8] T. Suzuki, M. Honma, T. Yoshida, H. Mao, T. Kajino and T. Otsuka Prog. Part. Nucl. Phys. **66** (2011) 385.

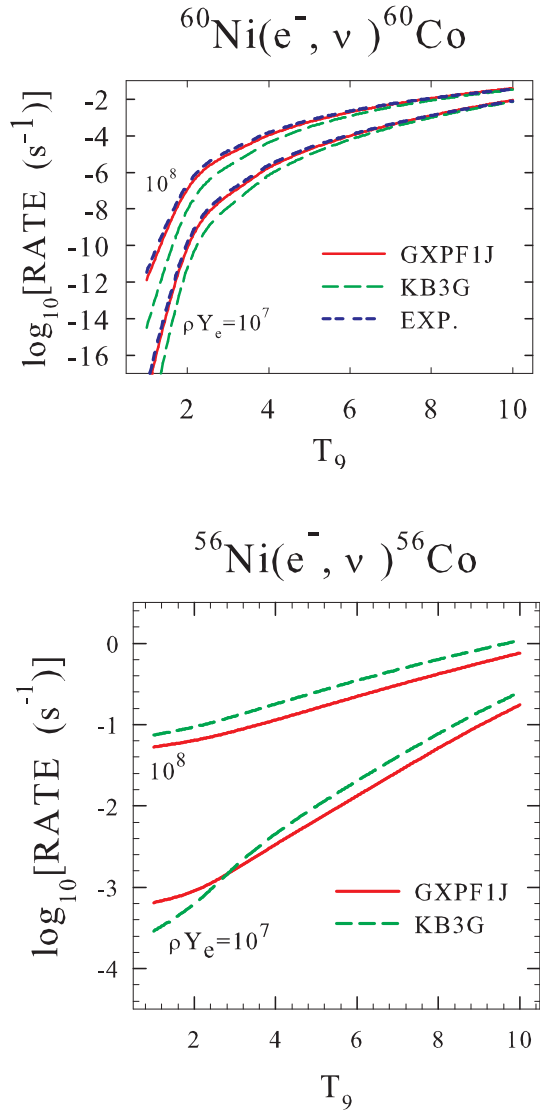


Figure 4. Calculated capture rates for ^{56}Ni obtained by GXPF1J and KB3G.

spreading of the GT strength. It would be quite interesting to measure the GT strength in ^{56}Ni .

The capture rates for neutron-rich ^{62}Ni and ^{64}Ni isotopes as well as Co and Mn isotopes are also investigated [2, 8], and compared with previous results [6].

References

- [1] M. Honma et al., J. Phys. Conf. Ser. **20** (2005) 7; Phys. Rev. C **65** (2002) 061301(R); **69** (2004) 034335.
 [2] T. Suzuki, M. Honma, H. Mao, T. Otsuka and T. Kajino, Phys. Rev. C **83** (2011) 044619.
 [3] M. Hagemann et al., Phys. Lett. **B579** (2004) 251.
 [4] N. Anantaraman et al., Phys. Rev. C **78** (2008) 065803.
 [5] E. Caurier et al., Rev. Mod. Phys. **77** (2005) 427.
 [6] K. Langanke and G. Martinez-Pinedo, Nucl. Phys. **A673** (2000) 481.

Symplectic structure and monopole strength in ^{12}C

T. Yoshida^a, N. Itagaki^b and K. Katō^c

^aCenter for Nuclear Study, Graduate School of Science, University of Tokyo

^bYukawa institute for Theoretical Physics, Kyoto University

^cDivision of Physics, Graduate School of Science, Hokkaido University

1. Introduction

From recent experimental [1] and theoretical studies [2–4], the existence of large monopole ($E0$) strengths for light nuclei has been discussed. From theoretical analysis, it has been suggested that the $E0$ strength is a measure for α cluster structure. This mechanism is understood based on so-called Bayman-Bohr theorem [2]. The theorem is interpreted that the shell model like ground state has a seed of various α cluster configuration that is easily excited by monopole transition operator [3]. We expect that the important concept to understand the relation between $E0$ strength and α cluster structure is symplectic algebra [5]. Historically, the symplectic model has been first used in the shell model calculation incorporated with the collective excitation mode. The similar sp structure is deduced in the microscopic α cluster model which is related to the α cluster relative motion [6]. They found that the probabilities of sp structure is large for some light nuclei. From these studies, it is reasonable to assume the close relation between symplectic structure and α cluster structure. We focus on the special version of sp structure ($Sp(2, R)_z$) for the study of the mechanism to generate the large $E0$ strength in ^{12}C . The states classified by this algebra can be raised to the $2\hbar\omega$ higher state by symplectic generators. We investigate that this large matrix element remains with coherent contributions based on the α cluster model calculation.

2. Formulation

In our study, we use $SU(3)$ α cluster model. It is advantageous that the model space is suited for the description both for the weakly binding α cluster states [7] (weak angular momentum coupling) or states which have geometrical shape such as linear-chain (l.c.) and triangular ones (strong angular momentum coupling) at the same time. In the present stage, we report the analysis for the three α cluster model. The $SU(3)$ model wave function is denoted by $V_{N_1, N_2}^{N(\lambda, \mu)J, \kappa}(\vec{r}, \vec{R})$, where $\lambda = N_z - N_y$, $\mu = N_y$ are evaluated from the total harmonic oscillator quanta for each direction and κ shows the ortho-normalized K quantum number for the intrinsic frame work. The selection of the Pauli allowed states can be performed by applying orthogonality condition model (OCM) [8, 9]. In the $SU(3)$ cluster model, it corresponds to the choice of the appropriate amplitude for $SU(3)$ (λ, μ) quanta as follows.

$$U_i(\vec{r}, \vec{R}) = \sum_{N_1 + N_2 = N} A_{N_1, N_2}^{(\lambda, \mu)\rho} V_{N_1, N_2}^{N(\lambda, \mu)J, \kappa}(\vec{r}, \vec{R}),$$

where i denotes $(\lambda, \mu)\rho, J, \kappa$ quanta. The ρ shows the Pauli allowed state. The label is given by imposing orthogonality condition to the Pauli forbidden states that is constructed

from other different Jacobi-coordinates. These model space is naturally truncated by the maximum harmonic oscillator quanta N_{max} . However the model space become large, when N_{max} increases due to the increase of ρ quanta. Therefore, we convert it to the basis state as follows,

$$w_\alpha(\vec{r}, \vec{R}) = \sum_{\rho} C_{\rho}^{\Lambda} U_i(\vec{r}, \vec{R}),$$

which is convenient for both the strong and weak coupling states in which the large N_{max} is needed. Here, the coefficients C_{ρ}^{Λ} and the quantum number Λ are obtained as eigenvectors and eigenvalues of the Casimir operator of $Sp(2, R)_z$ [10]. As shown below this model description is also suited for the analysis for $E0$ value. We notice that the interactions here are effective two α and inter three α interaction [11].

3. Result

We have checked that the good energy convergence is obtained with $N_{max}=100$ model space. Three lowest Λ -band states for each μ quanta are sufficient for the energy convergence. Even when we fit the parameter only for the ground band states, the energy spectra have good correspondence with the experiment around three α threshold. For instance, we obtain the 0_2^+ (Hoyle) state as a final state (energy $E_f=0.96$ MeV from the three α threshold), which is in reasonable region. The N -distribution of each state is shown in Fig. 1 and Fig. 2. Here, the red bar shows $\Lambda = 5/2$ component and blue one shows the total value (we label them as α_0 and α , respectively). Clearly, the ground state is dominated by α_0 configuration. For the 0_2^+ state, α_0 ranges to $N \sim 60$ which is consistent with the gas-like picture.

We also confirm that $E0(g.s. \rightarrow 0_2^+) = 5.9 \text{ fm}^2$ has good correspondence with the experiments ($5.4 \pm 0.2 \text{ fm}^2$). When Λ and $E0$ values for many other 0^+ state up to 20 MeV are compared, we find that the calculated $E0$ value and component of Λ -band states are closely related. The reason is that the ground state has α_0 dominance and $E0$ has a tendency to conserve Λ value. The overall $E0$ values can be understood by Λ strength. However, this does not assure that the large value always remains when configuration changes within the same Λ .

As a next step, we show importance of α_0 components and N distribution of final states to generate $E0$ strength [12]. We take overlap of the ground state and the final state multiplied by $E0$ operator for a specific N value of the final state. In Fig. 3, the result for the 0_2^+ state is shown. We can see the coherent contribution of α_0 around $N = 20 - 40$ makes large $E0$ value. Some of 0^+ states including linear-chain (l.c.) ($E_f = 5.12$) state have this mechanism. Contrary to this, some continuum 0^+ states ($E_f = 17.2$ etc.)

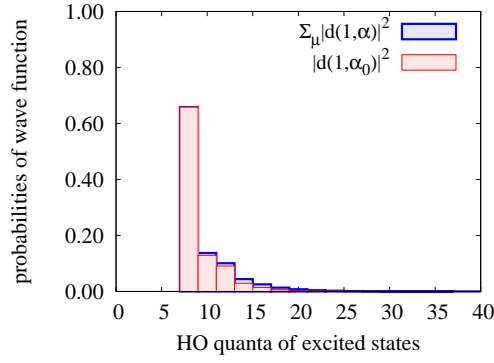


Figure 1. The N -quanta distribution of ground state for ^{12}C ($E_f = -7.29$ MeV).

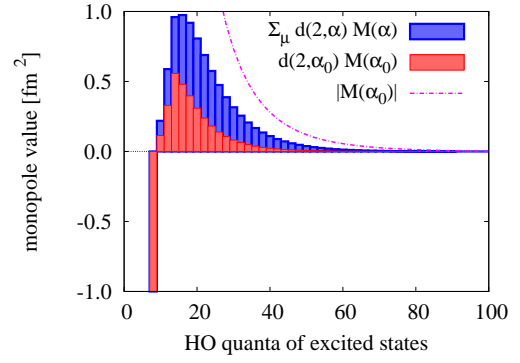


Figure 3. The N -quanta distribution of the excited state in $E0$ transition strength for ^{12}C ($E_f = 0.96$ MeV).

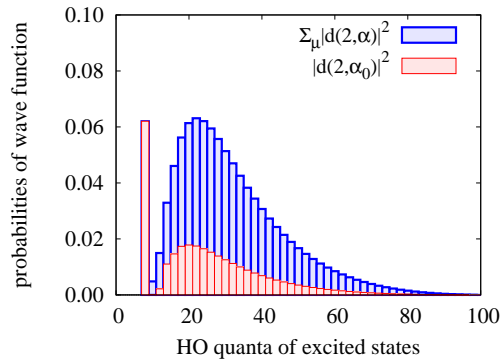


Figure 2. The N -quanta distribution for ^{12}C ($E_f = 0.96$ MeV).

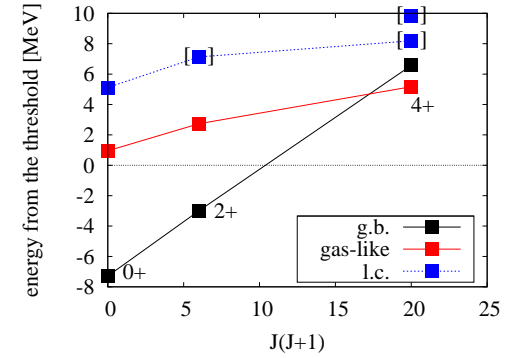


Figure 4. The band structure of positive parity ^{12}C are shown.

have cancellation mechanism where the final state contributions to $E0$ values oscillate with respect to N . As a result, the total $E0$ value is sensitive to the boundary condition.

We summarize the properties of the wave function around these energy region. The band structure of each state is shown in Fig. 4, where ground band states are shown with the black dots. The red dots are the states which have gas-like properties. For instance, the r.m.s. radius for the 0_2^+ state is 3.61 fm and the probabilities of (λ, μ) quanta are widely distributed, which is consistent with gas-like picture. The blue dots show the l.c. properties. For instance, $\mu = 0$ contribution (pure l.c. structure) occupies 45% of the wave function for 0^+ ($E_f = 5.12$ MeV) state. The dots with the parentheses show the state which have continuum properties. Here, the gas-like and l.c. 0^+ states have rapid energy convergence compared to the other continuum states, which indicate the shape resonant states. The existence of gas-like 2^+ state is also supported by N -convergence behaviors.

4. Summary

In this article, the importance of $Sp(2, R)_z$ has been discussed. Firstly, we show that the Λ -bands effectively describe the excited states of ^{12}C which correspond to the gas-like or l.c. structure. To describe such kind of states, the model space within three lowest Λ -bands for each μ is large enough for the states up to 20 MeV. The α_0 components ($\Lambda = 5/2$) which is the same as the ground state are found to be important for the overall behavior of $E0$ strength. The detailed behavior of $E0$ strength is related to the coherent contribution of α_0 . The properties of each state

are discussed with the band-structure. We can specify the gas-like and l.c. structure of 0^+ . To confirm the width, we must treat the boundary condition correctly in future works.

References

- [1] T. Kawabata *et al.*, Phys. Lett. B, **646**, 6 (2007).
- [2] B. F. Bayman and A. Bohr, Nucl. Phys. **9**, 596 (1959).
- [3] T. Yamada *et al.*, Prog. Theor. Phys. **120**, 6 (2008).
- [4] T. Yoshida, N. Itagaki and T. Otsuka, Phys. Rev. C **79**, 034308 (2009).
- [5] F. Arickx, Nucl. Phys. A **268**, 347 (1976).
- [6] Y. Suzuki, *et al.*, Phys. Rev. C **54**, 2073 (1996).
- [7] A. Tohsaki *et al.*, Phys. Rev. Lett. **87**, 192501 (2001).
- [8] S. Saitō, Prog. Theor. Phys. **41**, 705 (1969).
- [9] H. Horiuchi, Prog. Theo. Phys. **58**, 204 (1989).
- [10] K. Katō and H. Tanaka, Prog. Theor. Phys. **81**, 841 (1989).
- [11] C. Kurokawa *et al.*, Nucl. Phys. A **792**, 87 (2007).
- [12] T. Yoshida, N. Itagaki and K. Katō, Phys. Rev. C **83**, 024301 (2011).

Other Activities

The 9th CNS-EFES Summer School(CNS-EFES10)

S. Ota, S. Michimasa, N. Aoi^a, S. Fujii^b, H. Hamagaki, S. Kubono, S. Michimasa, T. Nakatsukasa^a,
T. Otsuka, H. Sakai^a, S. Shimoura, T. Suzuki^c *Center for Nuclear Study, Graduate School of Science,*

University of Tokyo

^a*Nishina Center for Accelerator-Based Science, RIKEN*

^b*Department of Physics, the University of Tokyo*

^c*Department of Physics, Nihon University*

The 9th CNS-EFES International Summer School (CNS-EFES10) was organized jointly by the Center for Nuclear Study (CNS), the University of Tokyo, and the Japan Society for the Promotion of Science (JSPS) Core-to-Core Program “ International Research Network for Exotic Femto Systems (EFES) ”, in the period of Aug 18-24, 2009. The summer school was held at the Nishina hall in the Wako campus of RIKEN and at the Koshiba hall in the Hongo campus, the University of Tokyo. This summer school was the ninth one in the series which aimed at providing graduate students and postdocs with basic knowledge and perspectives of nuclear physics. It consisted of lectures by leading scientists in the fields of both experimental and theoretical nuclear physics. Each lecture started with an introductory talk from the fundamental point of view and ended with up-to-date topics in the relevant field. The lecturers and the lecture titles are listed below.

- **K. Langanke (GSI, Germany)**, “Selected topic in Nuclear Astrophysics”
- **A. Vitturi (Padova, Italy)**, “Nuclear structure effects in heavy-ion reactions involving systems far from stability”
- **W. Lynch (MSU, US)**, “Constraining the properties of dense matter”
- **J. Dobaczewski (Warsaw, Poland)**, “Density functional theory and energy density functionals in nuclear physics”
- **J. Meng (Peking, China)**, “Covariant Density Functional Theory -applications in nuclear physics and astrophysics”
- **S. Chiba (JAEA, Japan)**, “Nuclear Physics Contributions to Nuclear Energy”
- **K. Yoneda (RIKEN, JAPAN)**, “A New Spectrometer in RIBF – SAMURAI –
- **H. Yamaguchi (CNS, JAPAN)**, “Recent experimental studies on nuclear astrophysics at CRIB”

This year, 110 participants, including 8 lecturers from 12 countries, attended the school. Three lecturers and 28 participants were from foreign institutes, and 8 participants were foreign researchers belonging to domestic institutes. Five lectures on Aug. 19 were held at the Koshiba hall in the Hongo campus and were broadcasted via the Inter- net. The

student and postdoc sessions were also held in the school. 25 talks and 28 posters were presented by graduate students and postdocs. Attendances communicated each other in the free discussion time between the lectures and in the welcome and farewell parties with a relaxed atmosphere. All information concerning the summer school is open for access at the following URL:

[http://indico.cns.s.u-tokyo.ac.jp/
conferenceDisplay.py?confId=25](http://indico.cns.s.u-tokyo.ac.jp/conferenceDisplay.py?confId=25)

This summer school was supported in part by the International Exchange Program of the Graduate School of Science, the University of Tokyo. The financial support was indispensable to organize this summer school successfully. The organizers deeply appreciate various accommodations provided by RIKEN Nishina center for the school. They are also grateful to administration staffs of the CNS and the Graduate School of Science for their helpful supports. They thank graduate students and postdocs in the CNS for their dedicated efforts. Finally, the organizers acknowledge all the lecturers and participants for their contributions to this summer school.

Laboratory Exercise for Undergraduate Students

S. Ota, S. Michimasa, H. Yamaguchi, A. Takaki^a, M. Takaki, K. Ozawa^a and S. Shimoura

Center for Nuclear Study, Graduate School of Science, University of Tokyo

^a*Department of Physics, University of Tokyo*

Nuclear scattering experiments were performed as a laboratory exercise for undergraduate students of the University of Tokyo. This program was aiming at providing undergraduate students with an opportunity to learn how to study subatomic physics by using an ion beam from an accelerator. In 2010, 32 students joined this program.

The four beam times were scheduled in the second semester for third-year students, and 8 students participated in each beam time. The experiment was performed at the RIBF using a 26-MeV alpha beam accelerated by the AVF cyclotron. The alpha beam extracted from the AVF cyclotron was transported to the E7B beam line in the E7 experimental hall. A newly developed scattering chamber was installed at the E7B course in order to perform the experiment efficiently. A photo is shown in Fig. 1 In each beam time, the students were divided into two groups and took one of the following two subjects:

1. Size of a nucleus through the measurement of elastic scattering on ^{197}Au .
2. Deformation of nuclei through the measurement of gamma rays emitted in the cascade decay of highly excited ^{154}Gd and ^{184}Os .



Figure 1. Newly developed scattering chamber located at the E7B course in E7 experimental room

Before the experiment, the students learned the basic handling of the semiconductor detectors and electronic circuits at the Hongo campus, and attended a radiation safety lecture at RIKEN. They also joined a tour to the RI beam factory at RIKEN.

In the $\alpha+^{197}\text{Au}$ measurement, α particles scattered from the Au target with a thickness of 1.42 mg/cm^2 were detected by a silicon PIN-diode located 11 cm away from the target. A collimator with a diameter of 6 mm was attached on the silicon detector. The energy spectrum of the scattered particles was recorded by a multi-channel analyzer (MCA) system. The beam was stopped by a Faraday cup in the scattering chamber. The cross section for the al-

pha elastic scattering was measured in the angular range of $\theta_{\text{lab}} = 25-160^\circ$.

The measured cross section was compared with the calculated cross section for the Rutherford scattering. The cross section was also analyzed by the potentialmodel calculation, and the radius of the gold nucleus was discussed. Some students obtained the radius of $\sim 10\text{ fm}$ by using a classical model where the trajectory of the α particle in the nuclear potential is obtained by the Runge-Kutta method. Others tried to understand the scattering process by calculating the angular distribution by the distorted wave Born approximation with a Coulomb wave function and a realistic nuclear potential.

In the measurement of the rotational bands, excited states in ^{154}Gd and ^{184}Os nuclei were populated by the $^{152}\text{Sm}(\alpha,2n)$ and $^{182}\text{W}(\alpha,2n)$ reactions, respectively. The gamma rays emitted from the cascade decay of the rotational bands were measured by a high purity germanium detector located 50 cm away from the target. The energies of the gamma rays were recorded by the MCA system. The gain and the efficiency of the detector system had been calibrated with standard gamma-ray sources of ^{22}Na , ^{60}Co , ^{133}Ba , and ^{137}Cs . The gamma rays from the $12+ \rightarrow 10+$ and $10+ \rightarrow 8+$ decay in ^{154}Gd and ^{184}Os were successfully identified. Based on the energies of the gamma rays, the moment of inertia and the deformation parameters of the excited states were discussed by using a classical rigid rotor model and a irrotational uid model. The students found that the reality lies between the two extreme models. The initial population among the levels in the rotational band was also discussed by taking the effect of the internal conversion into account.

We believe this program was very impressive for the students. It was the first time for most of the students to use large experimental equipments. They learned basic things about the experimental nuclear physics and how to extract physics from the data. The authors would like to thank Dr. Y. Uwamino, Prof. Y. Sakurai, the CNS accelerator group, and the RIBF cyclotron crew for their helpful effort in the present program.

Appendices

**Symposium, Workshop, Seminar, PAC and
External Review**

CNS Reports

Publication List

Talks and Presentations

Personnel

Symposium, Workshop, Seminar, Colloquium, and PAC

A. Symposium

1. 25th Anniversary of the Discovery of Halo Nuclei (Halo2010)

December 6–9, 2010, Hayama, Japan

The 25th anniversary of the discovery of significant neutron halo takes place this year. As a celebration of this occasion, the Halo2010 Symposium was held on the 6th-9th of December, 2010 by the Center for Nuclear Study (CNS), the University of Tokyo. The remarkable neutron-halo effect in ^{11}Li was observed in the first measurement of the nuclear radii of light neutron-rich nuclei by means of secondary beams produced by projectile fragmentation of a high-energy heavy-ion beam. It has opened a new era of the study of nuclei far from the stability. This experiment was performed in Berkeley under the US-Japan collaboration conducted by the Institute of Nuclear Study, the University of Tokyo. The INS has been transformed, and the relevant part has become the CNS.

The Halo2010 Symposium was devoted to review various experimental and theoretical progresses in the fields of physics of drip-line nuclei and to discuss future perspectives initiated by 3rd generation RI beam facilities. 64 researchers, including 18 persons from outside of Japan participated to the symposium. The symposium was hosted by CNS.

Topics: Nuclear Radii/Charge Radii, Mass Measurements, Nuclear Moments, Momentum Distribution, Beta Decay, Charge Exchange Reactions, Electro-Magnetic Responses, Spectroscopy of Loosely-Bound and/or Unbound System, Di-Neutron Correlation/Few Neutron System/Neutron Matter, Interaction and Structure in Dripline Nuclei, Reaction Mechanism for Dripline Nuclei, Neutron-Rich Hypernuclei

Local Organizer: S. Shimoura (Chair), H. Hamagaki (CNS), T. Nakatsukasa (RNC), T. Otsuka (Tokyo/CNS), H. Sakurai (RNC), S. Michimasa (CNS, Secretary)

B. Workshop

1. OMEG Institute on SNe and the r-process
July 15, 2010, RIKEN, Japan
2. OMEG Institute on the $^{12}\text{C}(\alpha, \gamma)^{16}\text{O}$ reaction rate
November 1, 2010, RIKEN, Japan
3. Workshop on Impact of new triple- α reaction rate on stellar evolution and nucleosynthesis
December 17-18, 2010, RIKEN, Japan

C. CNS Seminar

1. “Development of diamond detectors for heavy ion beam tracking”, A. Stolz (NSCL, MSU), Apr. 22, 2010.
2. “Some Aspects of the Structure of Exotic Nuclei”, Augusto O. Macchiavelli (Lawrence Berkeley National Laboratory), Sep. 16, 2010.
3. “Uncertainties in the nu p-process: supernova dynamics vs. nuclear physics”, S. Wanajo (TUM/MPA), Oct. 29, 2010.

E. Program Advisory Committee for Nuclear-Physics Experiments at RI Beam Factory

1. The 7th Program Advisory Committee (NP-PAC) meeting for Nuclear Physics Experiments at RI Beam Factory
Date: June 14-15, 2010 Place: Conference room, 2F RIBF building
2. The 8th Program Advisory Committee (NP-PAC) meeting for Nuclear Physics Experiments at RI Beam Factory
Date: December 3-5, 2010 Place: Conference room, 2F RIBF building

CNS Reports

- #84** “Analyzing power for the proton elastic scattering from neutron-rich ${}^6\text{He}$ nucleus”
T. Uesaka, S. Sakaguchi, Y. Iseri, K. Amos, N. Aoi, Y. Hashimoto, E. Hiyama, M. Ichikawa, Y. Ichikawa, S. Ishikawa, K. Itoh, M. Itoh, H. Iwasaki, S. Karataglidis, T. Kawabata, T. Kawahara, H. Kuboki, Y. Maeda, R. Matsuo, T. Nakao, H. Okamura, H. Sakai, Y. Sasamoto, M. Sasano, Y. Satou, K. Sekiguchi, M. Shinohara, K. Suda, D. Suzuki, Y. Takahashi, M. Tanifuji, A. Tamii, T. Wakui, K. Yako, Y. Yamamoto, and M. Yamaguchi July, 2010
- #85** “Simple, High-Sensitive and Non-Destructive Beam Monitor for RI Beam Facilities”
S.Watanabe S.Kubono Y.Ohshiro H. Yamaguchi M,Kase M.Wada R.koyama Dec.2010
- #86** “CNS Annual Report 2009”
Edited by T. Gunji Feb.2011
- #87** “Alpha resonance structure in ${}^{11}\text{B}$ studied via resonant scattering of ${}^7\text{Li}+\alpha$ ” H. Yamaguchi, T. Hashimoto, S. Hayakawa, D.N. Binh, D. Kahl, S. Kubono, Y. Wakabayashi, T. Kawabata and T. Teranishi, Feb. 2011

Publication List

A. Original Papers

1. T. Uesaka, S. Sakaguchi, Y. Iseri, K. Amos, N. Aoi, Y. Hashimoto, E. Hiyama, M. Ichikawa, Y. Ichikawa, S. Ishikawa, K. Itoh, M. Itoh, H. Iwasaki, S. Karataglidis, T. Kawabata, T. Kawahara, H. Kuboki, Y. Maeda, R. Matsuo, T. Nakao, H. Okamura, H. Sakai, Y. Sasamoto, M. Sasano, Y. Satou, K. Sekiguchi, M. Shinohara, K. Suda, D. Suzuki, Y. Takahashi, M. Tanifuji, A. Tamii, T. Wakui, K. Yako, Y. Yamamoto, and M. Yamaguchi, “Analyzing power for the proton elastic scattering from neutron-rich ${}^6\text{He}$ nucleus”, *Physical Review* **C822** (2010) 021602(R).
2. E. Ideguchi, S. Ota, T. Morikawa, M. Oshima, M. Koizumi, Y. Toh, A. Kimura, H. Harada, K. Furutaka, S. Nakamura, F. Kitatani, Y. Hatsukawa, T. Shizuma, M. Sugawara, H. Miyatake, Y.X. Watanabe, Y. Hirayama, M. Oi: “Superdeformation in asymmetric $N > Z$ nucleus ${}^{40}\text{Ar}$ ”, *Phys. Lett. B* **686** (2010) 18–22.
3. H. Baba, T. Ichihara, T. Ohnishi, S. Takeuchi, K. Yoshida, Y. Watanabe, S. Ota, S. Shimoura: “New Data Acquisition System for the RIKEN Radioactive Isotope Beam Factory”, *Nucl. Instrum. Methods. A* **616** (2010) 65–68
4. Y. Kondo, T. Nakamura, Y. Satou, T. Matsumoto, N. Aoi, N. Endo, N. Fukuda, T. Gomi, Y. Hashimoto, M. Ishihara, S. Kawai, M. Kitayama, T. Kobayashi, Y. Matsuda, N. Matsui, T. Motobayashi, T. Nakabayashi, T. Okumura, H.J. Ong, T.K. Onishi, K. Ogata, H. Otsu, H. Sakurai, S. Shimoura, M. Shinohara, T. Sugimoto, S. Takeuchi, M. Tamaki, Y. Togano, Y. Yanagisawa: “Low-lying intruder state of the unbound nucleus ${}^{13}\text{Be}$ ”, *Phys. Lett. B* **690**, 245–249 (2010).
5. Y. Satou, T. Nakamura, Y. Kondo, N. Matsui, Y. Hashimoto, T. Nakabayashi, T. Okumura, M. Shinohara, N. Fukuda, T. Sugimoto, H. Otsu, Y. Togano, T. Motobayashi, H. Sakurai, Y. Yanagisawa, N. Aoi, S. Takeuchi, T. Gomi, M. Ishihara, S. Kawai, H.J. Ong, T.K. Onishi, S. Shimoura, M. Tamaki, T. Kobayashi, Y. Matsuda, N. Endo, M. Kitayama: “ ${}^{14}\text{Be}(p, n){}^{14}\text{B}$ reaction at 69 MeV in inverse kinematics”, *Phys. Lett. B* **697** 459–462 (2011).
6. S. Nishimura, Z. Li, H. Watanabe, K. Yoshinaga, T. Sumikama, T. Tachibana, K. Yamaguchi, M. Kurata-Nishimura, G. Lorusso, Y. Miyashita, A. Odahara, H. Baba, J.S. Berryman, N. Blasi, A. Bracco, F. Camera, J. Chiba, P. Doornenbal, S. Go, T. Hashimoto, S. Hayakawa, C. Hinke, E. Ideguchi, T. Isobe, Y. Ito, D.G. Jenkins, Y. Kawada, N. Kobayashi, Y. Kondo, R. Krucken, S. Kubono, T. Nakano, H. Sakurai, H. Scheit, K. Steiger, D. Steppenbeck, K. Sugimoto, H.J. Ong, S. Ota, Zs. Podolyak, S. Takano, A. Takashima, K. Tajiri, T. Teranishi, Y. Wakabayashi, P.M. Walker, O. Wieland, H. Yamaguchi: “ β -Decay Half-Lives of Very Neutron-Rich Kr to Tc Isotopes on the Boundary of the r-Process Path: An Indication of Fast r-Matter Flow”. *Phys. Rev. Lett.* **106**, 052502 (2011).
7. H. Watanabe, T. Sumikama, S. Nishimura, K. Yoshinaga, Z. Li, Y. Miyashita, K. Yamaguchi, H. Baba, J.S. Berryman, N. Blasi, A. Bracco, F. Camera, J. Chiba, P. Doornenbal, S. Go, T. Hashimoto, S. Hayakawa, C. Hinke, E. Ideguchi, T. Isobe, Y. Ito, D.G. Jenkins, Y. Kawada, N. Kobayashi, Y. Kondo, R. Krucken, S. Kubono, G. Lorusso, T. Nakano, M. Kurata-Nishimura, A. Odahara, H.J. Ong, S. Ota, Zs. Podolyak, H. Sakurai, H. Scheit, Y. Shi, K. Steiger, D. Steppenbeck, K. Sugimoto, K. Tajiri, S. Takano, A. Takashima, T. Teranishi, Y. Wakabayashi, P.M. Walker, O. Wieland, F.R. Xu, H. Yamaguchi: “Low-lying level structure of the neutron-rich nucleus ${}^{109}\text{Nb}$: A possible oblate-shape isomer”, *Phys. Lett. B* **696**, 186–190 (2011).
8. T. Ohnishi, T. Kubo, K. Kusaka, A. Yoshida, K. Yoshida, M. Ohtake, N. Fukuda, H. Takeda, D. Kameda, K. Tanaka, N. Inabe, Y. Yanagisawa, Y. Gono, H. Watanabe, H. Otsu, H. Baba, T. Ichihara, Y. Yamaguchi, M. Takechi, S. Nishimura, H. Ueno, A. Yoshimi, H. Sakurai, T. Motobayashi, T. Nakao, Y. Mizoi, M. Matsushita, K. Ieki, N. Kobayashi, K. Tanaka, Y. Kawada, N. Tanaka, S. Deguchi, Y. Satou, Y. Kondo, T. Nakamura, K. Yoshinaga, C. Ishii, H. Yoshii, Y. Miyashita, N. Uematsu, Y. Shiraki, T. Sumikama, J. Chiba, E. Ideguchi, A. Saito, T. Yamaguchi, I. Hachiuma, T. Suzuki, T. Moriguchi, A. Ozawa, T. Ohtsubo, M.A. Famiano, H. Geissel, A.S. Nettleton, O.B. Tarasov, D.P. Bazin, B.M. Sherrill, S.L. Manikonda, J.A. Nolen: “Identification of 45 New Neutron-Rich Isotopes Produced by In-Flight Fission of a ${}^{238}\text{U}$ Beam at 345 MeV/nucleon”, *J. Phys. Soc. Jpn.* **79**, 073201 (2010).
9. D. Rudolph, I. Ragnarsson, W. Reviol, C. Andreoiu, M.A. Bentley, M.P. Carpenter, R.J. Charity, R.M. Clark, M. Cromaz, J. Ekman, C. Fahlander, P. Fallon, E. Ideguchi, A.O. Macchiavelli, M.N. Mineva, D.G. Sarantites, D. Seweryniak, S.J. Williams: “Rotational bands in the semi-magic nucleus ${}^{57}_{28}\text{Ni}_{29}$ ”, *J. Phys. G* **37**, 075105 (2010).
10. Y. Taniguchi, Y. Kanada-Enyo, M. Kimura, K. Ikeda, H. Horiuchi, E. Ideguchi: “Triaxial superdeformation in ${}^{40}\text{Ar}$ ”, *Phys. Rev. C* **82**, 011302 (2010).

11. H. Baba, T. Ichihara, T. Ohnishi, S. Takeuchi, K. Yoshida, Y. Watanabe, S. Ota, S. Shimoura: "New data acquisition system for the RIKEN Radioactive Isotope Beam Factory", Nucl. Instrum. Methods Phys. Res. **A616**, 65–68 (2010).
12. A. Kim, N. H. Lee, I. S. Hahn, J. S. Yoo and M. H. Han, S. Kubono, H. Yamaguchi, S. Hayakawa, Y. Wakabayashi, D. N. Binh, H. Hashimoto, T. Kawabata, D. Kahl, Y. Kurihara, Y. K. Kwon, T. Teranishi, S. Kato, T. Komatsubara, B. Guo, G. Bing, W. P. Liu and Y. Wang : "Direct Measurement of the $^{14}\text{O}(\alpha,p)^{14}\text{O}$ Cross Section for Astrophysically Important $^{14}\text{O} + \alpha$ Resonances", J. Korean Phys. Soc., *57* (2010) 40 - 43
13. K. Setoodehnia, A. A. Chen, T. Komatsubara, S. Kubono, D. N. Binh, J. F. Carpino, J. Chen, T. Hashimoto, T. Hayakawa, Y. Ishibashi, Y. Ito, D. Kahl, T. Moriguchi, H. Ooishi, A. Ozawa, T. Shizuma, Y. Sugiyama, and H. Yamaguchi : "Spins and parities of astrophysically important ^{30}S states from $^{28}\text{Si}(3\text{He}, n\gamma)^{30}\text{S}$ ", Phys. Rev. C **83** (2011) 018803-4
14. S. Wanajo, H.-T. Janka, and S. Kubono: "Uncertainties in the μp -Process: Supernova Dynamics versus Nuclear Physics", Astrophys. J. *729* (2011) 46
15. S. Watanabe, S. Kubono, Y. Ohshiro, H. Yamaguchi, M. Kase, M. Wada, R. Koyama: "Simple, High-Sensitive, and Non-Destructive Beam Monitor for RI Beam Facilities", Nucl. Instr. Meth. A *633* (2011) 8 - 14
16. T. Sumikama, K. Yoshinaga, H. Watanabe, S. Nishimura, Y. Miyashita, K. Yamaguchi, K. Sugimoto, J. Chiba, Z. Li, H. Baba, J. S. Berryman, N. Blasi, A. Bracco, F. Camera, P. Doornenbal, S. Go, T. Hashimoto, S. Hayakawa, C. Hinke, E. Ideguchi, T. Isobe, Y. Ito, D. G. Jenkins, Y. Kawada, N. Kobayashi, Y. Kondo, R. Krucken, S. Kubono, G. Lorusso, T. Nakano, M. Kurata-Nishimura, A. Odahara, H. J. Ong, S. Ota, Zs. Podolya ´k, H. Sakurai, H. Scheit, K. Steiger, D. Steppenbeck, S. Takano, A. Takashima, K. Tajiri, T. Teranishi, Y. Wakabayashi, P. M. Walker, O. Wieland, and H. Yamaguchi : "Structural Evolution in the Neutron-Rich Nuclei ^{106}Zr and ^{108}Zr ", Phys. Rev. Lett. *106* (2011) 202501
17. H. Watanabe, T. Sumikama, S. Nishimura, K. Yoshinaga, Z. Li, Y. Miyashita, K. Yamaguchi, H. Baba, J.S. Berryman, N. Blasi, A. Bracco, F. Camera, J. Chiba, P. Doornenbal, S. Go, T. Hashimoto, S. Hayakawa, C. Hinke, E. Ideguchi, T. Isobe, Y. Ito, D.G. Jenkins, Y. Kawada, N. Kobayashi, Y. Kondo, R. Krucken, S. Kubono, G. Lorusso, T. Nakano, M. Kurata-Nishimura, A. Odahara, H.J. Ong, S. Ota, Zs. Podolyak, H. Sakurai, H. Scheit, Y. Shi, K. Steiger, D. Steppenbeck, K. Sugimoto, K. Tajiri, S. Takano, A. Takashima, T. Teranishi, Y. Wakabayashi, P.M. Walker, O. Wieland, F.R. Xu, H. Yamaguchi : "Low-lying level structure of the neutron-rich nucleus ^{109}Nb : A possible oblate-shape isomer", Phys. Lett. B *696* (2011) 186
18. H. Yamaguchi, T. Hashimoto, S. Hayakawa, D. N. Binh, D. Kahl, S. Kubono Y. Wakabayashi, T. Kawabata, and T. Teranishi, " α resonance structure in ^{11}B studied via resonant scattering of $^7\text{Li}+\alpha$ ", Phys. Rev. C **83** (2011) 034306.
19. S. Nishimura, Z. Li, H. Watanabe, K. Yoshinaga, T. Sumikama, T. Tachibana, K. Yamaguchi, M. Kurata-Nishimura, G. Lorusso, Y. Miyashita, A. Odahara, H. Baba, J.S. Berryman, N. Blasi, A. Bracco, F. Camera, J. Chiba, P. Doornenbal, S. Go, T. Hashimoto, S. Hayakawa, C. Hinke, E. Ideguchi, T. Isobe, Y. Ito, D.G. Jenkins, Y. Kawada, N. Kobayashi, Y. Kondo, R. Kucken, S. Kubono, T. Nakano, H.J. Ong, S. Ota, Zs. Podolya ´k, H. Sakurai, H. Scheit, K. Steiger, D. Steppenbeck, K. Sugimoto, S. Takano, A. Takashima, K. Tajiri, T. Teranishi, Y. Wakabayashi, P.M. Walker, O. Wieland, and H. Yamaguchi, " β -Decay Half-Lives of Very Neutron-Rich Kr to Tc Isotopes on the Boundary of the r-Process Path: An Indication of Fast r-Matter Flow", Phys. Rev. Lett. **106**, (2011) 052502.
20. K. Aamodt et al. (ALICE Collaboration): "Strange particle production in proton-proton collisions at $\sqrt{s} = 0.9$ TeV with ALICE at the LHC", Eur. Phys. J. C *71*, 1594 (2011)
21. K. Aamodt et al. (ALICE Collaboration): "Two-pion Bose-Einstein correlations in central PbPb collisions at $\sqrt{s_{NN}} = 2.76$ TeV", Phys.Lett.B *696*:328-337,2011
22. K. Aamodt et al. (ALICE Collaboration): "Centrality dependence of the charged-particle multiplicity density at mid-rapidity in Pb-Pb collisions at $\sqrt{s_{NN}} = 2.76$ TeV" Phys. Rev. Lett. *106*, 032301 (2011)
23. K. Aamodt et al. (ALICE Collaboration): "Suppression of Charged Particle Production at Large Transverse Momentum in Central Pb-Pb Collisions at $\sqrt{s_{NN}} = 2.76$ TeV", Phys. Lett. B *696* (2011) 30-39
24. K. Aamodt et al. (ALICE Collaboration): "Elliptic flow of charged particles in Pb-Pb collisions at 2.76 TeV", Phys. Rev. Lett. *105*, 252302 (2010)

25. K. Aamodt et al. (ALICE Collaboration): “Charged-particle multiplicity density at mid-rapidity in central Pb-Pb collisions at $\sqrt{s_{NN}} = 2.76$ TeV”, Phys. Rev. Lett. 105, 252301 (2010)
26. K. Aamodt et al. (ALICE Collaboration): “Transverse momentum spectra of charged particles in proton-proton collisions at $\sqrt{s} = 900$ GeV with ALICE at the LHC”, Physics Letters B 693 (2010) 53–68
27. K. Aamodt et al. (ALICE Collaboration): “Two-pion Bose-Einstein correlations in pp collisions at $\sqrt{s} = 900$ GeV”, Phys. Rev. D 82, 052001 (2010)
28. K. Aamodt et al. (ALICE Collaboration): “Midrapidity Antiproton-to-Proton Ratio in pp Collisions at $\sqrt{s} = 0.9$ and 7 TeV Measured by the ALICE Experiment”, Phys Rev Lett Vol.105, No.7, (2010)
29. K. Aamodt et al. (ALICE Collaboration): “Charged-particle multiplicity measurement in proton-proton collisions at $\sqrt{s} = 7$ TeV with ALICE at LHC”, Eur. Phys. J. C (2010) 68: 345–354
30. K. Aamodt et al. (ALICE Collaboration): “Charged-particle multiplicity measurement in proton-proton collisions at $\sqrt{s} = 0.9$ and 2.36 TeV with ALICE at LHC”, Eur. Phys. J. C (2010) 68: 89–108
31. A. Adare et al., for the PHENIX Collaboration: “Azimuthal Correlations of Electrons from Heavy Flavor Decay with hadrons in Au+Au and p+p Collisions at $\sqrt{s} = 200$ GeV”, Phys. Rev. C 83, 044912 (2011)
32. A. Adare et al., for the PHENIX Collaboration: “Measurement of neutral mesons in p+p collisions at $\sqrt{s} = 200$ GeV and scaling properties of hadron production”, Phys. Rev. D 83, 052004 (2011)
33. A. Adare et al., for the PHENIX Collaboration: “Nuclear modification factors of phi mesons in d+Au, Cu+Cu and Au+Au collisions at $\sqrt{s_{NN}} = 200$ GeV”, Phys. Rev. C 83, 024909 (2011)
34. A. Adare et al., for the PHENIX Collaboration: “Cross Section and Parity Violating Spin Asymmetries of $W^{+/-}$ Boson Production in Polarized p+p Collisions at $\sqrt{s} = 500$ GeV”, Phys. Rev. Lett. 106, 062001 (2011)
35. A. Adare et al., for the PHENIX Collaboration: “Cross section and double helicity asymmetry for eta mesons and their comparison to neutral pion production in proton-proton collisions at $\sqrt{s} = 200$ GeV”, Phys. Rev. D 83, 032001 (2011)
36. A. Adare et al., for the PHENIX Collaboration: “Measurement of Transverse Single-Spin Asymmetries for J/ψ Production in Polarized p+p Collisions at $\sqrt{s} = 200$ GeV”, Phys. Rev. D 82, 112008 (2010)
37. A. Adare et al., for the PHENIX Collaboration: “High p_T Direct Photon and π^0 Triggered Azimuthal Jet Correlations in $\sqrt{s} = 200$ GeV p+p Collisions”, Phys. Rev. D 82, 072001 (2010)
38. A. Adare et al., for the PHENIX Collaboration: “Azimuthal anisotropy of neutral pion production in Au+Au collisions at $\sqrt{s_{NN}} = 200$ GeV: Path-length dependence of jet quenching and the role of initial geometry”, Phys. Rev. Lett. 105, 142301 (2010)
39. A. Adare et al., for the PHENIX Collaboration: “Elliptic and hexadecapole flow of charged hadrons in Au+Au collisions at $\sqrt{s_{NN}} = 200$ GeV”, Phys. Rev. Lett. 105, 062301 (2010)
40. A. Adare et al., for the PHENIX Collaboration: “Transverse momentum dependence of eta meson suppression in Au+Au collisions at $\sqrt{s_{NN}} = 200$ GeV”, Phys. Rev. C 82, 011902 (2010)
41. A. Adare et al., for the PHENIX Collaboration: “Transverse momentum dependence of J/ψ polarization at mid-rapidity in p+p collisions at $\sqrt{s} = 200$ GeV”, Phys. Rev. D 82, 012001 (2010)
42. A. Adare et al., for the PHENIX Collaboration: “Transition in yield and azimuthal shape modification in dihadron correlations in relativistic heavy ion collisions”, Phys. Rev. C 82, 011902 (2010)
43. T. Otsuka, T. Suzuki, J. D. Holt, A. Schwenk, Y. Akaishi, “Three-Body Forces and the Limit of Oxygen Isotopes”, Physical Review Letters **105** (2010), 032501.
44. T. Suzuki, M. Honma, T. Yoshida, H. Nao, T. Kajino, T. Otsuka, “Spin-dependent nuclear weak processes and nucleosynthesis in stars”, Prog. Part. Nucl. Phys. **66** (2011) 385-389.
45. T. Yoshida, N. Itagaki and K. Katō: “Symplectic structure and monopole strength in ^{12}C ”, Phys. Rev. C **83** (2011) 024301.

B. Proceedings

1. T. Uesaka, S. Michimasa, S. Ota, A. Saito, K. Nakanishi, Y. Sasamoto, H. Miya, H. Tokieda, S. Kawase, Y. Shimizu, S. Shimoura, K. Miki, S. Noji, H. Sakai, K. Yako, S. Itoh, T. Kawabata, Y. Yanagisawa, T. Ohnishi, H. Takeda, D. Kameda, T. Kubo, M. Sasano, H. Baba, K. Itahashi, T. Ichihara, G.P.A. Berg, P. Roussel-Chomaz, D. Bazin, Y. Shimbara and M. Nagashima, “SHARAQ Spectromete- Current status and future experimental plans-”, AIP Conference Proceedings **1224** (2010) 573.
2. T. Uesaka, S. Michimasa, S. Ota, A. Saito, K. Nakanishi, Y. Sasamoto, H. Miya, H. Tokieda, S. Kawase, Y. Shimizu, S. Shimoura, K. Miki, S. Noji, H. Sakai, K. Yako, S. Itoh, T. Kawabata, Y. Yanagisawa, T. Ohnishi, H. Takeda, D. Kameda, T. Kubo, M. Sasano, H. Baba, K. Itahashi, T. Ichihara, G.P.A. Berg, P. Roussel-Chomaz, D. Bazin, Y. Shimbara and M. Nagashima, “Current status and future experimental program of the SHARAQ spectrometer”, AIP Conference Proceedings **1235** (2010) 308.
3. P. Zhou, DQ. Fang, YG. Ma, XZ. Cai, JG. Chen, W. Guo, XY. Sun, WD. Tian, HW. Wang, GQ. Zhang, XG. Cao, Y. Fu, ZG. Hu, JS. Wang, M. Wang, Y. Togano, N. Aoi, H. Baba, T. Honda, K. Okada, Y. Hara, K. Ieki, Y. Ishibashi, Y. Itou, N. Iwasa, S. Kanno, T. Kawabata, H. Kimura, Y. Kondo, K. Kurita, M. Kurokawa, T. Moriguchi, H. Murakami, H. Oishi, S. Ota, A. Ozawa, H. Sakurai, S. Shimoura, R. Shioda, E. Takeshita, S. Takeuchi, K. Yamada, Y. Yamada, Y. Yasuda, K. Yoneda, T. Motobayashi: “Measurement of two-proton correlation from the break-up of ^{23}Al ”, Proc. of International Conference on Nuclear Reactions on Nucleons and Nuclei, Oct. 5–9, 2009, Messina, Italy, International Journal of Modern Physics E Nuclear Physics **19** (2010) 957–964
4. Y. Togano, T. Motobayashi, N. Aoi, H. Baba, S. Bishop, P. Doornenbal, T. Furukawa, S. Kanno, Y. Kondo, M. Kurokawa, Y. Matsuo, H. Murakami, S. Takeuchi, K. Yamada, K. Yoneda, X. Cai, D. Fang, YG. Ma, W. Tian, H. Wang, K. Ieki, K. Kurita, M. Matsushita, K. Okada, R. Shioda, Y. Yamada, N. Iwasa, N. Kume, T. Kawabata, S. Ota, S. Shimoura, N. Kobayashi, T. Nakamura, Y. Satou, K. Tanaka, T. Kuboki, J. Wang: “Experimental investigation of the stellar reaction $^{30}\text{S}(p, \gamma)^{31}\text{Cl}$ via coulomb dissociation”, Proc. of International Symposium on Frontiers of Researches in Exotic Nuclear Structures, Mar. 1–4, 2010, Tokamachi, JAPAN, Mod. Phys. Lett. A **25** (2010) 1763–1766
5. T. Morikawa, E. Ideguchi, S. Ota, M. Oshima, M. Koizumi, Y. Toh, A. Kimura, H. Harada, K. Furutaka, S. Nakamura, F. Kitatani, Y. Hatsukawa, T. Shizuma, M. Sugawara, H. Miyatake, Y.X. Watanabe, Y. Hirayama, M. Oi: “Superdeformed band in asymmetric $N > Z$ nucleus ^{40}Ar ”, Proc. of International Symposium on Frontiers of Researches in Exotic Nuclear Structures, Mar. 1–4, 2010, Tokamachi, JAPAN, Mod. Phys. Lett. A **25** (2010) 1792–1795
6. XY. Sun, JG. Chen, DQ. Fang, YG. Ma, XZ. Cai, W. Guo, WD. Tian, HW. Wang, P. Zhou, GQ. Zhang, XG. Cao, Y. Fu, ZG. Hu, JS. Wang, M. Wang, Y. Togano, N. Aoi, H. Baba, T. Honda, K. Okada, Y. Hara, K. Ieki, Y. Ishibashi, Y. Itou, N. Iwasa, S. Kanno, T. Kawabata, H. Kimura, Y. Kondo, K. Kurita, M. Kurokawa, T. Moriguchi, H. Murakami, H. Oishi, S. Ota, A. Ozawa, H. Sakurai, S. Shimoura, R. Shioda, E. Takeshita, S. Takeuchi, K. Yamada, Y. Yamada, Y. Yasuda, K. Yoneda, T. Motobayashi: “Measurement of the proton-proton correlation function from the break-up of ^{22}Mg and ^{20}Ne , Proc. of International Workshop on Nuclear Dynamics in Heavy-Ion Reactions and the Symmetry Energy (IWND2009), Aug. 23–25, 2009, Shnghai, Peoples R CHINA, International Journal of Modern Physics E Nuclear Physics **19** (2010) 1823–1828
7. Y. Satou, T. Nakamura, N. Fukuda, T. Sugimoto, Y. Kondo, N. Matsui, Y. Hashimoto, T. Nakabayashi, Y. Okumura, M. Shinohara, T. Motobayashi, Y. Yanagisawa, N. Aoi, S. Takeuchi, T. Gomi, Y. Togano, S. Kawai, H. Sakurai, H.J. Ong, T.K. Onishi, S. Shimoura, M. Tamaki, T. Kobayashi, H. Otsu, N. Endo, M. Kitayama, M. Ishihara: “Invariant mass spectroscopy of $^{19,17}\text{C}$ and ^{14}B using proton inelastic and charge-exchange reactions”, Proceedings of the 10th International Conference on Nucleus-Nucleus Collisions (NN2009), Aug. 17–21, 2009, Beijing, China, Nucl. Phys. **A834**, 404c–407c (2010).
8. P. Zhou, D.Q. Fang, Y.G. Ma, X.Z. Cai, J.G. Chen, W. Guo, X.Y. Sun, W.D. Tian, H.W. Wang, G.Q. Zhang, X.G. Cao, Y. Fu, Z.G. Hu, J.S. Wang, M. Wang, Y. Togano, N. Aoi, H. Baba, T. Honda, K. Okada, Y. Hara, K. Ieki, Y. Ishibashi, Y. Itou, N. Iwasa, S. Kanno, T. Kawabata, H. Kimura, Y. Kondo, K. Kurita, M. Kurokawa, T. Moriguchi, H. Murakami, H. Oishi, S. Ota, A. Ozawa, H. Sakurai, S. Shimoura, R. Shioda, E. Takeshita, S. Takeuchi, K. Yamada, Y. Yamada, Y. Yasuda, K. Yoneda, T. Motobayashi: “Measurement of two-proton correlation from the break-up of ^{23}Al ”, Proceedings of International Workshop on Nuclear Dynamics in Heavy-ion Reactions and the Symmetry Energy, Aug. 23–25, 2009, Shanghai, China, Int. J. Mod. Phys. **E19**, 957–964 (2010).

9. X.Y. Sun, J.G. Chen, D.Q. Fang, Y.G. Ma, X.Z. Cai, W. Guo, W.D. Tian, H.W. Wang, P. Zhou, G.Q. Zhang, X.G. Cao, Y. Fu, Z.G. Hu, J.S. Wang, M. Wang, Y. Togano, N. Aoi, H. Baba, T. Honda, K. Okada, Y. Hara, K. Ieki, Y. Ishibashi, Y. Itou, N. Iwasa, S. Kanno, T. Kawabata, H. Kimura, Y. Kondo, K. Kurita, M. Kurokawa, T. Moriguchi, H. Murakami, H. Oishi, S. Ota, A. Ozawa, H. Sakurai, S. Shimoura, R. Shioda, E. Takeshita, S. Takeuchi, K. Yamada, Y. Yamada, Y. Yasuda, K. Yoneda, T. Motobayashi: "MEASUREMENT OF THE PROTON-PROTON CORRELATION FUNCTION FROM THE BREAK-UP OF ^{22}Mg AND ^{20}Ne ", Proceedings of International Workshop on Nuclear Dynamics in Heavy-ion Reactions and the Symmetry Energy, Aug. 23–25, 2009, Shanghai, China, *Int. J. Mod. Phys. E* **19**, 1823–1828 (2010).
10. Y. Togano, T. Motobayashi, N. Aoi, H. Baba, S. Bishop, P. Doornenbal, T. Furukawa, S. Kanno, Y. Kondo, M. Kurokawa, Y. Matsuo, H. Murakami, S. Takeuchi, K. Yamada, K. Yoneda, X. Cai, D. Fang, Y.G. Ma, W. Tian, H. Wang, K. Ieki, K. Kurita, M. Matsushita, K. Okada, R. Shioda, Y. Yamada, N. Iwasa, N. Kume, T. Kawabata, S. Ota, S. Shimoura, N. Kobayashi, T. Nakamura, Y. Satou, K. Tanaka, T. Kuboki, J. Wang: "EXPERIMENTAL INVESTIGATION OF THE STELLAR REACTION $^{30}\text{S}(p,\gamma)^{31}\text{Cl}$ VIA COULOMB DISSOCIATION", Proceedings of International Symposium on Frontiers of Researches in Exotic Nuclear Structures (Niigata 2010), Mar. 1–4, 2010, Niigata, Japan, *Mod. Phys. Lett. A* **25**, 1763–1766 (2010).
11. A. Saito, S. Shimoura, T. Minemura, Y.U. Matsuyama, H. Baba, N. Aoi, T. Gomi, Y. Higurashi, K. Ieki, N. Imai, N. Iwasa, H. Iwasaki, S. Kanno, S. Kubono, M. Kunibu, S. Michimasa, T. Motobayashi, T. Nakamura, H. Ryuto, H. Sakurai, M. Serata, E. Takeshita, S. Takeuchi, T. Teranishi, K. Ue, K. Yamada, Y. Yanagisawa: "THE $^6\text{He}+^6\text{He}$ AND $\alpha+^8\text{He}$ CLUSTER STATES IN ^{12}Be VIA α -INELASTIC SCATTERING", Proceedings of International Symposium on Frontiers of Researches in Exotic Nuclear Structures (Niigata 2010), Mar. 1–4, 2010, Niigata, Japan, *Mod. Phys. Lett. A* **25**, 1858–1861 (2010).
12. T. Morikawa, E. Ideguchi, S. Ota, M. Oshima, M. Koizumi, Y. Toh, A. Kimura, H. Harada, K. Furutaka, S. Nakamura, F. Kitatani, Y. Hatsukawa, T. Shizuma, M. Sugawara, H. Miyatake, Y.X. Watanabe, Y. Hirayama, M. Oi: "SUPERDEFORMED BAND IN ASYMMETRIC N ; Z NUCLEUS ^{40}Ar " Proceedings of International Symposium on Frontiers of Researches in Exotic Nuclear Structures (Niigata 2010), Mar. 1–4, 2010, Niigata, Japan, *Mod. Phys. Lett. A* **25**, 1792–1795 (2010).
13. A. Odahara, A. Takahima, M. Suga, K. Tajiri, K. Kurata, J. Takatsu, Y. Ito, Y. Kenmoku, K. Yamaguchi, M. Kazato, K. Kura, T. Shimoda, T. Suzuki, H. Watanabe, S. Nishimura, Y. Gono, E. Ideguchi, S. Go, Y. Wakabayashi, T. Morikawa, C. Petrache, D. Beaumel: "ISOMER SPECTROSCOPY AT RI BEAM LINE IN RCNP", Proceedings of International Symposium on Frontiers of Researches in Exotic Nuclear Structures (Niigata 2010), Mar. 1–4, 2010, Niigata, Japan, *Mod. Phys. Lett. A* **25**, 1951–1954 (2010).
14. T. Uesaka, S. Michimasa, S. Ota, A. Saito, K. Nakanishi, Y. Sasamoto, H. Miya, H. Tokieda, S. Kawase, Y. Shimizu, S. Shimoura, K. Miki, S. Noji, H. Sakai, K. Yako, S. Itoh, T. Kawabata, Y. Yanagisawa, T. Ohnishi, H. Takeda, D. Kameda, T. Kubo, M. Sasano, H. Baba, K. Itahashi, T. Ichihara, G.P.A. Berg, P. Roussel-Chomaz, D. Bazin, Y. Shimbara, M. Nagashima: "SHARAQ Spectrometer-Current Status and Future Experimental Plans", Proc. Intern. Symposium Exotic Nuclei, Sochi, (Russia), 28 Sept.–2 Oct. 2009, Yu.E. Penionzhkevich, S.M. Lukyanov, Eds., pp.573–581 (2010); *AIP Conf. Proc.* 1224 (2010).
15. H. Yamaguchi, T. Hashimoto, S. Hayakawa, D. N. Binh, D. Kahl, and S. Kubono: "Nuclear Astrophysics and Structure Studies Using Low-energy RI Beams at CRIB", 7th Japan-China Joint Nuclear Physics Symposium, Nov. 9–13, 2009, Tsukuba University, Tsukuba, Japan. *AIP conference proceeding* **1235** (2010) 247–252 .
16. H. Yamaguchi, T. Hashimoto, S. Hayakawa, D. N. Binh, D. Kahl, and S. Kubono: "Studies of alpha-induced astrophysical reactions at CRIB", The 10th International Symposium on Origin of Matter and Evolution of Galaxies: OMEG–2010, March 8–10, 2010, RCNP, Osaka University, Osaka, Japan *AIP conference proceeding* **1269** (2010) 262–267 .
17. H. Yamaguchi, T. Hashimoto, S. Hayakawa, D.N. Binh, D. Kahl, S. Kubono: "Alpha-induced astrophysical reactions studied at CRIB", Proceedings of the International Symposium on Nuclear Astrophysics "Nuclei in the Cosmos - XI", Jul. 19–23, 2010, Heidelberg, Germany, *Proceedings of Science, PoS(NIC-XI)214* (2011).
18. S. Hayakawa, S. Kubono, T. Hashimoto, H. Yamaguchi, D. N. Binh, D. Kahl, Y. Wakabayashi, N. Iwasa, N. Kume, I. Miura, T. Teranishi, J. J. He, Y. K. Kwon, T. Komatsubara, S. Kato, and S. Wanajo, "Direct measurement of the $^{11}\text{C}(\alpha, p)^{14}\text{N}$ stellar reaction at CRIB", *AIP Conference Proceedings Volume 1269* (2010) pp104–109, The 10th International Symposium on Origin of Matter and Evolution of Galaxies (OMEG2010).

19. Yoki Aramaki, for the PHENIX Collaboration: “Neutral pion production with respect to reaction plane in Au+Au collisions at RHIC-PHENIX”, Proc. of the 20th International Conference in Ultra-Relativistic Nucleus-Nucleus Collisions (QM2008), Indian Journal of Physics 84, pp1669-1673, 2010
20. T. Gunji, “Heavy quark and quarkonium productions in high energy nucleus-nucleus collisions at RHIC and LHC”, Proc. of the YIPQS International Workshop on High Energy Strong Interactions 2010, Prog.Theor.Phys.Suppl.187:78-86,2011
21. H. Hamagaki, “First results from the ALICE experiment at LHC”, Proc. of the YIPQS International Workshop on High Energy Strong Interactions 2010, Prog.Theor.Phys.Suppl.187:237-249,2011
22. Y. Hori, H. Hamagaki, T. Gunji, “Simulation study for forward calorimeter in LHC-ALICE experiment”, Proc. of 14th International Conference On Calorimetry In High Energy Physics (CALOR 2010), J.Phys.Conf.Ser.293:012029,2011
23. K. Aoki, H. Hamagaki, T. Gunji, T. Tsuji *et al.*, “A development of HBD for the J-PARC E16 experiment”, Proc. of 12th Vienna Conference on Instrumentation, Vienna, Austria, 15-20 Feb 2010, Nucl.Instrum.Meth.A628:300-303,2011
24. R. Akimoto *et al.*, “Development of a Time Projection Chamber (TPC) Using Gas Electron Multiplier (GEM) for Use as an Active Target”, Proc. of 2010 IEEE Nuclear Science Symposium Conference Record, Oct. 30 - Nov. 6, 2010

C. Theses

1. Dam Ngyen Binh: ”Study of the $^{21}\text{Na}(\alpha,p)^{24}\text{Mg}$ Stellar Reaction by α -scattering and (α,p) Measurements in Inverse Kinematics”, Doctor thesis, University of Tokyo, October, 2011
2. Y. Aramaki: “Measurement of Neutral Pion with Respect to the Azimuthal Angle in Au+Au Collisions at $\sqrt{s_{NN}} = 200$ GeV”, Doctor Thesis, University of Tokyo, March (2011).
3. Y. Yamaguchi: “Direct photon measurement with virtual photon method in d+Au collisions at $\sqrt{s_{NN}} = 200$ GeV” Doctor Thesis, University of Tokyo, March (2011).
4. T. Tsuji: “Simulation Study of the Forward Calorimeter for LHC-ALICE” Master Thesis, University of Tokyo, March (2011).
5. S. Kawase: “200 MeV での $(\bar{p}, 2p)$ 反応による ^{18}O の陽子スピン軌道分離”, Master Thesis, University of Tokyo, March (2011).
6. S. Go: “Development of 3-D position sensitive Ge detectors for highly-sensitive in-beam gamma-ray spectroscopy”, Master Thesis, the University of Tokyo, March 2011.

D. Other Publications

1. T. Otsuka, T. Suzuki, ”Shell Evolutions of Atomic Nuclei due to the Tensor Force”, BUTSURI, **66** (2011) 195-200.

Talks and Presentations

A. Conferences

1. T. Uesaka, “Polarization Study of Unstable Nuclei”, ECT* Workshop “Reactions and Nucleon Properties in Rare Isotope”, 6-10 April 2010, Trento, Italy
2. T. Uesaka, “High-resolution SHARAQ Spectrometer at RI Beam Factory”, International Nuclear Physics Conference 2010, 4-9 July 2010, Vancouver, Canada
3. T. Uesaka, “Heavy-ion charge exchange reactions with transitions within supermultiplet members”, RCNP workshop on Nuclear Reaction, 2-4 August 2010, Osaka, Japan
4. T. Uesaka, “Spin-isospin studies with the SHARAQ Spectromete” University of Aizu-JUSTIPEN-EFES Symposium on “Cutting-Edge Physics of Unstable Nuclei”, 10-13 November 2010, Aizu, Japan
5. T. Uesaka, “Tensor force effects in few-body reactions with large momentum transfer”, RCNP 研究会 核構造の真の理解に向けて - テンソル力と高運動量成分 - 戦略会議 25-26 November 2010, Osaka, Japan
6. T. Uesaka, “SHARAQ Spectromete” 4th International Expert Meeting on In-flight Separators and Related Issues, 15-17 December 2010, Darmstadt, Germany
7. T. Uesaka, “High-resolution Ion-optical analysis of RI-beams with the SHARAQ Spectrometer”, French-Japanese Symposium on Nuclear Structure Problems, 5-8 January 2011, Saitama, Japan
8. T. Uesaka, “Spin observable in proton elastic scattering of $6,8\text{He}$ and its relevance to cluster structure”, International EFES-IN2P3 Conference “Many body correlations from dilute to dense nuclear systems”, 15-18 February 2011
9. T. Uesaka, “Spin-isospin studies with RI-beam induced charge exchange reactions”, The 5th LACM-EFES-JUSTIPEN Workshop, 15-17 March 2011, Oak Ridge, USA.
10. S. Ota (Oral): “CNS Active Target Project”, Workshop on advanced detector technology for nuclear physics, 11-12, January, 2011, RIKEN, Japan
11. S. Ota (Oral): “($d,^2\text{He}$) reaction with Active Target”, Symposium on Physics Perspective at RIBF Initiated by Prof. Hiroyuki Okamura, 22, January, 2011, RIKEN, Japan
12. H. Matsubara, M. Takaki, and T. Uesaka for E358 collaboration (Poster): “Spectroscopy of ^9He via the ($^{18}\text{O},^{18}\text{Ne}$) reaction by high resolution spectrograph Grand Raiden at RCNP”, HALO2010, Dec. 7–9, 2010, Shonan international village, Kanagawa, Japan.
13. Y. Sasamoto, T. Uesaka, S. Shimoura, S. Michimasa, S. Ota, H. Tokieda, H. Miya, S. Kawase, Y. Kikuchi, K. Kisamori, M. Takaki, M. Dozono, H. Mathubara, S. Noji, K. Miki, K. Yako, H. Sakai, T. Kubo, Y. Yanagisawa, K. Yoshida, T. Ohnishi, N. Fukuda, H. Takeda, D. Kameda, N. Inabe, N. Aoi, S. Takeuchi, T. Ichihara, H. Baba, S. Sakaguchi, P. Doornembal, W. He, C. Ruijiu, Y. Shimizu, T. Kawahara, T. Kawabata, N. Yokota, Y. Maeda, H. Miyasako, G. P. A. Berg (Oral): “Study of Studies of isovector non-spin-flip monopole transition via the super-allowed Fermi type charge exchange reaction”, French-Japanese Symposium on Nuclear Structure Problems Organized in the framework of FJNSP LIA and EFES -, Jan. 5–8, 2011, RIKEN, Wako, Japan.
14. S. Shimoura (invited): “Direct reactions populating continuum states of exotic nuclei”, Japan-Italy EFES Workshop, Sept. 6–8, 2010, Istituti di Fisica, Torino, Italy.
15. S. Shimoura (invited): “Single-particle wave functions near the threshold — coupled-channel effects on spectroscopic factors —”, ECT* Workshop on Reactions and Nucleon Properties in Rare isotopes, April 6–10, 2010, Trento, Italy.
16. T. Uesaka (invited): “Polarization study of unstable nuclei”, ECT* Workshop on Reactions and Nucleon Properties in Rare isotopes, April 6–10, 2010, Trento, Italy.

17. S. Shimoura (invited): “Cluster Structures in Neutron-Rich Nuclei Via Alpha-Inelastic Scattering in Inverse Kinematics”, The 5th LACM-EFES-JUSTIPEN Workshop, March 15–17, 2011, Oak Ridge National Laboratory, Oak Ridge, Tennessee, USA.
18. T. Uesaka (invited): “Spin-Isospin Studies With Ri-Beam Induced Charge Exchange Reactions” The 5th LACM-EFES-JUSTIPEN Workshop, March 15–17, 2011, Oak Ridge National Laboratory, Oak Ridge, Tennessee, USA.
19. S. Shimoura (invited): “CNS GRAPE for high-resolution spectroscopy of in-flight gamma decay”, French-Japanese Symposium on Nuclear Structure Problems, Jan. 5–8, 2011, RIKEN, Wako, Japan.
20. T. Uesaka (invited): “High-resolution ion-optical analysis of RI beams with the SHARAQ spectrometer”, French-Japanese Symposium on Nuclear Structure Problems, Jan. 5–8, 2011, RIKEN, Wako, Japan.
21. Y. Sasamoto, T. Uesaka, S. Shimoura, S. Michimasa, S. Ota, H. Tokieda, H. Miya, S. Kawase, Y. Kikuchi, K. Kisamori, M. Takaki, M. Dozono, H. Mathubara, S. Noji, K. Miki, K. Yako, H. Sakai, T. Kubo, Y. Yanagisawa, K. Yoshida, T. Ohnishi, N. Fukuda, H. Takeda, D. Kameda, N. Inabe, N. Aoi, S. Takeuchi, T. Ichihara, H. Baba, S. Sakaguchi, P. Doornembal, W. He, C. Ruijiu, Y. Shimizu, T. Kawahara, T. Kawabata, N. Yokota, Y. Maeda, H. Miyasako, G. P. A. Berg (Oral): “Study of Studies of isovector non-spin-flip monopole transition via the super-allowed Fermi type charge exchange reaction”, French-Japanese Symposium on Nuclear Structure Problems, Jan. 5–8, 2011, RIKEN, Wako, Japan.
22. S. Shimoura (invited): “Nuclear Physics Research at CNS”, The International Symposium on Nuclear Physics in Asia, Oct. 13–15, 2010, Beihang University, Beijing, China.
S. Kubono (invited): “Experimental Approach to Explosive Nucleosynthesis with Low-Energy RI beams”, The International Symposium on Nuclear Physics in Asia, Oct. 13–15, 2010, Beihang University, Beijing, China.
23. S. Michimasa (Oral): “Development of Diamond Detector at CNS”, Workshop on advanced detector technology for nuclear physics, Jan. 12, 2011, RIKEN, Wako, Japan.
24. E. Ideguchi (Oral): “Superdeformed band in asymmetric $N_{\zeta}Z$ nucleus, ^{40}Ar ”, Nuclear Structure 2010 conference, August 8–13, 2010, Clark-Kerr Campus, U.C. Berkeley, CA, USA.
25. E. Ideguchi (Oral): “Superdeformed Band in Asymmetric $N_{\zeta}Z$ Nucleus, ^{40}Ar , and High-Spin Studies in $A=30\sim 40$ Nuclei”, University of Aizu-JUSTIPEN-EFES symposium “Cutting Edge Physics of Unstable Nuclei”, November 10–13, 2010, University of Aizu, Fukushima, Japan.
26. E. Ideguchi (Oral): “Gamma-ray spectroscopy at storage ring”, RCNP Workshop on “Physics of heavy-ion strange ring”, September 24–25, RCNP, Osaka university, Japan.
27. E. Ideguchi (Oral): “Possible use of SHOGUN spectrometer for the studies of hyperdeformed nuclei”, Workshop on the SHOGUN gamma-ray spectrometer, February 4–5, 2011, RIKEN, Wako, Saitama, Japan.
28. H. Yamaguchi, T. Hashimoto, S. Hayakawa, D.N. Binh, D. Kahl, and S. Kubono: “Alpha-resonance-scattering measurements at CRIB”, Second EMMI-EFES workshop on neutron-rich nuclei (EENEN10), June 16–18, 2010, RIKEN, Wako, Japan.
29. H. Yamaguchi, T. Hashimoto, S. Hayakawa, D.N. Binh, D. Kahl, S. Kubono (Poster): “Alpha-induced astrophysical reactions studied at CRIB”, 11th Symposium on Nuclei in the Cosmos (NIC XI), Jul. 19–23, 2010, Heidelberg, Germany.
30. H. Yamaguchi: “Experimental techniques with RIB –Introduction of CRIB facility–”, Korea-Japan joint workshop for the nuclear physics and the nuclear astrophysics, Oct. 26, 2010, Seoul National University, Seoul, Korea.
31. H. Yamaguchi, T. Hashimoto, S. Hayakawa, D.N. Binh, D. Kahl, and S. Kubono: “Studies for alpha-induced astrophysical reactions at CRIB”, University of Aizu-JUSTIPEN-EFES Symposium on “Cutting-Edge Physics of Unstable Nuclei”, Nov. 10–13, 2010, University of Aizu, Fukushima, Japan.
32. H. Yamaguchi, T. Hashimoto, S. Hayakawa, D.N. Binh, D. Kahl, and S. Kubono: “Studies on $^7\text{Li}/^7\text{Be}$ +alpha resonant scatterings”, RIBF-ULIC Symposium “Impact of the new α reaction rate on stellar evolution and nucleosynthesis”, Dec. 17–18, 2010, RIKEN Nishina Center, Wako, Japan.
33. H. Yamaguchi: “Experiments on alpha resonance state”, Mini-workshop for resonance elastic scattering in inverse kinematics, Dec. 17, 2010, RIKEN Nishina Center, Wako, Japan.

34. S. Hayakawa, S. Kubono, T. Hashimoto, H. Yamaguchi, D.N. Binh, D. Kahl, Y. Wakabayashi, N. Iwasa, N. Kume, Y. Miura, T. Teranishi, J.J. He, Y.K. Kwon, T. Komatsubara, S. Kato and S. Wanajo (Oral): “Direct determination of the $^{11}\text{C}(\alpha, p)^{14}\text{N}$ reaction rate with CRIB: an alternative synthesis path to the CNO elements”, at 11th Symposium on Nuclei in the Cosmos, Jul. 19–23, 2010, Heidelberg, Germany.
35. S. Hayakawa, S. Kubono, T. Hashimoto, H. Yamaguchi, D.N. Binh, D. Kahl, Y. Wakabayashi, N. Iwasa, N. Kume, Y. Miura, T. Teranishi, J.J. He, Y.K. Kwon, T. Komatsubara, S. Kato and S. Wanajo (Oral): “Direct measurement of the $^{11}\text{C}(\alpha, p)^{14}\text{N}$ reaction \sim pp to CNO \sim ”, at Impact of New Triple Alpha Reaction Rate on Stellar Evolution and Nucleosynthesis, Dec. 19–23, 2010, RIKEN, Wako, Japan.
36. T. Gunji for the ALICE-FOCAL team, “Current status and plan of ALICE FOCAL project”, The workshop for ALICE upgrade by Asian countries, March 7-8, 2011, Yonsei, Korea
37. H. Hamagaki: “Status of ALICE FOCAL project”, The workshop for ALICE upgrade by Asian countries, March 7-8, 2011, Yonsei, Korea
38. S. Sano: “Strangeness production in p+p collisions at LHC”, The workshop for ALICE upgrade by Asian countries, March 7-8, 2011, Yonsei, Korea
39. T. Tsuji, H. Hamgaki, T. Gunji *et al.*, “Simulation study of ALICE FOCAL”, The workshop for ALICE upgrade by Asian countries, March 7-8, 2011, Yonsei, Korea
40. S. Hayashi H. Hamgaki, T. Gunji *et al.*, “ASIC development for ALICE FOCAL readout”, The workshop for ALICE upgrade by Asian countries, March 7-8, 2011, Yonsei, Korea
41. S. Hayashi, H. Hamgaki, T. Gunji *et al.*, “ALICE 実験における W+Si カロリメータ用読み出し ASIC の開発”, OpenIt ASIC ワークショップ 2010, Feb. 1st, 2011, 長崎総合科学大学
42. T. Gunji: “W+Si Forward tracking calorimeter for the ALICE upgrade”, Workshop on the PHENIX decadal plan, Dec. 12-14, 2010, BNL, USA
43. R. Akimoto: “Development of a Time Projection Chamber (TPC) Using Gas Electron Multiplier (GEM) for Use as an Active Target”, 2010 Nuclear Science Symposium and Medical Imaging Conference (IEEE), 10/30- 11/6, 2010, Knoxville, USA
44. A. Takahara for the PHENIX Collaboration: “Measurement of the Ultra-peripheral J/ψ Cross Section in Au+Au Collisions with the PHENIX Detector”, The Third Asian Triangle Heavy-Ion Conference (ATHIC 2010), 10/18-20, 2010, Wuhan, China
45. H. Hamagaki for the ALICE Collaboration: “The first results from ALICE”, Workshop on High Energy Strong Interactions 2010, 8/10-8/13, 2010, Yukawa Institute for Theoretical Physics, in Kyoto, Japan,
46. T. Gunji: “Heavy quark and quarkonia production in high energy nucleus-nucleus collisions at RHIC and LHC”, Workshop on High Energy Strong Interactions 2010, 8/10-8/13, 2010, Yukawa Institute for Theoretical Physics, in Kyoto, Japan,
47. Y. Hori: “Simulation study of Forward Calorimeter in LHC-ALICE experiment”, 14th International Conference on Calorimetry in High Energy Physics, 5/10-5/14, 2010, Peking, China
48. T. Suzuki: “Electron capture reactions in fp-shell nuclei and beta decays in rare isotopes”, ECT* Workshop on “Reactions and Nucleon Properties in Rare Isotopes”, April 2010, Toronto, Italy.
49. T. Suzuki, M. Honma, T. Yoshida, H. Mao, T. Kajino, T. Otsuka: “Gamow-Teller and First-forbidden Transition Strengths in Astrophysical Processes”, International Nuclear Physics Conference 2010 (INPC2010), July 9, 2010, Vancouver, Canada.
50. T. Suzuki, M. Honma, H. Mao, T. Yoshida, T. Kajino, T. Otsuka: “Electron capture reactions and beta decays in astrophysical environments”, The 3rd International Conference on Frontiers in Nuclear Structure, Astrophysics and Reactions (FINUSTAR3), August 23, 2010, Rhodos, Greece.
51. T. Suzuki: “Nuclear weak processes in stars”, Japn-Italy EFES Workshop on Correlations in REactions and Continuum, Sept. 8, 2010, Torino, Italy.

52. T. Suzuki, M. Honma, T. Yoshida, H. Mao, T. Kajino, T. Otsuka: "Spin dependent nuclear weak processes and nucleosynthesis in stars", International School of Physics, 32nd Course, Particle and Nuclear Astrophysics, Sept. 22, 2010, Erice, Italy.
53. T. Suzuki, T. Otsuka: "Spin modes in nuclei and nuclear forces", International Symposium on New Faces of Atomic Nuclei, Nov. 15, 2010, Okinawa, Japan.
54. T. Suzuki (invited): "Beta decays and isobaric analog states of exotic light nuclei", International Symposium on HALO 2010, Dec. 8, 2010, Zushi, Japan.
55. T. Suzuki: "Spin modes in nuclei and astrophysical processes based on new Hamiltonians", International EFES-IN2P3 Conference on "Many Body Correlations from Dilute to Dense Nuclear Systems", Feb. 18, 2011, IHP, Paris, France.
56. T. Suzuki (invited): "Neutrino-nucleus reactions at MeV region based on new shell-model Hamiltonians", 7th International Workshop on Neutrino-Nucleus Interactions in the Few-GeV Region, March 9, 2011, Dehradun, India.

B. JPS Meetings

1. H. Matsubara, A. Tamii, T. Adachi, D. Ishikawa, M. Itoh, J. Carter, H. Okamura, B. Ozel, M. Kato, T. Kawabata, S. Kuroita, H. Sakaguchi, S. Sakaguchi, Y. Sakemi, Y. Sasamoto, Y. Shimizu, F.D. Smit, Y. Shimbara, K. Suda, J. Zenihiro, Y. Tameshige, M. Dozono, H. Tokieda, H. Nakada, K. Nakanishi, P.von Neumann-Cosel, A. Nonaka, R. Neveling, K. Hatanaka, K. Fujita, N. Fujita, H. Fujita, Y. Fujita, A. Perez, L.A. Popescu, I. Poltoratska, Y. Maeda, R. Yamada, Y. Yamada, M. Yosoi, A. Richter, B. Rubio (Oral): " $M1$ strength distributions and quenching problem for the $N = Z$ nuclei in the sd -shell region.", at the JPS Spring meeting, Mar. 26–29, 2011, Niigata University, Niigata, Japan.
2. M. Dozono, T. Wakasa, T. Noro, K. Sagara, Y. Yamada, S. Kuroita, T. Imamura, H. Shimoda, T. Sueta, K. Hatanaka, H. Okamura, A. Tamii, H. Matsubara and Y. Sakemi: "Study of spin-dipole strengths in ^{12}N via $^{12}\text{C}(\bar{p}, \bar{n})$ reaction", at the JPS Spring meeting, Mar. 26–29, 2011, Niigata University, Niigata, Japan.
3. T. Kawahara, T. Uesaka, Y. Shimizu, S. Sakaguchi, A. Shibusawa, T. Wakui: "Pulse structure dependence of the proton polarization rate", at the JPS Fall meeting, Sep. 11–14, 2010, Kyushu Institute of Technology University, Kyushu, Japan.
4. Y. Sasamoto, T. Uesaka, S. Shimoura, S. Michimasa, S. Ota, H. Tokieda, H. Miya, S. Kawase, Y. Kikuchi, K. Kisamori, M. Takaki, M. Dozono, H. Mathubara, S. Noji, K. Miki, K. Yako, H. Sakai, T. Kubo, Y. Yanagisawa, K. Yoshida, T. Ohnishi, N. Fukuda, H. Takeda, D. Kameda, N. Inabe, N. Aoi, S. Takeuchi, T. Ichihara, H. Baba, S. Sakaguchi, P. Doornembal, W. He, C. Ruijiu, Y. Shimizu, T. Kawahara, T. Kawabata, N. Yokota, Y. Maeda, H. Miyasako, G. P. A. Berg (Oral): "Studies for isovector non-spin-flip monopole resonances via the super allowed Fermi type charge exchange reaction" at the JPS Spring meeting, Mar. 25–28, Niigata University, Niigata, Japan.
5. Y. Kikuchi, S. Ota, N. Matsubara, H. Miya, S. Kawase, K. Kisamori, M. Takaki, K. Miki, T. Uesaka: "Development of the new detector consisted of 30 thin plastic scintillators for the high rate RI beam", at the JPS Spring meeting, Mar. 26–29, 2011, Niigata University, Niigata, Japan.
6. S. Go, S. Shimoura, E. Ideguchi, S. Ota, H. Miya, H. Baba (Oral): "Development of 3-D position extraction for segmented Ge detectors by using pulse shape analysis" JPS Autumn Meeting, September 11–14, 2011, Kyushu Institute of Technology, Tohata, Japan
7. H. Miya, S. Shimoura, A. Saito, K. Miki, M. Sasano, T. Kawabata, S. Kawase, S. Ota, T. Uesaka, H. Sakai (Oral): "Performance evaluation of Low-Pressure Multi-Wire Drift Chamber", at the JPS Autumn meeting, Sep. 11–14, 2010, Kyushu Institute of Technology University, Fukuoka, Japan.
8. S. Go, S. Shimoura, E. Ideguchi, S. Ota, H. Miya, H. Baba (Oral): "3-Dimensional position extraction for segmented Ge detector" JPS Spring Meeting, March 25–28, 2011, Niigata University, Niigata, Japan

9. E. Ideguchi, S. Go, H. Miya, K. Kisamori, M. Takaki, S. Ota, S. Michimasa, S. Shimoura, T. Koike, T. Yamamoto, K. Shirotori, Y. Ito, J. Takatsu, T. Suzuki, T. Morikawa, T. Shinozuka, Y. Seongbae, T. Shizuma, M. Oshima, M. Koizumi, Y. Toh, Y. Hatsukawa, A. Kimura, K. Furutaka, S. Nakamura, F. Kitadani, H. Harada, M. Sugawara, Y.X. Watanabe, Y. Hirayama, M. Oi (Oral): “Study of High-Spin States in $^{35}\text{S II}$ ”, at JPS Spring Meeting, Mar. 25–28, 2011, Niigata University, Niigata, Japan.
10. K. Kisamori, S. Shimoura, S. Michimasa, S. Ota, S. Noji, H. Tokieda and H. Baba (Oral): “Development of readout system at final focal plane detector in SHARAQ spectrometer for missing mass measurement of tetra-neutron system”, at the JPS Spring meeting, Mar. 25–28, 2011, Niigata University, Niigata, Japan.
11. H. Miya, S. Ota, H. Matsubara, S. Noji, S. Kawase, Y. Kikuchi, K. Kisamori, M. Takaki, S. Michimasa, K. Miki, T. Uesaka, and S. Shimoura (Oral): “Performance evaluation of Low-Pressure Muti Wire Drift Chamber with High Intensity Unstable Heavy Ion Beam”, at the JPS Spring meeting, Mar. 25–27, 2011, Niigata University, Niigata, Japan.
12. Y. Sasamoto, T. Uesaka, S. Shimoura, S. Michimasa, S. Ota, H. Tokieda, H. Miya, S. Kawase, Y. Kikuchi, K. Kisamori, M. Takaki, M. Dozono, H. Mathubara, S. Noji, K. Miki, K. Yako, H. Sakai, T. Kubo, Y. Yanagisawa, K. Yoshida, T. Ohnishi, N. Fukuda, H. Takeda, D. Kameda, N. Inabe, N. Aoi, S. Takeuchi, T. Ichihara, H. Baba, S. Sakaguchi, P. Doornembal, W. He, C. Ruijiu, Y. Shimizu, T. Kawahara, T. Kawabata, N. Yokota, Y. Maeda, H. Miyasako, G. P. A. Berg (Oral): “Studies for isovector non-spin-flip monopole resonances via the super allowed Fermi type charge exchange reaction” at the JPS Spring meeting, Mar. 25–28, Niigata university, Niigata, Japan.
13. S. Michimasa, Y. Yanagisawa, K. Inafuku, N. Aoi, Z. Elekes, Zs. Fulop, Y. Ichikawa, N. Iwasa, K. Kurita, M. Kurokawa, T. Machida, T. Motobayashi, T. Nakamura, T. Nakabayashi, M. Notani, H.J. Ong, T.K. Onishi, H. Otsu, H. Sakurai, M. Shinohara, T. Sumikama, S. Takauchi, K. Tanaka, Y. Togano, K. Yamada, M. Yamaguchi, K. Yoneda (Oral): “Gamma-ray spectroscopy of very neutron-rich magnesium isotopes by using the proton inelastic scattering” at the JPS Spring meeting, Mar. 25–28, 2011, Niigata university, Niigata, Japan.
14. M. Takaki, H. Matsubara, T. Uesaka, S. Ota, S. Kawase, T. Kawabata, Y. Kikuchi, K. Kisamori, S. Sakaguchi, Y. Sasamoto, S. Shimoura, T. Suzuki, J. Zenihiro, K. Takahisa, A. Tamii, H. Tokieda, M. Dozono, S. Noji, K. Hatanaka, Y. Maeda, S. Michimasa, H. Miya, H. Miyasako, Y. Yasuda (Oral): “Study of heavy ion double charge exchange reaction via the ($^{18}\text{O}, ^{18}\text{Ne}$) reaction between same super-multiplet states” at the JPS Spring meeting, Mar. 25–28, 2011, Niigata University, Niigata, Japan.
15. T. Gunji, for the ALICE Collaboration: “Future perspectives and plans of the ALICE experiment”, at the JPS Autumn meeting, September 11-14, 2010, Kyusyu Institute of Technology, Kitakyushu, Japan.
16. Y. Aramaki, for the PHENIX Collaboration (Oral): “Study of parton energy loss with high-pT pi0 in Au+Au collisions at PHENIX”, at the JPS Autumn meeting, September 11-14, 2010, Kyusyu Institute of Technology, Kitakyushu, Japan.
17. S. Sano, for the ALICE Collaboration: “The Status and the results in measurement of charged particles” at the JPS Autumn meeting, September 11-14, 2010, Kyusyu Institute of Technology, Kitakyushu, Japan.
18. Y. Hori, for the ALICE-TPC Collaboration: “LHC-ALICE 実験における TPC の ExB ディストーション” at the JPS Autumn meeting, September 11-14, 2010, Kyusyu Institute of Technology, Kitakyushu, Japan.
19. T. Tsuji: “LHC-ALICE 実験のアップグレードに向けた前方カロリメーターの研究” at the JPS Autumn meeting, September 11-14, 2010, Kyusyu Institute of Technology, Kitakyushu, Japan.
20. T. Gunji for the ALICE Collaborarion: “Heavy Quarkonia Production in p+p and Pb+Pb collisions at LHC-ALICE”, at the JPS Spring meeting, Mar. 25–28, 2011, Niigata University, Niigata, Japan.
21. Y. Yamaguchi for the PHENIX Collaboration: “Measurement of low pT direct photons in d+Au collisions at the PHENIX experiment”, at the JPS Spring meeting, Mar. 25–28, 2011, Niigata University, Niigata, Japan.
22. S. Sano for the ALICE Collaboration: “Multi-strangeness particle production in $\sqrt{s} = 7$ TeV p+p collisions at LHC-ALICE”, at the JPS Spring meeting, Mar. 25–28, 2011, Niigata University, Niigata, Japan.
23. A. Takahara for the PHENIX Collaboration: “Measurement of J/ψ photoproduction in ultra-peripheral Au+Au collisions at $\sqrt{s_{NN}}=200\text{GeV}$ using the PHENIX detecto”, at the JPS Spring meeting, Mar. 25–28, 2011, Niigata University, Niigata, Japan.

24. T. Tsuji, H. Hamagaki, T. Gunji, Y. Hori: “シミュレーションを用いた LHC-ALICE 実験用前方カロリメータの性能評価”, at the JPS Spring meeting, Mar. 25–28, 2011, Niigata University, Niigata, Japan.
25. S. Hayashi, H. Hamagaki, T. Gunji *et al.*, “Si+W カロリメータ用読み出し ASIC の開発”, at the JPS Spring meeting, Mar. 25–28, 2011, Niigata University, Niigata, Japan.
26. A. Nukariya, H. Hamagaki *et al.*, “GEM を用いたイメージング装置の読み出し部分の開発”, at the JPS Spring meeting, Mar. 25–28, 2011, Niigata University, Niigata, Japan.

C. Lectures

1. 下浦 享: 「エキゾチック原子核の世界 —陽子と中性子が織りなす量子系の多様性—」, June 1–2, 2010, Chiba University, Chiba, Japan.
2. T. Suzuki: ”Nuclear structure and nuclear weak and neutrino processes”, Special Lectures on Astronomy V ”Nuclear Astrophysics”, Jan. 27, 28, 2011, National Astronomical Observatory of Japan, Mitaka, Japan.
3. H. Yamaguchi: “Recent experimental studies on nuclear astrophysics at CRIB”, The 9th CNS-EFES International Summer School (CNS-EFES10), Aug. 18–24, 2010, CNS, Wako, Japan.

D. Seminars

1. T. Uesaka, “Spin-isospin studies with RI-beam induced charge exchange reactions”, seminar at Notre Dame University, 1 March 2011, South Bend, USA
2. 下浦 享: 「直接反応で探るエキゾチック核の構造」, June 2, 2010, Chiba University, Chiba, Japan.
3. T. Suzuki: ”Tensor force and shell evolutions”, Toward the real understanding of nuclear structure - tensor force and high momentum components, Nov. 26, 2010, RCNP, Osaka, Japan.
4. T. Suzuki: ”Structure of light nuclei and shell evolutions” ”Structure of Ca isotopes and roles of three-body forces”, Workshop on nuclear forces, Feb. 21, 2011, University of Oslo, Norway.

Personnel

Director

OTSUKA, Takaharu *Professor, Department of Physics,
Graduate School of Science*

Scientific Staff

1. Heavy-Ion Collisions

SHIMOURA, Susumu *Professor*
UESAKA, Tomohiro *Associate Professor*
IDEGUCHI, Eiji *Lecturer*
MICHIMASA, Shin'ichiro *Assistant Professor*
OTA, Shinsuke *Assistant Professor*

3. Nuclear Structure in Extreme States

KUBONO, Shigeru *Professor*
HAMAGAKI, Hideki *Associate Professor*
YAMAGUCHI, Hidetoshi *Assistant Professor*
GUNJI, Taku *Assistant Professor*

Guest Professors

SUZUKI, Toshio *Nihon University*
MITSUMOTO, Toshinori *Sumitomo Heavy Industries, Ltd.*

Technical Staff

OHSIRO, Yukimitsu *YAMAZAKI, Norio*

Technical Assistants

WATANABE, Shin-ichi

YAMAKA, Shoichi

NINOMIYA, Hideaki

KUREI, Hiroshi

YOSHINO, Akira

Post Doctoral Associates

HASHIMOTO, Takashi

YOSHIDA, Toru

Dozono, Masanori (Oct. 2010 ~)

CHERUBINI, Silvio (June. 2010 ~)

TSUCHIMOTO, Yuji

MATSUBARA, Hideaki (Oct. 2010 ~)

Graduate Students

SASAMOTO, Yoshiko

ARAMAKI, Yoki

SANO, Satoshi

KAHL, David. M

MIYA, Hiroyuki

HORI, Yasuto

TSUJI, Tomoya

KAWASE, Shoichiro

KISAMORI, KeiIchi

NUKARIYA, Atsushi

LEUNG, Tang. T (Oct. 2010 ~)

YAMAGUCHI, Yorito

DAM, Nguyen Binh (~ Sept. 2010)

HAYAKAWA, Seiya

TAKAHARA, Akihisa

AKIMOTO, Ryoji

TOKIEDA, Hiroshi

GO,Shintaro

HAYASHI, ShinIchi

TAKAKI, Motonobu

KIKUCHI, Yosuke

Administration Staff

HIRANO, Midori

YAMAMOTO, Ikuko

ENDO, Takako

KISHI, Yukino

ITAGAKI, Toshiko

SOMA, Yuko

Committees

Steering Committee

YAMAGATA, Toshio
AIHARA, Hiroaki
HAYANO, Ryugo
OTSUKA, Takaharu
KUBONO, Shigeru
SHIMOURA, Susumu
GONOKAMI, Makoto
NAGAMIYA, Shoji
KOBAYASHI, Tomio
TAKAHASHI, Hiroyuki

Department of Earth and Planetary Science
Department of Physics, Graduate School of Science
Department of Physics, Graduate School of Science
Department of Physics, Graduate School of Science
Center for Nuclear Study, Graduate School of Science
Center for Nuclear Study, Graduate School of Science
Department of Physics, Graduate School of Science
J-PARC Project Office,
International Center for Elementary Particle Physics
Department of Nuclear Engineering and Management

